

(70)

# Multi-echo Methods for Fast MRI and MRS of <sup>31</sup>P Containing Compounds

By

Hui Chao

B. S., Electrical Engineering, Wuhan University (1987)  
M. S., Electrical Engineering, Wuhan University (1990)

MIT LIBRARIES

AUG 11 1997

SCHERING

SUBMITTED TO  
THE HARVARD-MASSACHUSETTS INSTITUTE OF TECHNOLOGY  
DIVISION OF HEALTH SCIENCE AND TECHNOLOGY  
IN PARTIAL FULFILLMENT OF THE REQUIREMENTS FOR THE DEGREE OF  
DOCTOR OF PHILOSOPHY IN MEDICAL ENGINEERING AND MEDICAL PHYSICS

at

Massachusetts Institute of Technology

February 1997

© Hui Chao, 1997

The author hereby grants to MIT permission to reproduce and to distribute  
copies of this thesis document in whole or in part.

Signature of Author.....

Department of Harvard-Massachusetts Institute of Technology  
Division of Health Science and Technology, Jan. 28, 1997

Certified by.....

Robert V. Mulkern  
Assistant Professor of Radiology, Harvard Medical School  
Thesis Supervisor

Accepted by .....

HARVARD MASSACHUSETTS INSTITUTE  
OF TECHNOLOGY

Martha L. Gray  
J.W. Kieckhefer Associate Professor of  
Electrical Engineering and Computer Science  
Co-Director, Health Science and Technology

FEB 26 1997

SCHERING-PLEURON

LIBRARIES

## Acknowledgments

I feel very grateful for having had the opportunity to pursue my doctoral degree at HST and for the support, the help and the encouragement from the people I met during my graduate studies.

I thank my advisor, Dr. Robert Mulkern, who educated me in many aspects of research. His willingness to spend time discussing problems, to help in preparation my manuscripts, thesis and presentations has been greatly appreciated. His honesty, kindness and sense of humor have made my Ph.D. work with him one of the most enjoyable and rewarding experiences of my life.

I thank Dr. John Bowers who taught me not only how to make NMR probes but more importantly taught me to believe in myself. His encouragement and confidence in me have helped me go through many frustrating times during my graduate studies.

I thank Dr. David Holtzman for providing the research opportunity for my Ph.D. project and for introducing me the physiological aspects involved in my research. His generous help in reading many drafts of abstracts, papers and this thesis are greatly appreciated.

I thank Dr. Gilberto Gonzalez for his willingness to be my committee member and for his support with this project. He has been very generous with helpful ideas and comments in reading my manuscripts and this thesis.

I thank Prof. David Cory for many helpful discussions about my research projects and NMR theories. I thank former HST Director Prof. Roger Mark for his guidance, support and help in my graduate studies. I thank people in HST office, Karen, Don, Chris and Keiko, for helps with administrative tasks. I thank all my friends, Peili, Yingchun, Chun, Osman, Tsumu, Changmei and Adirl, for talking with me and keeping me laughing.

I thank my parents, brother and sister-in-law for supporting me at every stage of my life and career. My bother, Wei, has always been my positive role model and he still will be. I wouldn't have been able to pursue career so far without him.

Finally, I thank my husband for his love and support. I have been very fortunate to meet him early in my graduate study and truly lucky to have him as my friend and companion for the rest of my life.

**Committee Members:**

Robert Mulkern, Ph.D.  
Assistant Professor of Radiology  
Children's Hospital  
Harvard Medical School

David Holtzman, MD., Ph.D.  
Associate Professor of Neurology  
Children's Hospital  
Harvard Medical School

Gilberto Gonzalez, MD., Ph.D.  
Associate Professor of Radiology  
Massachusetts General Hospital  
Harvard Medical School

David Cory, Ph.D.  
Associate Professor of Nuclear Engineering  
Massachusetts Institute of Technology

## Table of Contents

List of figures.....	2
List of table.....	3
Abstract.....	4
Part I Multi-echo <sup>31</sup> P spectroscopic imaging of ATP.....	5
Introduction.....	6
Chapter 1. Background.....	8
1.1 Chemical shift imaging.....	8
1.2 Multi-echo spectroscopic imaging.....	9
1.3 The application of NMR to ATP.....	9
1.4 Homonuclear spin coupled system.....	10
1.5 Density matrix analysis of coupled system.....	11
Chapter 2. Theory.....	13
2.1 Basic NMR principles.....	13
2.1.1 Magnetic moments and magnetization.....	13
2.1.2 Spin-Spin relaxation (T <sub>2</sub> ) phenomena.....	16
2.1.3 Chemical shift.....	17
2.2 Spectroscopic imaging.....	18
2.3 Multi-echo spectroscopic imaging.....	18
2.4 Density matrix analysis of spin coupled systems.....	20
Analytical derivation.....	21
Numerical analysis.....	24
Chapter 3. Experiment.....	27
3.1 Spectral experiment.....	27
3.2 Spectroscopic imaging (SI).....	27
3.2.1 Phantom.....	28
3.2.2 In vivo.....	28
3.2.3 Pulse sequence.....	28
Chapter 4. Results.....	32
4.1 Phantom experiment.....	32
4.2 In vivo experiment.....	43
Chapter 5. Discussion.....	51
Appendix.....	54
Appendix I: A numerical calculation of the AMX density operator formalism.....	54
Appendix II: Simulation of J-coupling effect on the spatial mapping in the case of TE=n/J.....	59
Part II Fast PCr imaging: feasibility of monitoring muscle metabolism.....	64
Introduction.....	65
Chapter 1. Background.....	67
1.1 Phosphocreatine (PCr) in biological systems.....	67
1.2 PCr level reflects the metabolic changes in patho-physiologic processes....	69

1.3 Previous PCr imaging.....	70
1.4 Shortening PCr imaging time.....	71
1.5 Summary.....	71
Chapter 2. NMR Theory.....	73
2.1 MRI Theory.....	73
2.2 Spin-echo and multi-echo technique.....	73
2.3 Spin-spin relaxation (T2) effect in RARE Image.....	75
2.4 Suppression of unwanted resonance.....	78
2.5 Determination of spectral width of the RF pulse.....	78
Chapter 3. Experimental material and method.....	81
3.1 Instrumentation.....	81
3.2 Pulse sequence.....	84
3.3 Phantom experiment for technique testing.....	87
3.4 Experimental setup and protocol for human forearm study.....	88
3.4.1 The spectra acquisition before and after exercise.....	88
3.4.2 CPMG acquisition.....	88
3.4.3 Regional PCr change during/after exercise and the comparison with T2 weighted proton image.....	89
3.4.4 PCr recovery rate after exercise.....	89
Chapter 4. Results.....	91
4.1 Phantom experiment.....	91
4.2 Human forearm muscle studies.....	91
4.2.1 Spectral acquired before and after exercise.....	95
4.2.2 CPMG acquisition.....	95
4.2.3 Regional PCr change during/after exercise and the comparison with T2 weighted proton images.....	99
4.2.4 PCr recovery rate after exercise.....	104
Chapter 5. Discussion.....	108
5.1 Pi suppression.....	108
5.2 CPMG mode determines the optimal number of echoes can be used in the RARE mode.....	109
5.3 Reduce the motion artifacts.....	110
5.4 Implementation on the clinical system.....	110
5.5 Instrumentation: Coil and active shielded gradients.....	110
5.6 PCr imaging and T2-weighted proton imaging.....	111
5.7 PCr recovery rate.....	111
References.....	114

List of Figure:

Part I:

Figure 2.1.....	14
Figure 3.1.....	29
Figure 3.2.....	30
Figure 4.1.....	34
Figure 4.2.....	35

Figure 4.3.....	36
Figure 4.4.....	37
Figure 4.5.....	39
Figure 4.6.....	41
Figure 4.7.....	42
Figure 4.8.....	44
Figure 4.9.....	47, 48, 49
Figure 4.10.....	50

Part II:

Figure 1.1.....	68
Figure 2.2.....	77
Figure 3.1.....	82
Figure 3.2.....	83
Figure 3.3.....	85
Figure 3.2.....	86
Figure 4.1.....	92
Figure 4.2.....	93
Figure 4.3.....	94
Figure 4.4.....	96
Figure 4.5.....	97
Figure 4.6.....	98
Figure 4.7.....	100, 101
Figure 4.8.....	102, 103
Figure 4.9.....	105, 106
Figure 4.10.....	107

Table 1.....	46
--------------	----

**Multi-echo Methods for Fast MRI and MRS of  $^{31}\text{P}$  Containing Compounds**  
by  
**Hui Chao**

Submitted to the Harvard-Massachusetts Institute of Technology Division of Health Sciences and Technology on Jan. 28, 1997 in partial fulfillment of the requirements for the Degree of Doctoral of Philosophy in Medical Engineering and Medical Physics

**Abstract**

Spectroscopic imaging of  $^{31}\text{P}$  metabolites and ATP in particular with multiple spin echoes is useful for reducing data acquisition times. The usual T2 decay processes which degrade multi-echo spectroscopic imaging methods, however, are further compounded by J-coupling modulations in the case of ATP. We determine how these modulations affect multi-echo spectroscopic imaging k-space data and produce systematic spatial misregistrations of the ATP resonances. The specific AMX J-coupling modulations of ATP are determined in order to identify echo spacing effects in multi-echo spectroscopic imaging of ATP and to determine appropriate post-processing correction schemes to address the spatial misregistration problem. An in vivo demonstration of the technique which offers a three-fold reduction in scan time compared to conventional SI methods is provided and compared with the conventional SI approach.

Phosphocreatine (PCr) plays an important role in energy metabolism. PCr level partially reflects the energy state of tissue. In the transition from rest to work ATP turnover rate in skeletal muscle may increase as much as several orders of magnitude. Muscle ATP concentrations do not change while PCr declines. When ATP concentration is closely regulated, the net effect of metabolism is the breaking down of PCr to Pi and Creatine(Cr). AT2 value of about 400 ms for PCr makes multi-echo imaging or Rapid Acquisition with Relaxation Enhancement (RARE) techniques useful in shortening PCr imaging time. We acquired PCr images by collecting thirty-two Carr-Purcell-Meiboom-Gill (CPMG) echoes following each excitation and selectively suppressing inorganic phosphate (Pi) signal. Each CPMG echo was recorded with a distinct phase encoding step. This technique was applied to monitor energy metabolism (i.e. PCr depletion after muscle contraction), and ATP resynthesis (i.e. PCr recovery during muscle recovery). Images were recorded with 2 cc spatial resolution and 5 min and 30 sec scan time.

In summary, in this study, we demonstrate, for the first time, the feasibility of multi-echo spectroscopic imaging(SI) of  $^{31}\text{P}$  metabolites especially ATP for in vivo studies, which reduces scan time by a factor of three compared to conventional technique, and multi-echo PCr imaging, which reduces scan time by a factor of thirty-two, providing a better spatial and temporal resolution for the study of energy metabolism.

**Thesis Advisor:**      **Robert V. Mulkern**  
Assistant Professor of Radiology  
Children's Hospital  
Harvard Medical School

## **Part I**

### **Multi-echo $^{31}\text{P}$ spectroscopic imaging of ATP: A Scan time reduction strategy**

The goal of this part of research is to shorten the spectroscopic imaging (SI) time of the  $^{31}\text{P}$  containing metabolite ATP, and to evaluate and demonstrate the feasibility of multi-echo spectroscopic imaging of  $^{31}\text{P}$  containing metabolites in vivo which offers a three-fold reduction in scan time compared to conventional SI methods.

## Introduction:

Adenosine triphosphate (ATP) plays a central role in the energy metabolism of living cells. Clinical applications of  $^{31}\text{P}$  Nuclear Magnetic Resonance (NMR) studies of ATP and other phosphorous containing metabolites, however, are hampered by low sensitivity. This makes acquisition times for spectroscopic imaging of  $^{31}\text{P}$  containing metabolites rather long and subsequently difficult to apply clinically.

Multi-echo spectroscopic imaging has previously been proposed and demonstrated as a means to reduce scan times for proton spectroscopic imaging (SI) studies (Mulkern et al, 1991, Oshio et al, 1992, Duyn et al, 1993, 1995). With this approach, several spin echoes are collected following each excitation and each echo is used for a distinct spatial phase encoding step, as in the Rapid Acquisition with Relaxation Enhancement (RARE) fast imaging technique (Hennig et al, 1986, mulkern et al, 1990, 1991). Given the same repetition time TR and number of phase encoding steps, scan time reductions over conventional spectroscopic imaging by factors equal to the number of echoes collected per excitation are attained with the multi-echo approach. Disadvantages include reduced spectral resolution due to short signal readouts and T2 related attenuation of k-space lines. The T2 attenuation of k-space lines leads to a general degradation of the spatial mapping along the dimension encoded with multiple echoes (Mulkern et al, 1990, 1991, Oshio et al 1992, Duyn et al, 1993, 1995, Hennig et al, 1986). Given these limitations, long T2 values and well-separated spectral components provide the best combination for application of multi-echo spectroscopic imaging methods.

Early reports suggested that in vivo T2 values for the  $^{31}\text{P}$  ATP resonances were in the 8 to 40 ms range (Turner et al 1984, Thomsen et al, 1989, Albrand et al,

1986, Merboldt et al, 1990). Such short T2 values would render multi-echo approaches to spectroscopic imaging of ATP impractical. There have been however, several more recent studies in which the critical importance of J-coupling among the ATP resonances to spin echo amplitudes has been carefully taken into account (Straubinger et al, 1994, Jung et al, 1992, 1993). These studies suggest that the actual T2 values of  $^{31}\text{P}$  ATP resonances in vivo are in the 60 to 100 ms range. Since at 4.7 T, the major spectral peaks of in vivo  $^{31}\text{P}$  spectra can be resolved using spectral readouts as short as 17 ms (vide infra), the longer T2 values recently reported suggest the feasibility of collecting several spectroscopic echoes within the 100 ms time frame provided by the T2 relaxation in order to reduce  $^{31}\text{P}$  spectroscopic imaging scan times.

Towards this end, a theoretical analysis of AMX spin echo modulations was performed and used in conjunction with 7 T spectroscopic results of ATP solutions to determine the echo time dependence of signal from each of the three ATP peaks. One-dimensional (1D) Carr-Purcell-Meiboom-Gill (CPMG) and RARE multi-echo spectroscopic imaging sequences were implemented at 4.7 T to test the feasibility of mapping ATP signals with multi-echo methods. Both the CPMG and RARE data sets of the ATP phantom were completely consistent with the 7 T spectroscopic results and the theoretical analyses. The J-coupling modulations of the different k-space lines in RARE mode acquisitions led to well-defined spatial misregistration of the distinct ATP peaks. The misregistration problem is shown to be amenable to correction with post-processing techniques based on an understanding of the J-coupling modulations among the ATP nuclei. Finally, a RARE mode acquisition in a live mouse was performed to demonstrate the feasibility of mapping ATP signals in vivo with a three-fold reduction in scan time compared to conventional SI methods. Spectral and spatial quality differences between the RARE mode acquisition and a conventional 1D  $^{31}\text{P}$  SI of the live mouse are discussed.

## **Chapter 1.**

### **Background**

In this chapter previous studies relative to multi-echo spectroscopic imaging of ATP are reviewed briefly .

One of the advantage of magnetic resonance imaging over other clinical imaging modalities is the potential to provide specific chemical information in vivo. Spectroscopic imaging which provides spectral resolution and some degree of spatial localization and spatial or anatomic resolution can enhance our understanding of the biological and patho-physiological function (Rosen et al, 1988, Bruhn et al, 1989, Frahm 1989).

#### **1.1 Chemical shift imaging**

Conventional spectroscopic imaging (described in detail in the next chapter) as presented by Brown et al. in 1982 involves exciting the spin system, phase encoding the resulting transverse magnetization with phase encoding gradients, and signal acquisition (readout) in the absence of applied field gradients. Phase encoding gradients encode the magnetizations according to their spatial position. Readouts are performed in the absent of field gradients so that Fourier Transform along this direction yields the spectral information.

Usually the low concentration of metabolite nuclei and low NMR sensitivity in the case of  $^{31}\text{P}$  reduce the overall sensitivity of conventional SI techniques ( Mora et al, 1991, Tsuji et al, 1996 ). Multiple averages are required to achieve a reasonable Signal to Noise Ratio (SNR), making high quality metabolite mapping a lengthy procedure, hampering clinical applications.

## 1.2 Multi-echo spectroscopic imaging

A multi-echo sequence was realized by Mulkern et al. in 1991 for reducing spectroscopic imaging times. In this approach several spin echoes with different phase encoding steps, representing different k space lines, were collected following each excitation. Given the same repetition time TR and number of phase encoding steps, scan time reductions over conventional spectroscopic imaging by factors equal to the number of echoes collected per excitation are attained with this approach (Mulkern et al, 1990, Oshio et al, 1992, Duyn et al, 1993, 1995). Here we refer to this approach as RARE mode due to its similarity to commonly known Rapid Acquisition with Relaxation Enhancement(RARE) fast imaging technique(Hennig et al, 1986, Mulkern et al, 1990, 1991, Melki et al, 1992). The shortening of scan time using RARE mode approaches depends on the T2 value of the components and the spectral resolution required to resolve different resonances or equivalently, the duration of the readout period.

## 1.3 The application of NMR to ATP

The  $^{31}\text{P}$  NMR in vivo contains unique information about the energy state of tissue(Bottomley et al., 1988, Buchli et al. 1994, Tsuji et al. 1996). Adenosine triphosphate (ATP) provides a fuel for the energy metabolism of living cell. Resonances from ATP, PCr and Pi all contribute to in vivo  $^{31}\text{P}$  spectra. Because of low NMR sensitivity to  $^{31}\text{P}$  compared to proton and low concentration of the metabolites, conventional SI methods applied in 1D spatial encoding formats often require long scan times (Tsuji et al, 1996) which limited the clinical applications of  $^{31}\text{P}$  nuclear NMR studies of ATP and other phosphorous containing metabolites.

Although Multi-echo spectroscopic imaging has previously been proposed and demonstrated as a means to reduce scan times for proton SI studies, the

application to  $^{31}\text{P}$  has been neglected and most spectroscopic imagings of  $^{31}\text{P}$  metabolites have been performed with conventional SI approaches (Nelson et al, 1991, Tsuji et al, 1996 ). The lack of attention paid to multi-echo methods for  $^{31}\text{P}$  SI to date may be due to a long-standing misconception that T2 values of ATP resonances are short, in the 8 to 40 ms range (Turner et al, 1984, Thomsen et al, 1989, Albrand et al., 1989, Merboldt et al, 1990). If this were the case, multi-echo SI methods would be of little value for mapping some of most informative  $^{31}\text{P}$  resonances, the three ATP resonances. Several recent reports provide more accurate assessments of in vivo ATP T2 values by properly taking into account J-coupling effects among the ATP nuclei (Straubinger et al, 1994, Jung et al, 1992, 1993). These reports find ATP T2 values in vivo in the 65 to 100 ms range. This important finding led us to consider multi-echo approaches for  $^{31}\text{P}$  studies, particularly at high field where short echo readouts suffice to resolve the individual peaks of in vivo  $^{31}\text{P}$ .

#### **1.4 Homonuclear spin coupled system**

ATP, which contains more than one phosphorus nucleus, is a homonuclear coupled spin system. Because at 4.7T the J-coupling constant, which is independent of field strength is much smaller than the chemical shift, the nuclear coupling is represented by a weakly coupled AMX system. Although the modulation of spin-echo signal due to the existence of homonuclear spin coupling is a well known phenomenon (Hahn et al, 1952) and its phase modulation of the Fourier transformed signals has been used to achieve selective editing of spin-coupling multiplets, consideration of artifacts induced by this modulation on the multi-echo spectroscopic image has not been fully explored.

In Duyn et al's RARE mode spectroscopic imaging of lactate, an AX3 spin coupling system, a simple approach was used to avoid the spin coupling

modulation of the echo, where echo time was chosen to be integer numbers of  $1/J$  to avoid the spin-coupling modulation (Duyn et al, 1993, 1995). Because lactate has relatively long T2 value, multiple echoes were able to be acquired following each excitation (Duyn et al., 1993, 1995)

Because three ATP resonances are spin-spin coupled with relatively short T2s, the application of multi-echo to these resonance more complicated. The usual T2 decay processes which degrade multi-echo spectroscopic imaging methods are further compounded by J-coupling modulations in the case of ATP.

### 1.5 Density matrix analysis of coupled system

In the NMR experiments, successive RF pulses applied prior to signal acquisition give rise to complex spectral modulations for a coupled spin systems. Interpulse timing delays, RF flip angles and phases all affect these modulations. Fully understanding these effects is important for optimizing a specific study. Density matrix theory is a powerful, elegant and relatively simple formalism for describing in detail the time evolution of spin system (Farr 1990, Mulkern 1994). Starting from the Hamiltonian of a coupled system, the density matrix is calculated and magnetizations from a bulk of spins which have experienced successive RF pulses can be derived.

This study was designed to study the feasibility of multi-echo approaches for shortening the spectroscopic imaging of  $^{31}\text{P}$  containing metabolites, and to understand the J-coupling modulation effects multi-echo spectroscopic images. An analytical analysis of J-coupling modulation is conducted for AMX coupled spin systems and generalized numerical calculations are presented for any type of coupled systems. J-coupling effects on multi-echo spectroscopic imaging of ATP were fully explored with phantom studies as well as with computer simulations.

An in vivo demonstration of the multi-echo approach for  $^{31}\text{P}$  spectroscopic imaging is provided to show the feasibility of this technique.

## Chapter 2

### Theory

This chapter reviews the basic principles of NMR theory, NMR spectroscopic imaging, multi-echo spectroscopic imaging given by Slichter (1989), Abragam (1981) and Becker (1980) with emphasis on aspects more relevant to my research. Density matrix theory using numerical and analytical methods to study spin coupled systems relevant to our study are discussed.

#### 2.1 Basic NMR principles

In magnetic resonance we observe a signal produced by the magnetic moments of the nuclei. This signal is an electric current induced in a receiver coil by precessing magnetic moments (Figure 2.1).

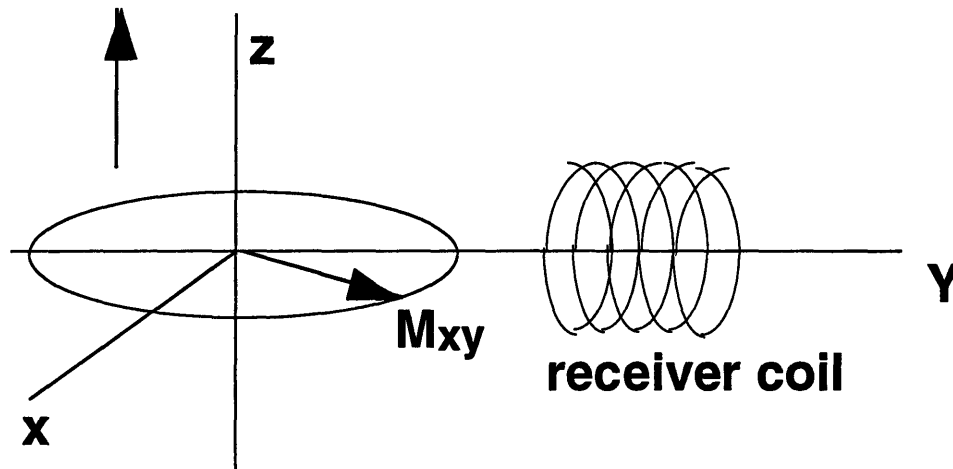
##### 2.1.1 Magnetic moments and magnetization

Many atomic nuclei in their ground state have a non-zero spin angular momentum  $I\hbar$  (integer or half integer of Plank's constant) and associated dipolar magnetic moment as:

$$\mu = \gamma I\hbar. \quad (2.1)$$

Where  $\gamma$  is the gyromagnetic ratio of the nuclei, which is measured in units of  $radians \cdot sec^{-1} \cdot gauss$  . The collective macroscopic magnetic moments are denoted as magnetization  $M$ .

$$B_z = B_0 + \vec{G}(t) \cdot \vec{r}$$



$$\omega(t) = \gamma B_z = \gamma B_0 + \gamma \vec{G}(t) \cdot \vec{r}$$

Figure 2.1 In NMR an electric signal is induced in a receiver coil by the magnetization. This magnetization is flipped by a  $90^\circ$  pulse to the transverse or xy plane. The magnetization will precess in that plane with a frequency proportional to the local magnetic field strength.

Consider an isolated spin system: the application of a magnetic field to the nucleus will produce an interaction energy between nucleus and field and can be described by the Hamiltonian operator  $\mathcal{H}$  :

$$\mathcal{H} = -\vec{\mu} \cdot \vec{B}_0 \quad (2.2)$$

It can be shown that the solution of this Hamiltonian gives energy level in which

$$E_m = -\gamma\hbar m B_0 \quad (2.3)$$

The quantum number  $m$  may assume the values

$$-I, -I+1, \dots, I-1, I.$$

For spin of  $I=1/2$ , there are two energy levels. The energy separation between the states is linearly dependent on the magnetic field. In the presence of an applied external electromagnetic radio-frequency field  $B_1$ , the interaction between the spin system and applied radio-frequency field can be expressed as:

$$\mathcal{H}' = 2\mu_x H_1 \cos \omega t \quad (2.4)$$

Where  $\omega = \gamma B_0$ , is called the Larmor frequency. Nuclear Magnetic Resonance arises when the RF field is applied at the Larmor frequency and causes the transition of magnetic moments between energy levels from their lower to higher energy state . Transitions are induced by the absorption of energy from the applied electromagnetic field. The signals we observed are radiations of energy when the nuclei return to the original lower energy state or thermal equilibrium state.

In practice, the magnetic moment from a single nucleus is far too small to induce detectable current in a coil; signals are actually from an ensemble of identical nuclei. The macroscopic magnetization  $M$  is the vector sum of the individual magnetic moments which are oriented along the main magnetic field  $B_0$  direction or longitudinal direction ( $z$  direction) in the presence of magnetic field  $B_0$  and has a value  $M_0$ . The imposed RF field  $B_1$  at the Larmor frequency can be treated as acting on  $M$ , rather than on single magnetic moment. The RF field flips  $M_0$  away from the  $z$  axis into transverse or  $xy$  plane.  $M_{xy}$  is generated and precesses in the plane perpendicular to the main magnetic field. An electrical signal is then generated by  $M_{xy}$  with intensity proportional to the magnitude of  $M_{xy}$ .

Our studies are based on the detection of  $^{31}\text{P}$  nuclear signals in biological systems.

### **2.1.2 Spin-Spin relaxation ( $T_2$ ) phenomena**

Imposing a  $90^\circ$  RF  $B_1$  field at the Larmor frequency results in the flip of  $M$  into transverse direction as  $M_{xy}$ . The existence of  $M_{xy}$  component implies some phase coherence in the  $xy$  plane. As nuclei exchange energy with each other, they gradually dephase and lose their phase coherence, and decay back to their equilibrium value of zero (spin-spin relaxation). At the same time the nuclei lose energy to their surroundings (spin-lattice relaxation), and  $M_z$  relaxes back to its original value of  $M_0$ .

Spin-spin relaxation, also called transverse relaxation, is a process in which the magnetization in the transverse or  $xy$  plane decays with characteristic relaxation time  $T_2$ .  $T_2$  is the time constant for the decay of the precessing  $xy$  component of magnetization following a disturbance such as an application of RF pulse. The magnetization can be described as:

$$M_{xy}(t) = M_{xy}(0)e^{-\frac{t}{T_2}} \quad (2.8)$$

Therefore, given an echo time TE, the electrical signal detected is not only proportional to the spin density or nuclear density but also weighted by the exponential function described in Eq. 2.8 as the T2 relaxation effect.

### 2.1.3 Chemical shift

When a nucleus is placed in magnetic field  $B_0$ , the actual magnetic field a nucleus experiences is not equal to the applied field  $B_0$ , but a field which is altered by the screening or shielding of the electrons surrounding the nucleus. Since electrons are magnetic particles also, their motion is influenced by the imposition of the applied magnetic field. The motion induced by the applied field is in the opposite direction to the applied field (Lenz's law). The actual magnetic field a nucleus experiences is :

$$\begin{aligned} B_{eff}(nucleus) &= B_0 - B_{shielding} \\ &= B_0 - \sigma B_0 = B_0(1 - \sigma) \end{aligned} \quad (2.6)$$

The screen factor, or shielding factor,  $\sigma$  is around  $10^{-6}$ . The chemical shift difference in frequency can be calculated as:

$$\Delta f = \Delta\sigma\gamma B_0 \quad (2.7)$$

Therefore, though in  $^{31}\text{P}$  NMR we observe phosphorous nuclei, because of surrounding electron clouds, the actual resonant frequencies are different from molecule to molecule. Phosphorous nuclei in ATP, PCr and Pi each has a unique

resonance frequency, which allows us to differentiate signals generated by different molecules.

## 2.2 Spectroscopic imaging

In a conventional spectroscopic imaging sequence, phase encoding gradients are applied for spatial modulation and readout is performed in the absence of gradients so that the echoes are modulated by phase encoding gradient as well as the chemical shift resonant frequency. In the case of 1-D spectroscopic imaging, the signal we detect is:

$$S \propto \int \rho(y, \omega_\alpha) \exp\{i\gamma \int_t (yG_y t' + \omega_\alpha t') dt'\} dy d\omega_\alpha \quad (2.1)$$

where  $y$  is the phase encoding direction, and  $\omega_\alpha$  is the chemical shift frequency. This equation can be further simplified as:

$$\begin{aligned} S(k_y, t) &\propto \int \rho(y, \omega_\alpha) \exp\{i\gamma \int_t \overbrace{G_y t'}^{k_y} dt'\} + i\omega_\alpha t\} dy d\omega_\alpha \\ &\propto \int \rho(y, \omega_\alpha) \exp\{iky_y + i\omega_\alpha t\} dy d\omega_\alpha \end{aligned} \quad (2.2)$$

The Fourier Transform of the 2-D data  $S$  with two variables:  $k_y$  and  $t$ , yields the spectroscopic or chemical shift imaging  $\rho(y, \omega_\alpha)$  which provides spectral resolution and spatial localization or anatomic resolution.

## 2.3 Multi-echo Spectroscopic Imaging

Similar to the RARE imaging technique, in multi-echo spectroscopic imaging, several spin echoes are acquired following each excitation and each echo is used for a distinct phase encoding gradient step for spatial encoding. Each echo is recorded

in the absence of gradient (Figure 3.1). However, the shortening of imaging time has more limitations in SI than regular anatomic imaging: the number of echoes recorded depends not only upon the T2 decay time but also on how long a time period is used for acquiring each individual echo. Furthermore, in case of multiple spin systems, J-coupling modulations should be determined precisely to optimize the timing of the pulse sequence.

In spectroscopic imaging, spectral resolution is inversely proportional to the readout duration, the longer the readout, the higher the spectral resolution. The essential problem therefore is the minimum spectral resolution required for a given SI application.

At  $TE = T2$ , the signal intensity, which is  $S = S_0 \exp(-TE/T2)$ , will drop to 36.7% of the maximum. Using T2 as the time envelope, the number of echoes which can be collected following excitation, which is also the scan time reduction factor should be less than  $T2/\text{readout-duration}$ .

The CPMG mode multi-echo approach (Figure 3.1), which requires the same scan time as conventional SI, is best suited for studying the fundamental tradeoffs between T2 decay, spectral resolution and the total number of usable echoes for a given task. In CPMG mode, multiple spectra are acquired with different echo times (TE). For example, it has been found from CPMG SI studies of vertebral bone marrow that a 32 ms echo readout is sufficient for spectral quantitation of fat and water at 1.5 T. In addition, spectral T2 values of approximately 80 and 120 ms were measured from the CPMG data sets for the water and fat marrow resonances, respectively. Thus, three to six usable echoes can be acquired for RARE mode SI studies of vertebral marrow in order to provide sufficient information of relative fat/water concentrations in minimal scan times.

In the case of a spin-coupled systems, the number of usable echoes which can be recorded becomes more complicated. Prior knowledge about the J-modulation is

necessary in order to properly choose echo time and to achieve maximal SNR within limited time periods. CPMG mode acquisitions are useful for testing the theoretical derivation of J-coupling modulation.

## 2.4 Density Matrix Analysis of Spin Coupled system

In our study, the density Matrix Formalism (Abragam, 1978, Farr 1990, Mulkern 1994) was used to derive an expression for the transverse magnetization at the center of each CPMG echo for the general case of a weakly-coupled AMX spin system. Starting with the general concept of density matrix analysis, using AMX spin system as an example, both numerical calculation and analytic derivations will be discussed.

The signal detected is produced by the sum of magnetic moments, in the transverse plane

$$\begin{aligned} S &\propto \langle \mu_x + i\mu_y \rangle \\ &\propto \langle I_x + iI_y \rangle = \text{Tr}[\hat{\sigma}(I_x + iI_y)] \end{aligned}$$

Where  $\hat{\sigma}$  is the density operator which represents the time evolution of coupled spin following successive application of RF pulses. The trace(Tr) of the density operator acting on the appropriate spin operator gives the expectation value.

From the Hamiltonian, the density matrix operator can be derived. The Hamiltonian of the AMX system is

$$H_{AMX} = \omega_\alpha I_{\alpha z} + \omega_\beta I_{\beta z} + \omega_\gamma I_{\gamma z} + J_{\alpha\beta} I_{\alpha z} I_{\beta z} + J_{\beta\gamma} I_{\beta z} I_{\gamma z} + J_{\alpha\gamma} I_{\alpha z} I_{\gamma z} \quad (2.3)$$

where  $\omega_\alpha$ ,  $\omega_\beta$  and  $\omega_\gamma$  are chemical shifts for the three resonances,  $J_{\alpha\beta}$ ,  $J_{\beta\gamma}$  and  $J_{\alpha\gamma}$  are the coupling constants and  $I_{\alpha z}$ ,  $I_{\beta z}$  and  $I_{\gamma z}$  are the longitudinal magnetic

moment components of the three resonances. The density matrix operator for the center of the nth CPMG echo reads:

$$\sigma = \left[ e^{-iH_{AMX}T/2} e^{-i\pi F_y} e^{-iH_{AMX}T/2} \right]^n e^{-i\frac{\pi}{2}F_x} I_z e^{i\frac{\pi}{2}F_x} \left[ e^{iH_{AMX}T/2} e^{i\pi F_y} e^{iH_{AMX}T/2} \right]^n \quad (2.4)$$

Where

$$\begin{aligned} F_x &= I_{\alpha x} + I_{\beta x} + I_{\gamma x}; \\ F_y &= I_{\alpha y} + I_{\beta y} + I_{\gamma y}; \end{aligned} \quad (2.5)$$

the operation of  $e^{-i\frac{\pi}{2}F_x}$  and  $e^{i\frac{\pi}{2}F_x}$  represent the application of  $90^\circ$  excitation pulse,  $e^{-iH_{AMX}T/2}$  and  $e^{iH_{AMX}T/2}$  represent the time interval between the RF pulses, and  $e^{-i\pi F_y}$  and  $e^{i\pi F_y}$  represent the application of  $180^\circ$  refocusing pulses.

The J-coupling modulation of transverse magnetization as a function of time can be derived by the calculation of the expectation value of magnetic moments in the transverse plane, which is the trace of the density operator acting on the transverse magnetic moments.

*Analytical derivation:* assuming perfect  $90^\circ$  excitation pulse and  $180^\circ$  refocusing pulses, an expression can be derived for the expectation value of magnetic moments.

The eigenfunction of the Hamiltonian is derived based on eight basic product states of three spins system which are  $|+++ \rangle$ ,  $| - + + \rangle$ ,  $| + - + \rangle$ , ...,  $| - - - \rangle$ . It can be demonstrated that those are actually the eigenstates of the weakly coupled AMX system. The eight eigenstates and the corresponding eigenvalues are as follows:

Define	$\begin{aligned}  +++ \rangle &=  a\rangle \\  -++ \rangle &=  b\rangle \\  +-+ \rangle &=  c\rangle \\  ++- \rangle &=  d\rangle \\  --+ \rangle &=  e\rangle \\  +- - \rangle &=  f\rangle \\  -- - \rangle &=  g\rangle \\  --- \rangle &=  h\rangle \end{aligned};$	there is	$\begin{aligned} H_{AMX} a\rangle &= a a\rangle \\ H_{AMX} b\rangle &= b b\rangle \\ H_{AMX} c\rangle &= c c\rangle \\ H_{AMX} d\rangle &= d d\rangle \\ H_{AMX} e\rangle &= e e\rangle \\ H_{AMX} f\rangle &= f f\rangle \\ H_{AMX} g\rangle &= g g\rangle \\ H_{AMX} h\rangle &= h h\rangle \end{aligned};$
--------	---	----------	---

where	$\begin{aligned} a &= \frac{\omega_\alpha}{2} + \frac{\omega_\beta}{2} + \frac{\omega_\gamma}{2} + \frac{J_{\alpha\beta}}{4} + \frac{J_{\beta\gamma}}{4} + \frac{J_{\gamma\alpha}}{4}; \\ b &= -\frac{\omega_\alpha}{2} + \frac{\omega_\beta}{2} + \frac{\omega_\gamma}{2} - \frac{J_{\alpha\beta}}{4} + \frac{J_{\beta\gamma}}{4} - \frac{J_{\gamma\alpha}}{4}; \\ c &= \frac{\omega_\alpha}{2} - \frac{\omega_\beta}{2} + \frac{\omega_\gamma}{2} - \frac{J_{\alpha\beta}}{4} - \frac{J_{\beta\gamma}}{4} + \frac{J_{\gamma\alpha}}{4}; \\ d &= \frac{\omega_\alpha}{2} + \frac{\omega_\beta}{2} - \frac{\omega_\gamma}{2} + \frac{J_{\alpha\beta}}{4} - \frac{J_{\beta\gamma}}{4} - \frac{J_{\gamma\alpha}}{4}; \\ e &= -\frac{\omega_\alpha}{2} - \frac{\omega_\beta}{2} + \frac{\omega_\gamma}{2} + \frac{J_{\alpha\beta}}{4} - \frac{J_{\beta\gamma}}{4} - \frac{J_{\gamma\alpha}}{4}; \\ f &= -\frac{\omega_\alpha}{2} + \frac{\omega_\beta}{2} - \frac{\omega_\gamma}{2} - \frac{J_{\alpha\beta}}{4} - \frac{J_{\beta\gamma}}{4} + \frac{J_{\gamma\alpha}}{4}; \\ g &= \frac{\omega_\alpha}{2} - \frac{\omega_\beta}{2} - \frac{\omega_\gamma}{2} - \frac{J_{\alpha\beta}}{4} + \frac{J_{\beta\gamma}}{4} - \frac{J_{\gamma\alpha}}{4}; \\ h &= -\frac{\omega_\alpha}{2} - \frac{\omega_\beta}{2} - \frac{\omega_\gamma}{2} + \frac{J_{\alpha\beta}}{4} + \frac{J_{\beta\gamma}}{4} + \frac{J_{\gamma\alpha}}{4}; \end{aligned}$
-------	--

Given a density matrix operator  $\sigma$ , for any sequence,  $\langle I_{\alpha+} \rangle$  will be calculated from the trace of the 8 X 8 matrix:

$$\begin{bmatrix} \langle a|\sigma I_{\alpha+}|a\rangle & \langle a|\sigma I_{\alpha+}|b\rangle & \langle a|\sigma I_{\alpha+}|c\rangle & \langle a|\sigma I_{\alpha+}|d\rangle & \langle a|\sigma I_{\alpha+}|e\rangle & \langle a|\sigma I_{\alpha+}|f\rangle & \langle a|\sigma I_{\alpha+}|g\rangle & \langle a|\sigma I_{\alpha+}|h\rangle \\ \langle b|\sigma I_{\alpha+}|a\rangle & \langle b|\sigma I_{\alpha+}|b\rangle & \langle b|\sigma I_{\alpha+}|c\rangle & \langle b|\sigma I_{\alpha+}|d\rangle & \langle b|\sigma I_{\alpha+}|e\rangle & \langle b|\sigma I_{\alpha+}|f\rangle & \langle b|\sigma I_{\alpha+}|g\rangle & \langle b|\sigma I_{\alpha+}|h\rangle \\ \langle c|\sigma I_{\alpha+}|a\rangle & \langle c|\sigma I_{\alpha+}|b\rangle & \langle c|\sigma I_{\alpha+}|c\rangle & \langle c|\sigma I_{\alpha+}|d\rangle & \langle c|\sigma I_{\alpha+}|e\rangle & \langle c|\sigma I_{\alpha+}|f\rangle & \langle c|\sigma I_{\alpha+}|g\rangle & \langle c|\sigma I_{\alpha+}|h\rangle \\ \langle d|\sigma I_{\alpha+}|a\rangle & \langle d|\sigma I_{\alpha+}|b\rangle & \langle d|\sigma I_{\alpha+}|c\rangle & \langle d|\sigma I_{\alpha+}|d\rangle & \langle d|\sigma I_{\alpha+}|e\rangle & \langle d|\sigma I_{\alpha+}|f\rangle & \langle d|\sigma I_{\alpha+}|g\rangle & \langle d|\sigma I_{\alpha+}|h\rangle \\ \langle e|\sigma I_{\alpha+}|a\rangle & \langle e|\sigma I_{\alpha+}|b\rangle & \langle e|\sigma I_{\alpha+}|c\rangle & \langle e|\sigma I_{\alpha+}|d\rangle & \langle e|\sigma I_{\alpha+}|e\rangle & \langle e|\sigma I_{\alpha+}|f\rangle & \langle e|\sigma I_{\alpha+}|g\rangle & \langle e|\sigma I_{\alpha+}|h\rangle \\ \langle f|\sigma I_{\alpha+}|a\rangle & \langle f|\sigma I_{\alpha+}|b\rangle & \langle f|\sigma I_{\alpha+}|c\rangle & \langle f|\sigma I_{\alpha+}|d\rangle & \langle f|\sigma I_{\alpha+}|e\rangle & \langle f|\sigma I_{\alpha+}|f\rangle & \langle f|\sigma I_{\alpha+}|g\rangle & \langle f|\sigma I_{\alpha+}|h\rangle \\ \langle g|\sigma I_{\alpha+}|a\rangle & \langle g|\sigma I_{\alpha+}|b\rangle & \langle g|\sigma I_{\alpha+}|c\rangle & \langle g|\sigma I_{\alpha+}|d\rangle & \langle g|\sigma I_{\alpha+}|e\rangle & \langle g|\sigma I_{\alpha+}|f\rangle & \langle g|\sigma I_{\alpha+}|g\rangle & \langle g|\sigma I_{\alpha+}|h\rangle \\ \langle h|\sigma I_{\alpha+}|a\rangle & \langle h|\sigma I_{\alpha+}|b\rangle & \langle h|\sigma I_{\alpha+}|c\rangle & \langle h|\sigma I_{\alpha+}|d\rangle & \langle h|\sigma I_{\alpha+}|e\rangle & \langle h|\sigma I_{\alpha+}|f\rangle & \langle h|\sigma I_{\alpha+}|g\rangle & \langle h|\sigma I_{\alpha+}|h\rangle \end{bmatrix}$$

The trace of the matrix is the sum of its diagonal elements. Calculation of these diagonal matrix elements provides the means to yield the transverse magnetization during readout for any specified sequence:

$$\langle I_{\alpha+} \rangle = \langle a|\sigma I_{\alpha+}|a\rangle + \langle b|\sigma I_{\alpha+}|b\rangle + \langle c|\sigma I_{\alpha+}|c\rangle + \dots + \langle h|\sigma I_{\alpha+}|h\rangle;$$

After further derivation, the non-zero terms left are:

$$\langle I_{\alpha+} \rangle = \langle b|\sigma|a \rangle + \langle e|\sigma|c \rangle + \langle f|\sigma|d \rangle + \langle h|\sigma|g \rangle;$$

For given pulse sequence and Hamiltonian, each term can be calculated.

As the  $\pi/2$  pulse along x axis flips the spin into y axis, and  $\pi$  pulse along y axis changes the sign of both  $F_x$  and  $F_z$ , density matrix can be simplified as follows:

$$\begin{aligned} \sigma &= \left[ e^{-iH_{AMX}T/2} \underbrace{e^{-i\pi F_y} e^{-iH_{AMX}T/2}}_{e^{-iH'_{AMX}T/2}} \right]^n \underbrace{e^{-i\frac{\pi}{2}F_x} I_{\alpha} e^{i\frac{\pi}{2}F_x}}_{I_{\alpha y}} \left[ e^{iH_{AMX}T/2} \underbrace{e^{i\pi F_y} e^{iH_{AMX}T/2}}_{e^{iH'_{AMX}T/2}} \right]^n \\ &= [e^{-iH_{AMX}T/2} e^{-iH'_{AMX}T/2}]^n I_{\alpha y} [e^{iH_{AMX}T/2} e^{iH'_{AMX}T/2}]^n \end{aligned}$$

where 
$$H'_{AMX} = -\omega_{\alpha}I_{\alpha z} - \omega_{\beta}I_{\beta z} - \omega_{\gamma}I_{\gamma z} + J_{\alpha\beta}I_{\alpha z}I_{\beta z} + J_{\beta\gamma}I_{\beta z}I_{\gamma z} + J_{\alpha\gamma}I_{\alpha z}I_{\gamma z}$$

with eigen values of

$$\begin{aligned} a' &= -\frac{\omega_{\alpha}}{2} - \frac{\omega_{\beta}}{2} - \frac{\omega_{\gamma}}{2} + \frac{J_{\alpha\beta}}{4} + \frac{J_{\beta\gamma}}{4} + \frac{J_{\gamma\alpha}}{4}; & e' &= \frac{\omega_{\alpha}}{2} + \frac{\omega_{\beta}}{2} - \frac{\omega_{\gamma}}{2} + \frac{J_{\alpha\beta}}{4} - \frac{J_{\beta\gamma}}{4} - \frac{J_{\gamma\alpha}}{4}; \\ b' &= \frac{\omega_{\alpha}}{2} - \frac{\omega_{\beta}}{2} - \frac{\omega_{\gamma}}{2} - \frac{J_{\alpha\beta}}{4} + \frac{J_{\beta\gamma}}{4} - \frac{J_{\gamma\alpha}}{4}; & f' &= \frac{\omega_{\alpha}}{2} - \frac{\omega_{\beta}}{2} + \frac{\omega_{\gamma}}{2} - \frac{J_{\alpha\beta}}{4} - \frac{J_{\beta\gamma}}{4} + \frac{J_{\gamma\alpha}}{4}; \\ c' &= -\frac{\omega_{\alpha}}{2} + \frac{\omega_{\beta}}{2} - \frac{\omega_{\gamma}}{2} - \frac{J_{\alpha\beta}}{4} - \frac{J_{\beta\gamma}}{4} + \frac{J_{\gamma\alpha}}{4}; & g' &= -\frac{\omega_{\alpha}}{2} + \frac{\omega_{\beta}}{2} + \frac{\omega_{\gamma}}{2} - \frac{J_{\alpha\beta}}{4} + \frac{J_{\beta\gamma}}{4} - \frac{J_{\gamma\alpha}}{4}; \\ d' &= -\frac{\omega_{\alpha}}{2} - \frac{\omega_{\beta}}{2} + \frac{\omega_{\gamma}}{2} + \frac{J_{\alpha\beta}}{4} - \frac{J_{\beta\gamma}}{4} - \frac{J_{\gamma\alpha}}{4}; & h' &= \frac{\omega_{\alpha}}{2} + \frac{\omega_{\beta}}{2} + \frac{\omega_{\gamma}}{2} + \frac{J_{\alpha\beta}}{4} + \frac{J_{\beta\gamma}}{4} + \frac{J_{\gamma\alpha}}{4} \end{aligned}$$

Since  $H_{AMX}$  and  $H'_{AMX}$  commute ( $[H_{AMX}, H'_{AMX}] = 0$ ),  $\sigma$  density operator can be further simplified as:

$$\sigma = [e^{-i(H_{AMX} + H'_{AMX})nT/2}] I_{\alpha y} [e^{i(H_{AMX} + H'_{AMX})nT/2}]$$

$\langle I_{\alpha+} \rangle$  can be derived stepwise as:

$$\begin{aligned}
\langle b|\sigma|a\rangle &= e^{-i(b+b')nT/2+i(a+a')nT/2}\langle b|I_{\alpha y}|a\rangle = -\frac{i}{2}\exp[(J_{\alpha\beta} + J_{\gamma\alpha})nT]; \\
\langle e|\sigma|c\rangle &= e^{-i(e+e')nT/2+i(c+c')nT/2}\langle e|I_{\alpha y}|c\rangle = -\frac{i}{2}\exp[(J_{\alpha\beta} - J_{\gamma\alpha})nT]; \\
\langle f|\sigma|d\rangle &= e^{-i(f+f')nT/2+i(d+d')nT/2}\langle f|I_{\alpha y}|d\rangle = -\frac{i}{2}\exp[-(J_{\alpha\beta} - J_{\gamma\alpha})nT]; \\
\langle h|\sigma|g\rangle &= e^{-i(h+h')nT/2+i(g+g')nT/2}\langle h|I_{\alpha y}|g\rangle = -\frac{i}{2}\exp[-(J_{\alpha\beta} + J_{\gamma\alpha})nT];
\end{aligned} \tag{2.6}$$

thus

$$\langle I_{\alpha+} \rangle \propto \{\cos[(J_{\alpha\beta} + J_{\gamma\alpha})nT] + \cos[(J_{\alpha\beta} - J_{\gamma\alpha})nT]\};$$

similarly, there are

$$\begin{aligned}
\langle I_{\beta+} \rangle &\propto \{\cos[(J_{\alpha\beta} + J_{\beta\gamma})nT] + \cos[(J_{\alpha\beta} - J_{\beta\gamma})nT]\}; \\
\langle I_{\gamma+} \rangle &\propto \{\cos[(J_{\gamma\alpha} + J_{\beta\gamma})nT] + \cos[(J_{\gamma\alpha} - J_{\beta\gamma})nT]\};
\end{aligned} \tag{2.7}$$

thus, J coupling modulation of the magnetizations of three ATP resonances at the center of the nth echo ( $TE=nT$ ) can be simply expressed as two cosine functions in the case of having perfect  $90^\circ$  and  $180^\circ$  RF pulse. In many cases, derivation of an analytic expression can be extremely complicated (for example, when the flip angles for RF pulse are not exactly  $90^\circ$  and  $180^\circ$ ), J modulation can be found with numerical calculation.

*Numerical analysis:* All possible configurations of a given spin can be expressed as a linear combination of  $2^N$  basis matrices which correspond to the  $2^N$  eigenstates in the above analytic analysis, where N is the number of spin -1/2 nuclei

in the system. A single spin system, magnetic moment can be expressed as three Pauli matrices  $\tilde{\delta}_x$ ,  $\tilde{\delta}_y$ ,  $\tilde{\delta}_z$  and the unit matrix  $\tilde{\delta}_0$ :

$$\tilde{\delta}_x = \begin{bmatrix} 0 & 1 \\ 1 & 0 \end{bmatrix}; \quad \tilde{\delta}_y = \begin{bmatrix} 0 & -i \\ i & 0 \end{bmatrix}; \quad \tilde{\delta}_z = \begin{bmatrix} 1 & 0 \\ 0 & -1 \end{bmatrix}; \quad \tilde{\delta}_0 = \begin{bmatrix} 1 & 0 \\ 0 & 1 \end{bmatrix};$$

Define direct produce operation as:

$$\begin{aligned} \tilde{C} &= \tilde{A} \otimes \tilde{B} \\ &= \begin{bmatrix} A_{11}\tilde{B} & A_{12}\tilde{B} & \dots & A_{1n}\tilde{B} \\ A_{21}\tilde{B} & A_{22}\tilde{B} & \dots & A_{2n}\tilde{B} \\ \dots & \dots & \dots & \dots \\ A_{n1}\tilde{B} & A_{n2}\tilde{B} & \dots & A_{nn}\tilde{B} \end{bmatrix}; \end{aligned}$$

The components of magnetic moment in a three spin system (e.g. AMX) system can be expressed in matrix format. For example, in an AMX system, assuming A, M and X represent the magnetic moment of each spin, then there are:

$$\begin{aligned} \tilde{A}_x &= \tilde{\sigma}_x \otimes \tilde{\sigma}_0 \otimes \tilde{\sigma}_0; & \tilde{A}_y &= \tilde{\sigma}_y \otimes \tilde{\sigma}_0 \otimes \tilde{\sigma}_0; & \tilde{A}_z &= \tilde{\sigma}_z \otimes \tilde{\sigma}_0 \otimes \tilde{\sigma}_0; \\ \tilde{M}_x &= \tilde{\sigma}_0 \otimes \tilde{\sigma}_x \otimes \tilde{\sigma}_0; & \tilde{M}_y &= \tilde{\sigma}_0 \otimes \tilde{\sigma}_y \otimes \tilde{\sigma}_0; & \text{and} & \tilde{M}_z = \tilde{\sigma}_0 \otimes \tilde{\sigma}_z \otimes \tilde{\sigma}_0; \\ \tilde{X}_x &= \tilde{\sigma}_0 \otimes \tilde{\sigma}_0 \otimes \tilde{\sigma}_x; & \tilde{X}_y &= \tilde{\sigma}_0 \otimes \tilde{\sigma}_0 \otimes \tilde{\sigma}_y; & \tilde{X}_z &= \tilde{\sigma}_0 \otimes \tilde{\sigma}_0 \otimes \tilde{\sigma}_z; \end{aligned}$$

For any spin coupled system, the Hamiltonian matrix can be calculated using the above matrices. The Hamiltonian for the AMX coupled system,

$$H_{AMX} = \omega_\alpha \tilde{A}_z + \omega_\beta \tilde{M}_z + \omega_\gamma \tilde{X}_z + J_{\alpha\beta} \tilde{A}_z \tilde{M}_z + J_{\beta\gamma} \tilde{M}_z \tilde{X}_z + J_{\alpha\gamma} \tilde{X}_z \tilde{A}_z;$$

Given the Harmiltonian, each element in the density operator can be calculated with MATLAB. For the time evolution function with matrix in

exponential function, standard "*exp1* or *exp3*" can be used for the approximation. Thus, for each resonance the expectation value of the transverse magnetization, which are modulated by J coupling, can be calculated as the trace of density operator acting on the transverse magnetic moment. The MATLAB file for AMX system calculation can be found in the Appendix.

The advantages of numerical analyses are straightforward and not limited by the format of applied pulse sequences and flip angle of RF pulses in the sequences. The disadvantage is that matrix calculations especially with matrix in the exponential function could be time consuming.

## Chapter 3

### Experiment

Phantom experiments were performed to verify the theory and to evaluate the feasibility of the pulse sequence and the postprocessing techniques in correcting artifacts induced by the spin coupling effect. An in vivo experiment was performed to demonstrate the potential application of this approach in study biological systems.

#### 3.1 Spectroscopic experiment

Experiments were performed on a phosphorous metabolite solution containing 50 mM ATP and 50 mM inorganic phosphate in distilled water, pH=7.4. Approximately 1 ml of the solution was transferred to a 5 mm NMR tube for high resolution spectroscopic studies. Approximately 30 ml was transferred to a 25 mm diameter (OD), 50 mm high plastic vial for use as a phantom in the spectroscopic imaging studies.

High resolution phosphorus spin echo spectra were recorded using a 7.0 T GN-300WB spectrometer and a 10 mm multinuclear probe (General Electric, Fremont CA). Flip angles were calibrated with single pulse experiments and the 90° hard pulses were found to be 26 μs. Free precession spectra were acquired using 32 signal averages, a 10 s TR, 5 kHz bandwidth, 2 Watts of WALTZ-16 proton decoupling and processed with 1 Hz Lorentzian apodization. A series of Hahn spin echo spectra (90<sub>x</sub> - T/2 - 180<sub>y</sub> - T/2 - acquire) were acquired using 32 signal averages, a 10 kHz bandwidth, and a 10 s TR for each T/2 value ranging from 10 to 300 ms.

#### 3.2 Spectroscopic imaging (SI) experiment

Spectroscopic imaging experiments were performed with a 4.7 T Biospec (Bruker Instruments, Billerica, MA) with a 30 cm horizontal bore.

### **3.2.1 Phantom**

For the phantom experiments, a 10 cm long, 7 cm wide (diameter) loopgap RF coil was employed. A chamber containing 50ml, 100 mM ATP and Pi was used.

### **3.2.2 In vivo**

For the in vivo study of the anesthetized mouse, an 8 cm long, 3 cm wide (diameter) loopgap coil was employed to improve the volume filling factor.

### **3.2.3 Pulse sequence**

The two 1D multi-echo spectroscopic imaging sequences shown in Figure 3.1 were implemented on the Biospec. The amplitudes of the 100  $\mu$ s  $90^\circ$  and  $180^\circ$  hard pulses were calibrated by minimizing FID components and maximizing echo signals during a CPMG echo train applied in the absence of gradients. In both sequences, 0.5 ms phase encoding gradient lobes were applied prior to spectroscopic echo readouts and "unwound" following each readout. In the first sequence of Figure 3.1 (CPMG mode), the phase encode wind and rewind lobes were incremented from excitation-to-excitation to generate spectroscopic images at each echo time. In the second sequence of Figure 3.1 (RARE mode), the phase encode gradient amplitudes were incremented from echo-to-echo to rapidly fill a single k-space matrix. In RARE mode, scan times are shortened compared to CPMG mode by a factor equal to the number of echoes per echo train, given identical TR values and number of phase encode steps. A minimum of two signal averages were used in each experiment to allow for two-step phase cycling of the excitation pulse and receiver.

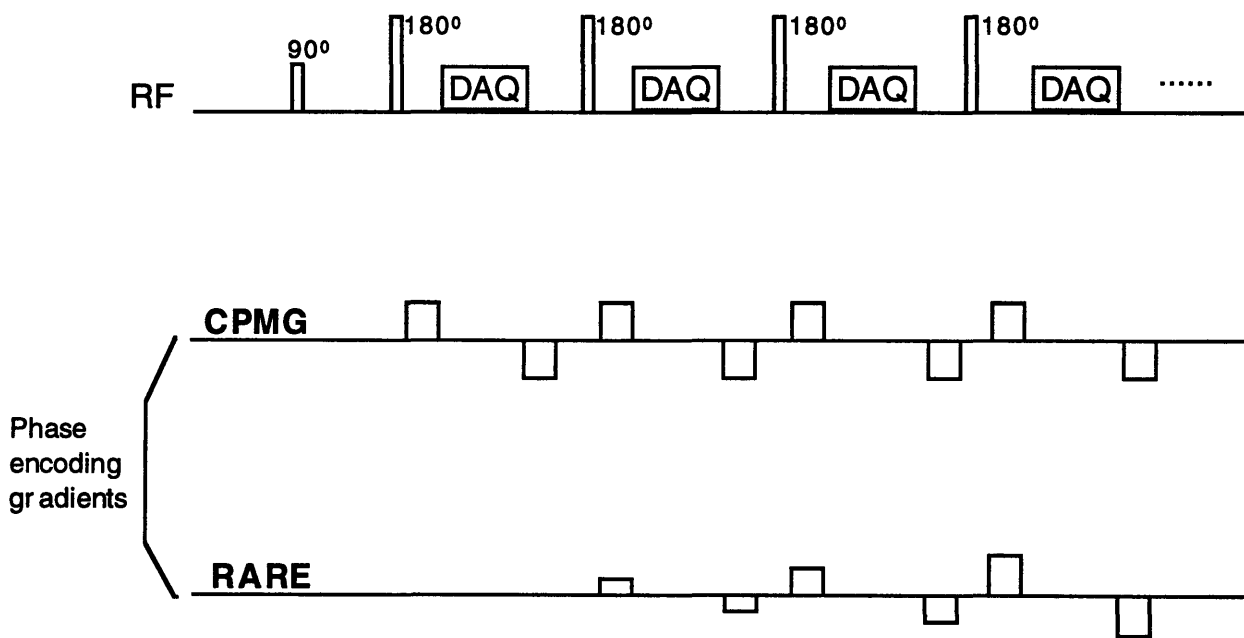


Figure 3.1 The pulse sequences for multi-echo 1-D spectroscopic imaging implemented at 4.7 T. The RF pulse train consists of a classic CPMG echo train. Each phase encode is applied prior to spectroscopic echo readout and is "unwound" after readout. In CPMG mode, the phase encode gradients are incremented from excitation-to-excitation while in RARE mode they are incremented from echo-to-echo reducing scan times by a factor equal to the number of echoes collected per excitation.

We tested echo train lengths from 3 to 16 and echo spacings from 17 to 52 ms. Echo readout durations were maximized for each echo spacing within the constraints of the RF pulse spacing and accommodation of the phase encode lobes. The centric phase encode reordering scheme (Mulkern et al, 1990, 1991) was employed for RARE mode acquisitions in which the lower phase encode gradients were applied to early echoes and the larger phase encode gradients to later echoes, as shown in Figure 3.2 a, b.

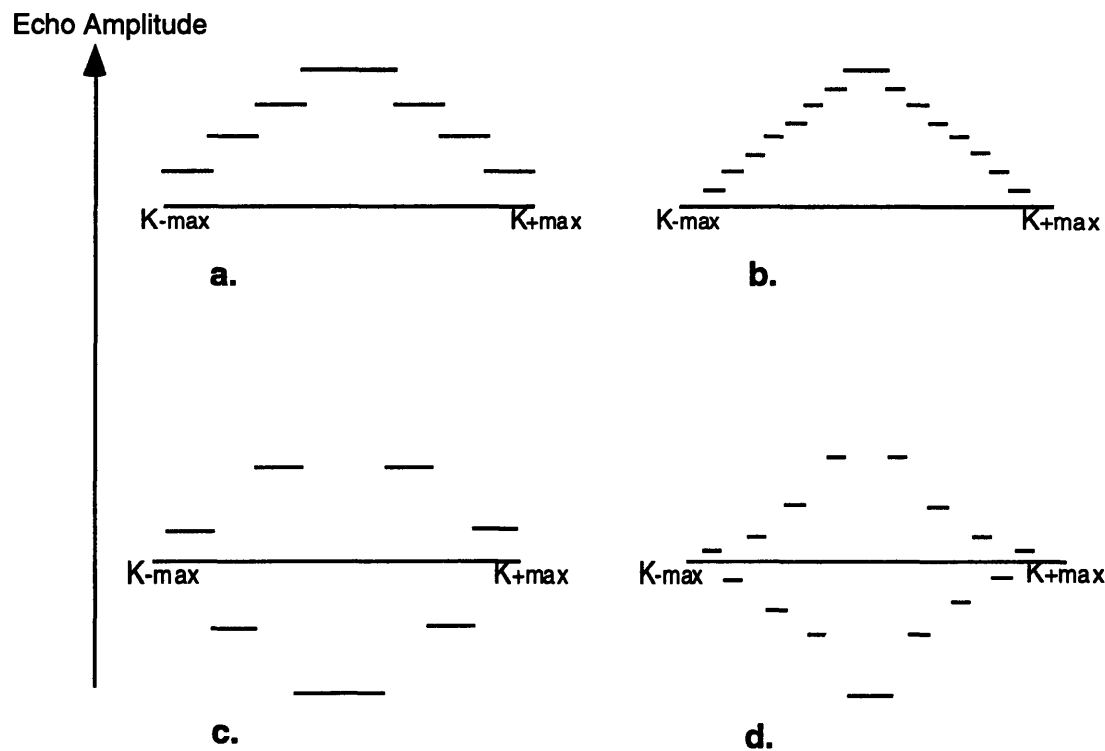


Figure 3.2. Diagrams depicting the relation between phase encode step (x-axes) and echo amplitudes (y-axes) for RARE mode acquisitions using 32 phase encodes and either 4 (a, c) or 8 (b, d) echoes. In this implementation, the lowest phase encode gradients are collected using the earliest echoes with larger phase encode gradients collected with later echoes using the so-called "centric" phase encode ordering

scheme. The upper two diagrams illustrate standard T<sub>2</sub>-decay effects on echo amplitudes while the lower two diagrams illustrate how J-coupling will affect the echo amplitudes in addition to T<sub>2</sub>-decay for  $\alpha$  and  $\gamma$  ATP resonances when a 52 ms echo spacing is employed.

## Chapter 4

### Results

Results combining theory and the phantom experiment are presented as high resolution spectra, the RARE SI, postprocessed image, and computer simulation. Results from in vivo experiments are presented as the RARE SI and postprocessed SI in comparison with the conventional spectroscopic imaging.

#### 4.1 Phantom experiment

*High resolution spectrum for coupling constant J measurement:* The proton decoupled 7 T  $^{31}\text{P}$  free precession spectra of the ATP resonances contained doublets for the  $\alpha$  and  $\gamma$  peaks and a triplet for the  $\beta$  peak. The coupling constants measured from the doublet separations of the  $\alpha$  and  $\gamma$  peaks were identical within experimental error and we find that  $J_{\alpha\beta} = J_{\gamma\beta} = J = 19.3 \pm 0.3$  Hz. The long range  $J_{\alpha\gamma}$  coupling was estimated to be less than 1 Hz, the approximate linewidth of the individual multiplets of our spectra. With no measurable difference between  $J_{\alpha\beta}$  and  $J_{\gamma\beta}$  and negligible long range coupling between  $\alpha$  and  $\gamma$ , Eq. 2.6 and Eq. 2.7 reduces to the form:

$$S \propto \{2\text{Cos}[J\pi TE]\}_{\alpha} + \{1 + \text{Cos}[J2\pi TE]\}_{\beta} + \{2\text{Cos}[J\pi TE]\}_{\gamma} \quad (3.1)$$

where the subscripts refer to the signal intensities of the individual ATP peaks. This equation predicts that for TE's chosen to be multiples of  $1/J = 52$  ms, the  $\beta$  peak will be consistently maximized at each echo time while the  $\alpha$  and  $\gamma$  peaks will oscillate

from maximal negative to maximal positive values for odd and even echoes, respectively.

*J* coupling modulation of the signal intensity on the SE spectra and the CPMG mode SI images. These predictions were confirmed by the 7.0 T Hahn spin echo spectra and by the CPMG mode spectroscopic images acquired at 4.7 T. Figure 4.1 shows 7 T Hahn spin echo absorption mode spectra at echo times of  $n/J$  for  $n = 1-4$  in which the  $\alpha$  and  $\gamma$  peaks oscillate from negative to positive in-phase doublets while the  $\beta$  peak remains a purely positive in-phase triplet. The CPMG mode 1D spectroscopic images of the phantom are shown in Figure 4.2. The top row shows spectroscopic images at the first four echo times from a 26 ms echo spacing, 16 echo data set. The lower row shows spectroscopic images at the first four echo times from a 52 ms echo spacing, 8 echo data set. Note the increased spectral peak separation (vertical axis) in the latter set of images due to the longer echo readouts. Both data sets were acquired in 2 minutes and 20 seconds using a 2.2 s TR, 32 phase encodes, a 10 cm FOV, and 2 signal averages per phase encode. Spectra extracted from the central locations in each of the images of Figure 4.2 are provided in Figure 4.3. Note the resolution of all three ATP peaks from each other and from Pi even with the relatively short 24 ms echo readouts. Spectra from the odd echoes of the 26 ms echo spacing data set have minimal ATP signals due to the J-coupling modulations. These signals return to full strength in the even echoes, apart from T2 decay. Spectra from the 52 ms echo spacing data set show full strength ATP signal apart from T2-decay at all echo times. The negative oscillations predicted for the  $\alpha$  and  $\gamma$  peaks are not observed because of the magnitude mode display.

Figure 4.4 plots signal intensity vs. echo time for all three ATP peaks as extracted from the complete set of images acquired with the 8 and 16 echo CPMG mode sequence. The intensities obey the predictions of equation 4 with regards to J-

coupling. Monoexponential T2 estimates made from the 52 ms echo spacing data, which effectively removed ATP J-coupling modulations for the magnitude data, yielded T2 values of 98 ms, 134 ms, and 180 ms for the  $\gamma$ ,  $\alpha$ , and  $\beta$  peaks, respectively.

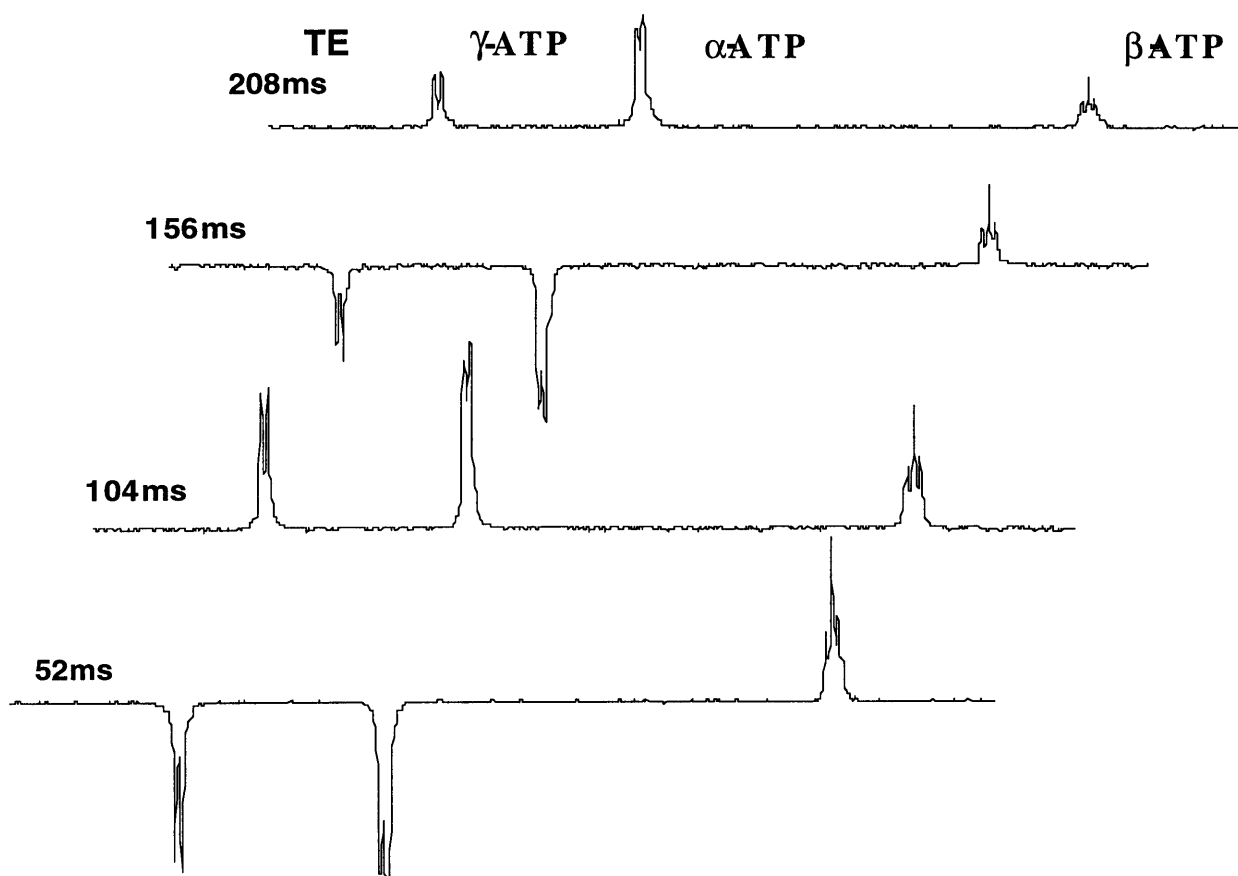


Figure 4.1. Proton decoupled,  $^{31}\text{P}$  spectra of ATP spectra acquired at 7 Tesla using a Hahn spin-echo sequence with TE set to multiples of  $1/J$ . TE value of 52, 104, 156 and 208 ms are shown. Note the negative to positive oscillations of the  $\alpha$  and  $\gamma$  resonances as predicted theoretically by Equation 3.1.

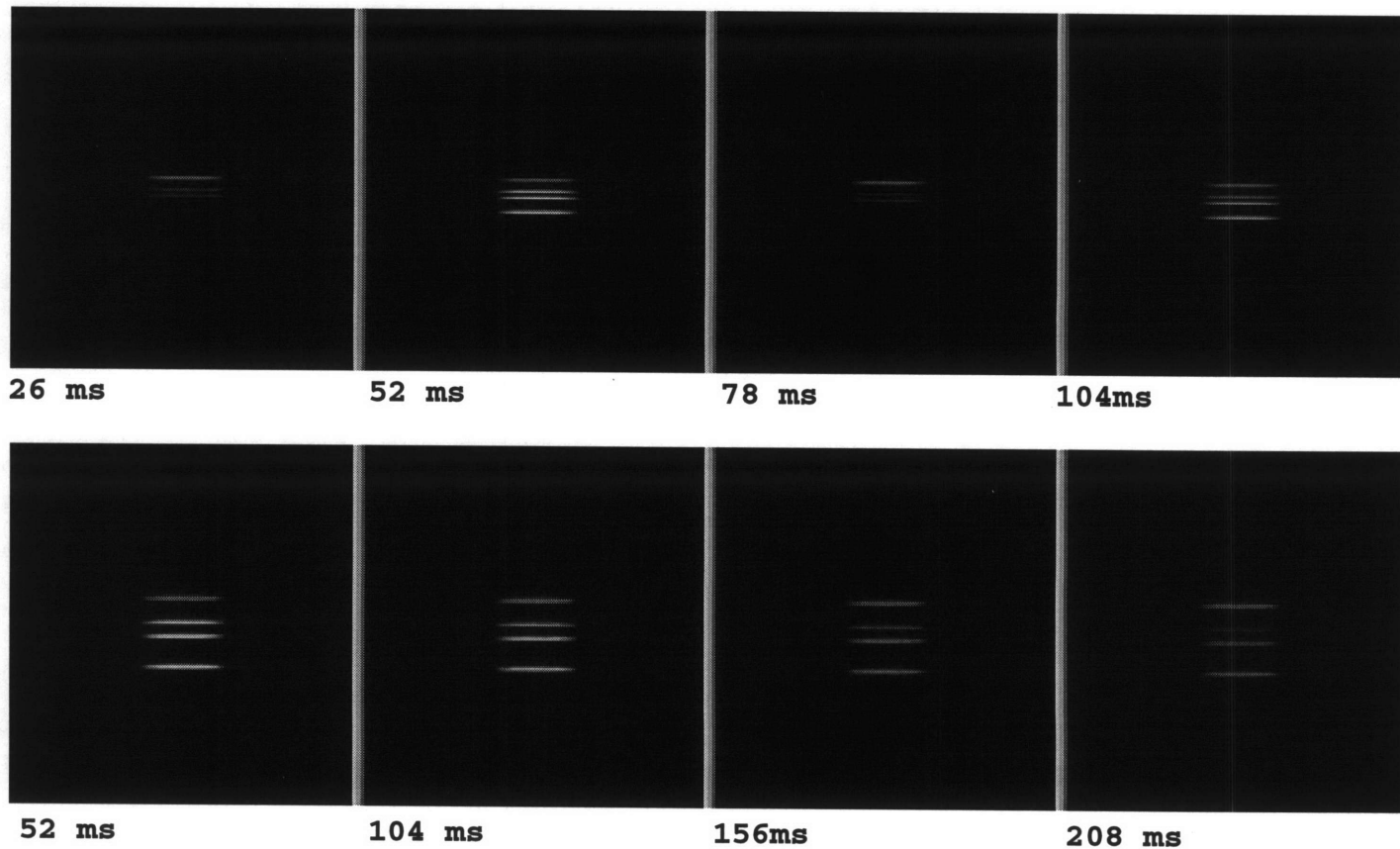


Figure 4.2 Top Row: Images at the first 4 echo times of a 16 echo CPMG mode acquisition of the phantom at 4.7 T using an echo spacing of 26 msec. Bottom Row: Images at the first 4 echo times of an 8 echo CPMG mode acquisition using the 52 ms echo spacing. The spectral peaks are well-resolved along the spectral axis (vertical) even in the short echo readout data sets and are, from top to bottom, Pi,  $\gamma$ ,  $\alpha$  and  $\beta$  ATP resonances. Scan time for each acquisition was 140 s.

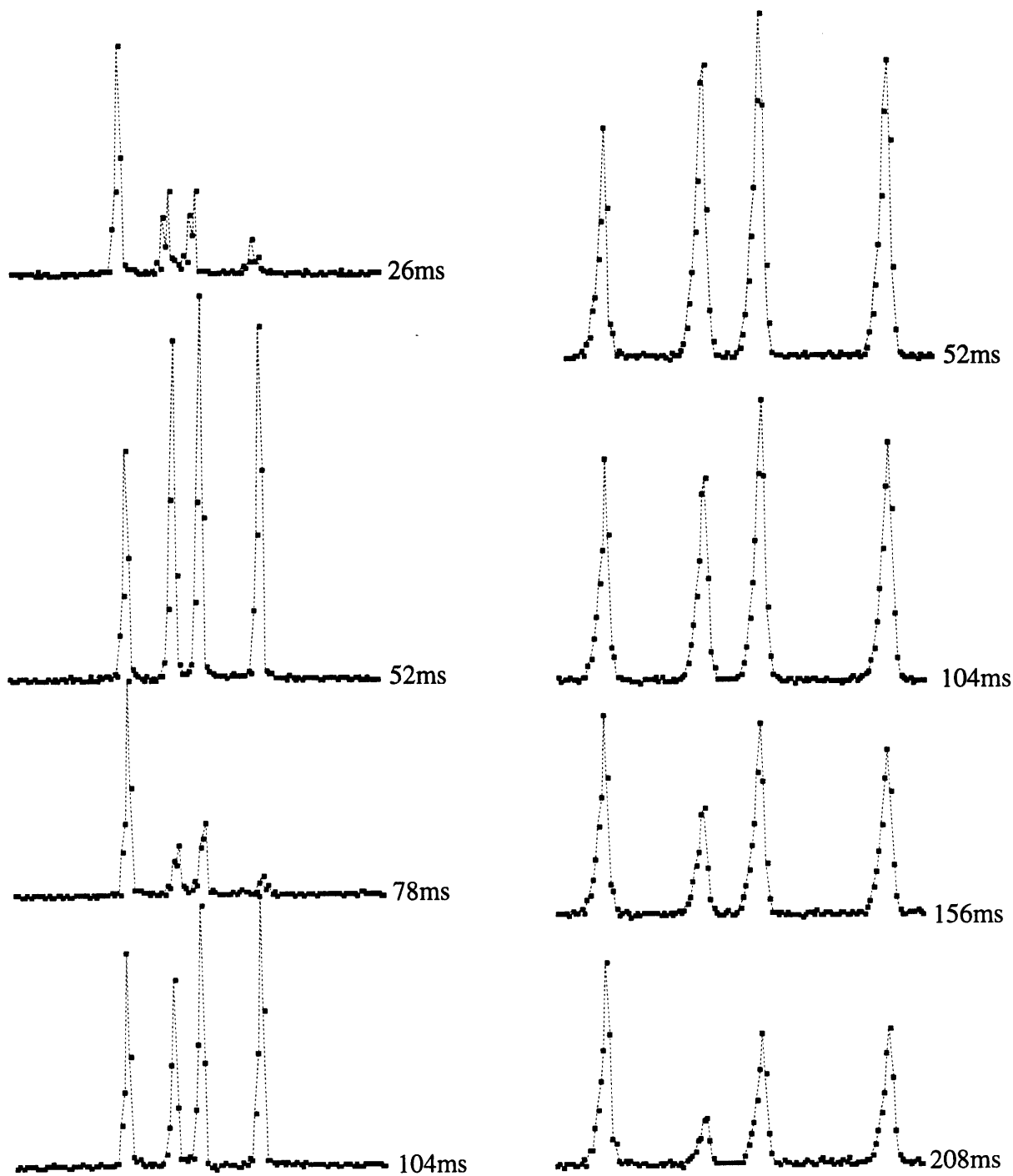
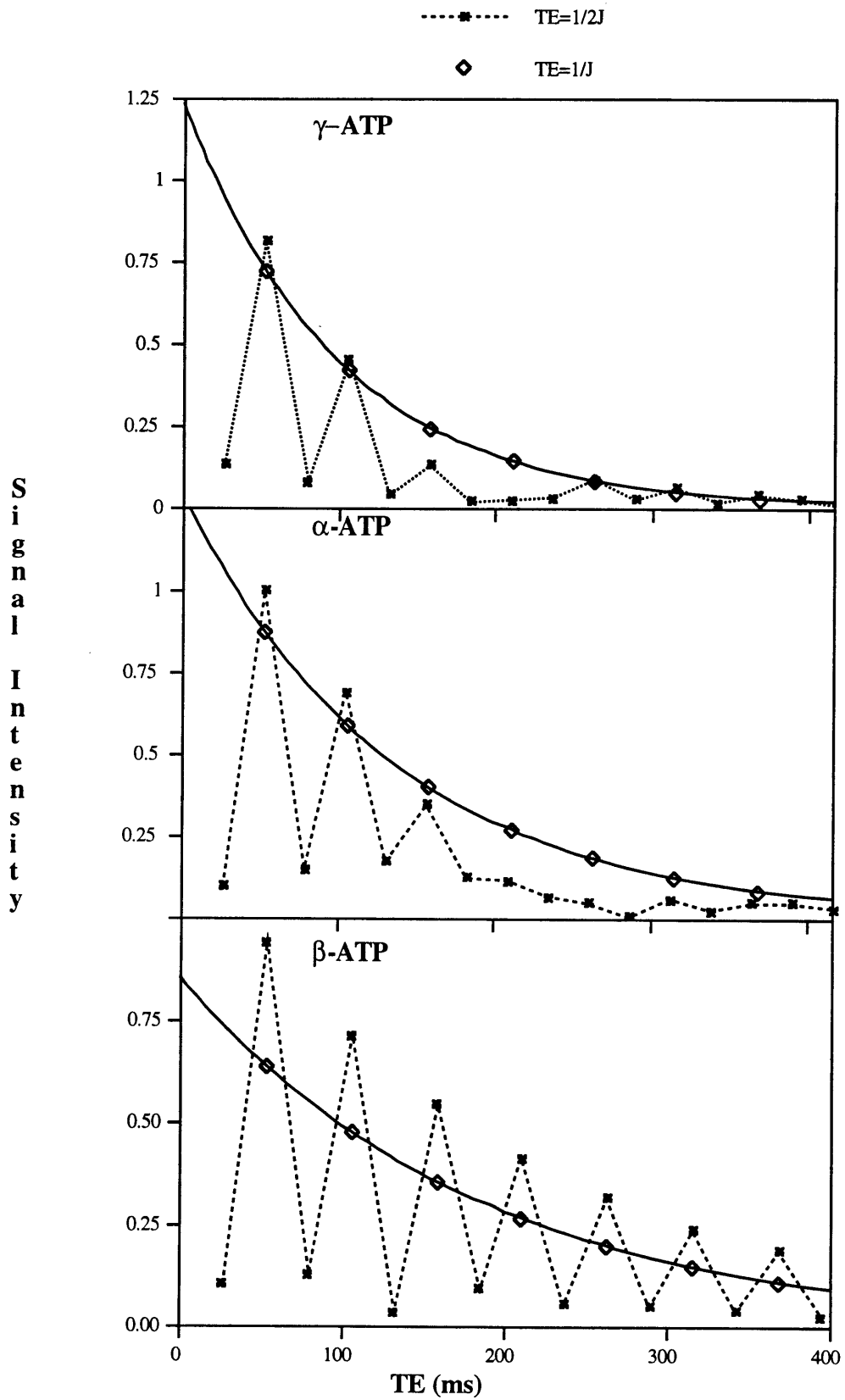


Figure 4.3. Spectra extracted from the central locations of the images in Figure 4. The spectral peaks are well-resolved and the J-coupling modulations predicted are observed. The use of magnitude calculation for data display precludes seeing the negative to positive oscillations of the  $\alpha$  and  $\gamma$  peaks in the 52 ms echo spacing data sets.



-----  
Figure 4.4 (Previous page) ATP signal intensities as a function of echo time as extracted from the full set of 16 and 8 echo CPMG images (Figure 4). Note how the 52 ms echo spacing data set allows for an estimation of T2 for all three peaks.  
-----

*Comparison of computer simulation and experimental results of the J coupling induced spatial misregistrations in the RARE SI and the correction of the misregistration:* From equation 3.1 and its confirmed behavior, one can readily infer how the k-space data lines of RARE mode acquisitions of ATP resonances will be affected by the spin echo modulations. For instance, when a 52 ms echo spacing is employed, the usual T2 weighting of echo amplitudes with respect to phase encode order, as illustrated in Figure 3.2 a,b apply to the  $\beta$  resonance for the particular 4 and 8 echo RARE acquisitions considered. For the  $\alpha$  and  $\gamma$  resonances, however, the diagrams of Figure 3.2 c,d now apply in which odd echoes have negative amplitudes in addition to the T2-weighting factor. With the centric phase encode ordering employed, adjacent blocks of k-space lines take on opposite signs for the  $\alpha$  and  $\gamma$  resonances. This results in a perfectly predictable effect on the spatial registration of these resonances upon Fourier transformation. Figure 4.5 a and b present 4 and 8 echo RARE mode spectroscopic images of the ATP phantom acquired with 52 ms echo spacings which demonstrate precisely the phenomenon discussed. These images, acquired using the same TR and number of phase encodes as the CPMG images, were generated in only 18 s (8 echo RARE) and 36 s (4 echo RARE) as compared to the 140 s required for the CPMG images. The  $\alpha$  and  $\gamma$  resonances show definitive ghosting patterns due to the negative/positive oscillations between odd and even echoes as translated into the k-space data. The uncoupled resonance from Pi is mapped with no ghosting along the phase encode dimension since it

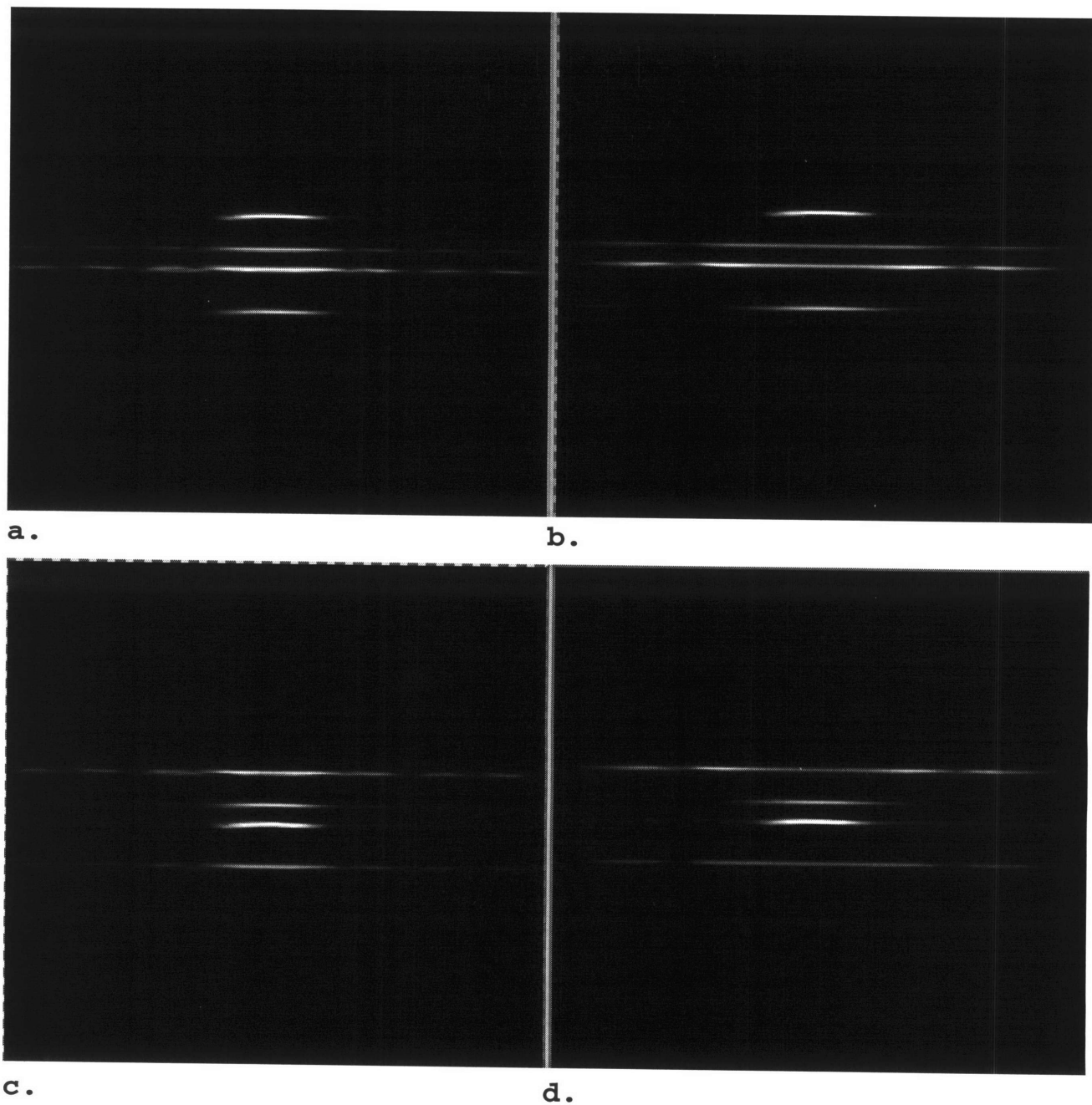


Figure 4.5. RARE mode spectroscopic images of the ATP phantom acquired at 4.7 T with a 4-echo, 8-shot sequence (a) and an 8-echo, 4-shot sequence requiring 36 and 18 s scan times, respectively. Echo spacing employed was 52 ms, leading to substantial ghosting of the  $\alpha$  and  $\gamma$  resonances along the spatially phase encoded dimension (horizontal). The ghosting is removed for these two resonances by proper k-space processing prior to Fourier transformation (c,d). The ghosting then occurs for the uncoupled Pi peak and the effectively uncoupled  $\beta$  ATP resonance.

experiences no J-coupling modulations. Similarly, with the echo spacing of  $1/J$ , the  $\beta$  resonance is maximally positive at all echo times and so is also mapped without any noticeable ghosting. Figures 4.5 c and d show the 4 and 8 echo RARE mode spectroscopic images in which the k-space data has been corrected to account for the  $\alpha$  and  $\gamma$  peak oscillations by multiplying k-space lines acquired from odd echoes by -1. The  $\alpha$  and  $\gamma$  resonances now reconstruct without ghosts along the phase encode dimension while the  $P_i$  resonance and the  $\beta$  ATP resonance now appear with substantial ghost artifact due to the additional k-space processing for these effectively "uncoupled" resonances.

Figure 4.6 demonstrates how well the phase encode spatial misregistration can be predicted with a thorough knowledge of the AMX coupling pattern for ATP and spectral T2 values. Shown in the figure are the experimental spatial profiles obtained from the spectroscopic images of Figure 4.5 a and b along with simulated spatial profiles. The latter were generated using equations previously developed to study T2-decay effects in RARE images for square phantom profiles (Mulkern et al., 1991 ) modified to include the J-coupling modulations of the  $\alpha$  and  $\gamma$  resonances in the 52 ms echo spacing RARE data sets. As seen, there is excellent agreement between the experimentally and theoretically determined spatial profiles.

*Using  $1/3J$  echo spacing:* The echo spacing of  $1/J$  simplifies echo modulations of the ATP signals but is, at 52 ms, too long for in vivo use where T2 values are reportedly in the 60 to 100 ms range (Straubinger et al., 1994, Jung et al, 1992, 1993). Furthermore, in vivo ATP J values have recently been reported to be on the order of 16 Hz ( Jung et al, 1996) rather than the 19 Hz observed in simple solutions. This would further lengthen the optimal  $1/J$  echo spacing and incur even greater T2-decay loss in vivo. We therefore examined an alternative echo space sampling approach as shown in Figure 4.7. Specifically this scheme utilizes the reduced echo

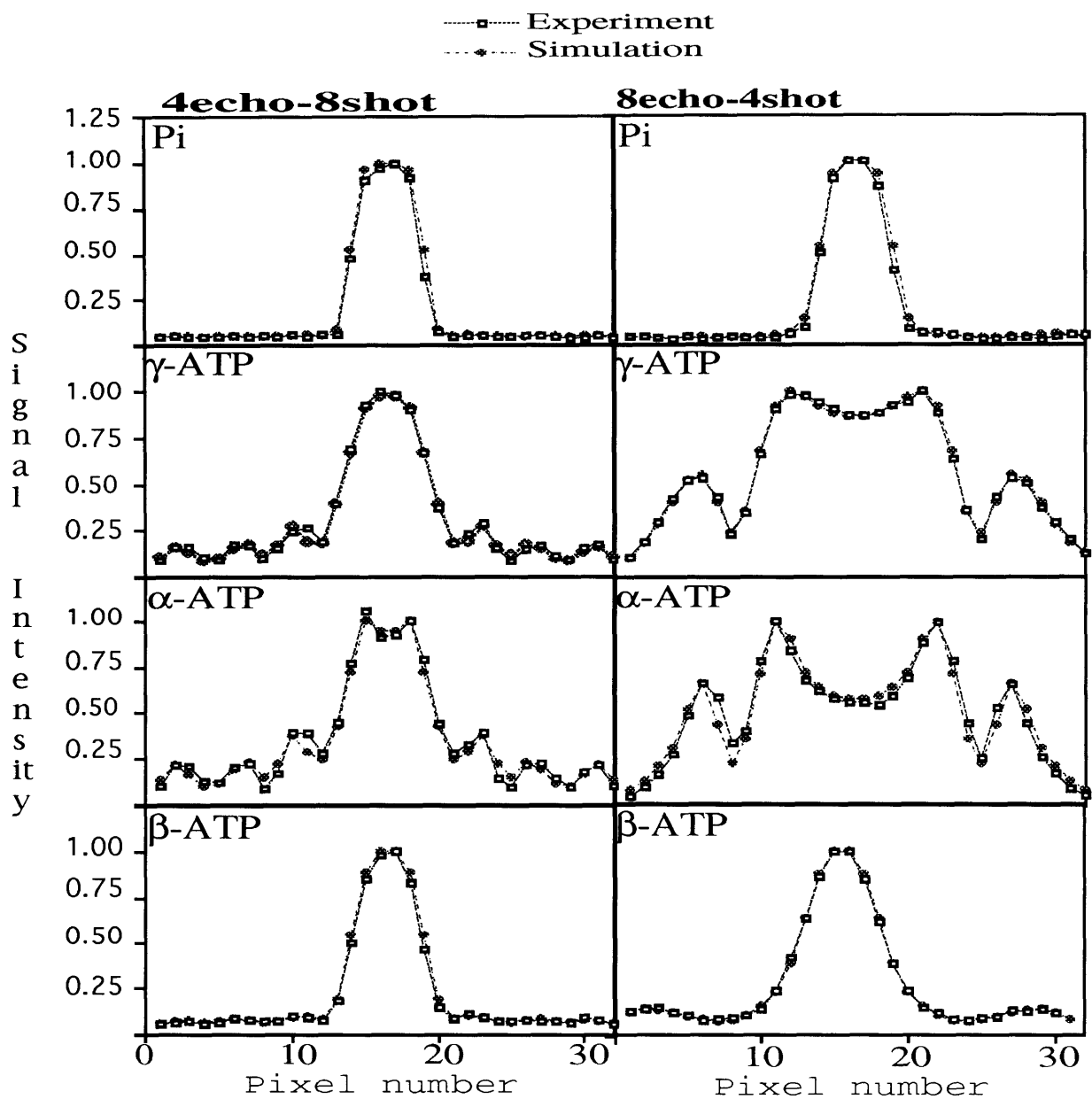


Figure 4.6. Experimental and spatial profiles extracted from the data sets of Figure 7 for each of the four  $^{31}\text{P}$  resonances. Also shown are simulated spatial profiles of a square phantom generated by taking into account both T2-decay and J-coupling effects.

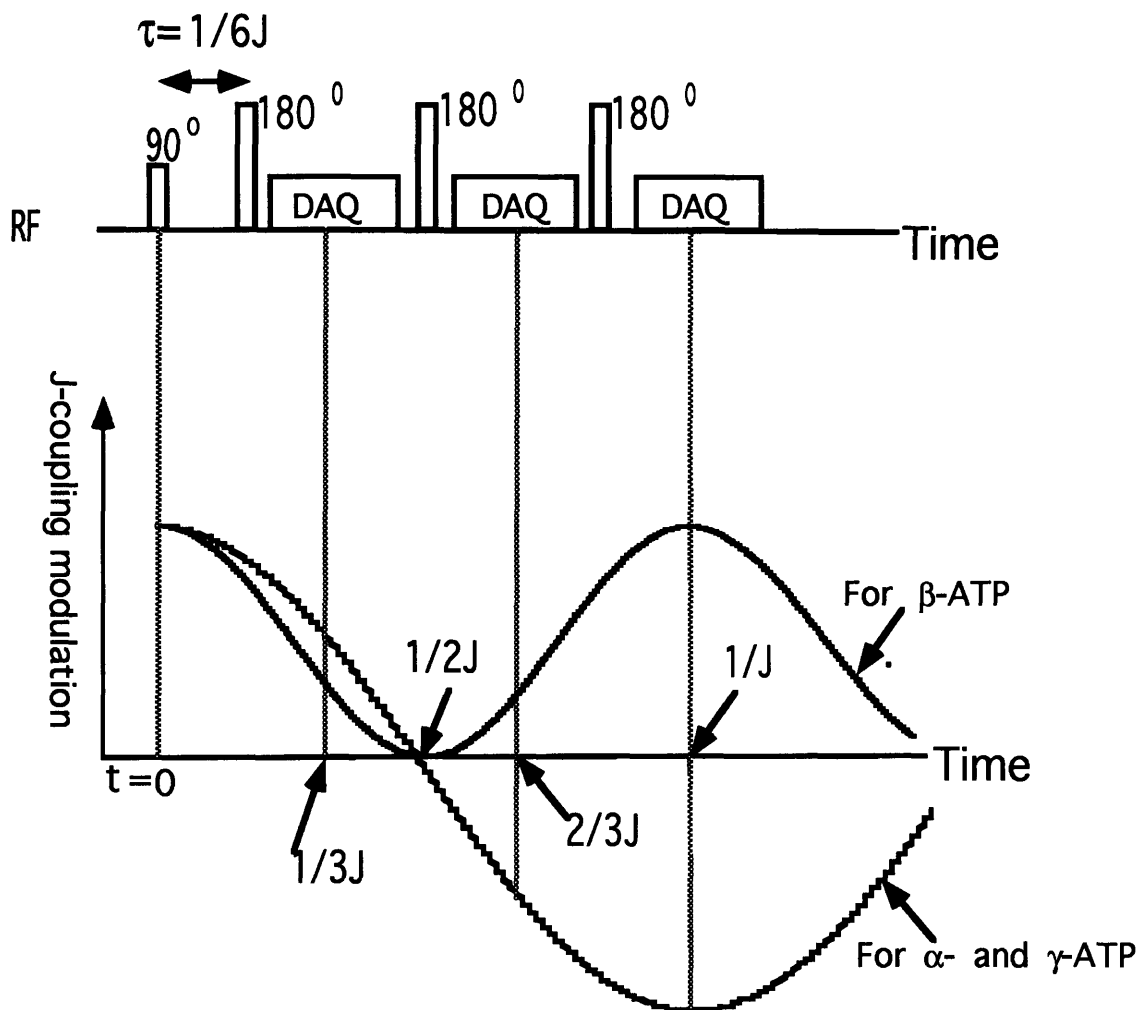
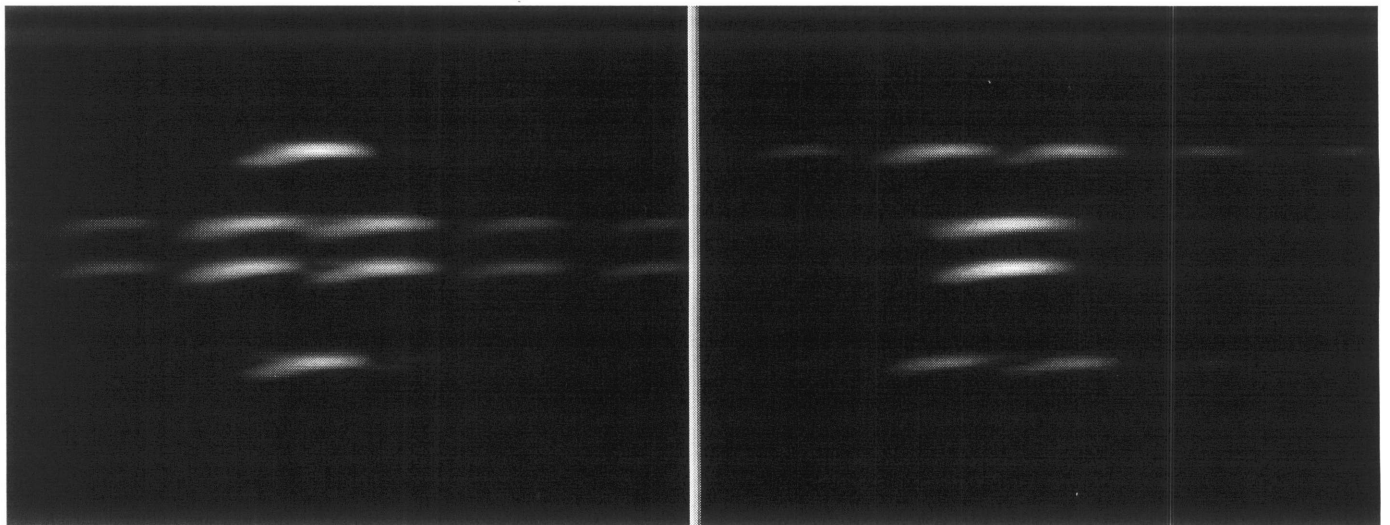


Figure 4.7. Reduced echo spacing sampling scheme used for in vivo acquisitions where ATP  $T_2$  values are smaller than in solution. An echo spacing of  $1/3J$  allows for the collection of three echoes avoiding J-coupling modulated zero's for all three resonances. An in vivo value of  $J$  of 16 Hz leads to a  $1/3J$  echo spacing of 20 ms.

spacing of  $1/3J$ . As shown in Figure 4.7 for a J-coupling constant of 16 Hz, this sampling scheme avoids signal nulls at the echo time of  $1/2J$  while achieving a third echo with maximal signal intensity for all three peaks (positive for  $\beta$  and negative for  $\alpha$  and  $\gamma$ ). Figure 4.8 shows 3-echo RARE images of the ATP phantom acquired with this scheme using an echo spacing of  $1/3J$  of 17 ms. The image in Figure 4.8 a was acquired in only 20 seconds using a 2 s TR, 15 phase encodes and two signal averages and reconstructed directly from the raw data without any post-processing. Though all resonances are clearly resolved even with the 15 ms readout, considerable spatial ghosting is observed for the  $\alpha$  and  $\gamma$  resonances. Figure 4.8 b shows the image processed from the same data but with appropriate k-space lines corrected according to Eq 4 for the  $\alpha$  and  $\gamma$  resonances. As in the simpler cases above, the corrections remove the spatial misregistration (ghosts) of the  $\alpha$  and  $\gamma$  resonances, introducing of course, spatial misregistration for the Pi and  $\beta$  peaks.

#### 4.2 In vivo experiment

We applied the three echo,  $1/3J = 20$  ms echo space sampling scheme of Figure 9 to map  $^{31}\text{P}$  spectra through a live mouse. The mouse was oriented vertically in the horizontal bore of the magnet and phase encoding proceeded from bottom to top along the entire body of the mouse. Figures 4.9 a and b show three echo RARE SI data sets of the mouse before and after k-space post-processing corrections for ATP J-coupling effects, respectively. Post-processing according to Eq 4 was performed to correct for  $\alpha$  and  $\gamma$  spatial misregistration using a J of 16 Hz. The acquisition parameters were a TR of 1.1 s, 15 phase encodes and 64 signal averages with a total scan time of 5 minutes and 52 seconds. Note how the k-space correction (Figure 4.9 b) resulted in a significant reduction of the spatial spread of the ATP resonances while introducing phase encode blur and ghosting to the uncoupled resonances PCr, Pi and the PME bands. In both data sets, however, all the standard



**a.**

**b.**

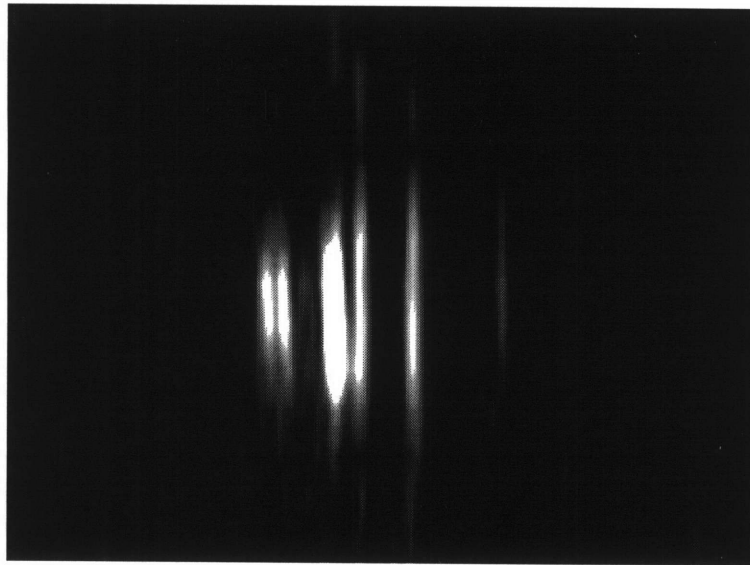
Figure 4.8. a. A three-echo RARE image of the ATP phantom using a  $1/3J = 17$  ms echo spacing. Misregistration along the spatial direction is quite severe for the  $\alpha$  and  $\gamma$ -ATP resonances. b. Same image as in a but with k-space correction scheme based on Eq 4 for the  $\alpha$  and  $\gamma$  resonances which now show no ghosting (ghosting now transferred to Pi and  $\beta$  bands).

$^{31}\text{P}$  metabolites are observed. Representative spectra extracted from horizontal profiles through the center of Figures 4.9 a and b are provided in Figures 4.9 d and e. Figure 4.9 c is a conventional 1D SI of the same mouse acquired using a single  $90^\circ$  pulse followed by a 0.5 ms phase encoding step, a 128 ms FID readout, a 1.1 s TR and 64 signal averages per phase encode. The total scan time for the conventional SI was thus three times longer than the RARE SI acquisition (17 minutes and 36 seconds). All the spectral bands are more intense in the conventional SI due to the short delay to data acquisition compared to the 20 ms effective echo time of the RARE mode acquisition. Spatial mapping in the conventional SI data set shows only the standard blurring due to the small number of phase encode steps. Peak signal-to-noise ratios for the Pi, PCr, and ATP resonances were measured using peak heights and average baseline noise values taken from the spectra shown in Figures 4.9 d - f. The results are given in Table 1. Note that for the RARE mode acquisitions, Pi and PCr signal-to-noise values were measured from the uncorrected data set while the signal-to-noise for the ATP peaks were measured from the k-space corrected data set.

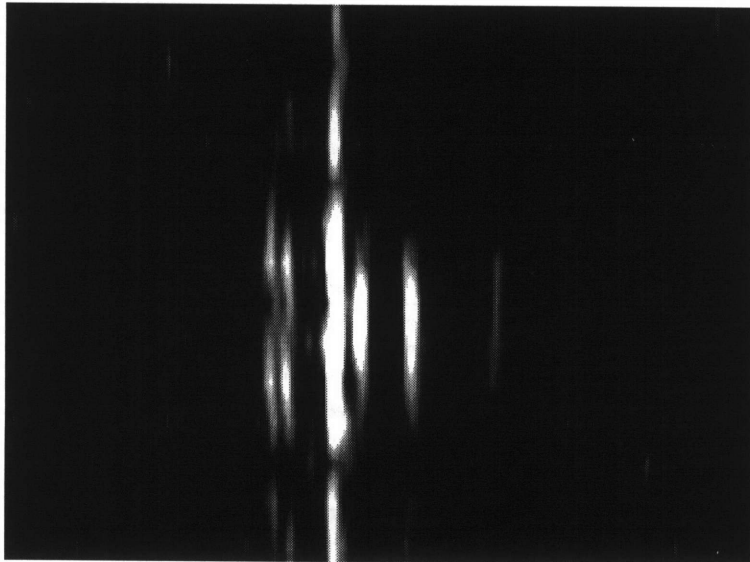
By cutting and pasting, shown in Figure 4.10 is a SI which provides correct spatial mapping for all metabolites obtained from both raw RARE SI (for Pi, PCr) and processed RARE SI (for ATP resonances esp.  $\alpha$ - and  $\gamma$ -ATP).

	RARE SI	Processed RARE SI	Conventional SI
Pi	6.5	N/A	7.3
PCr	20	N/A	21
$\gamma$ -ATP	N/A	9.8	19
$\alpha$ -ATP	N/A	9.2	27
$\beta$ -ATP	2.5	3.4	25

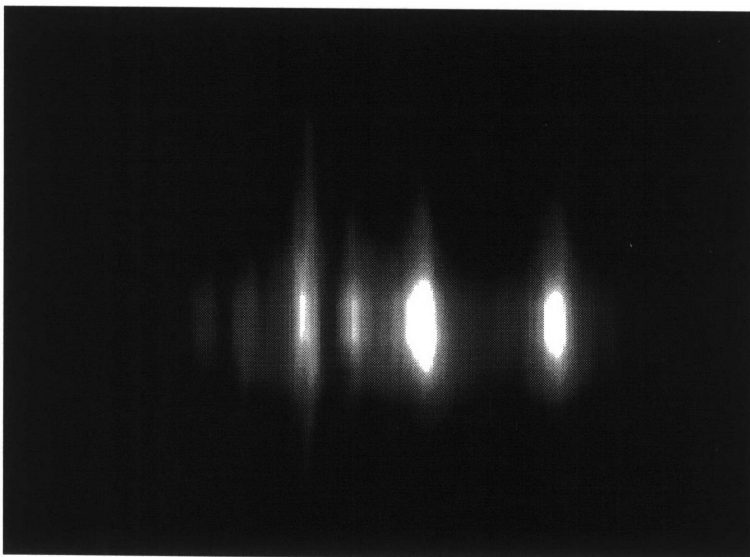
Table 1: The signal-to-noise ratios of the five major  $^{31}\text{P}$  resonances estimated from the three-echo RARE mode SI data sets and the conventional SI data set of the live mouse extracted from the spectra in Figures 4.9 d - f.



a.



b.



c.

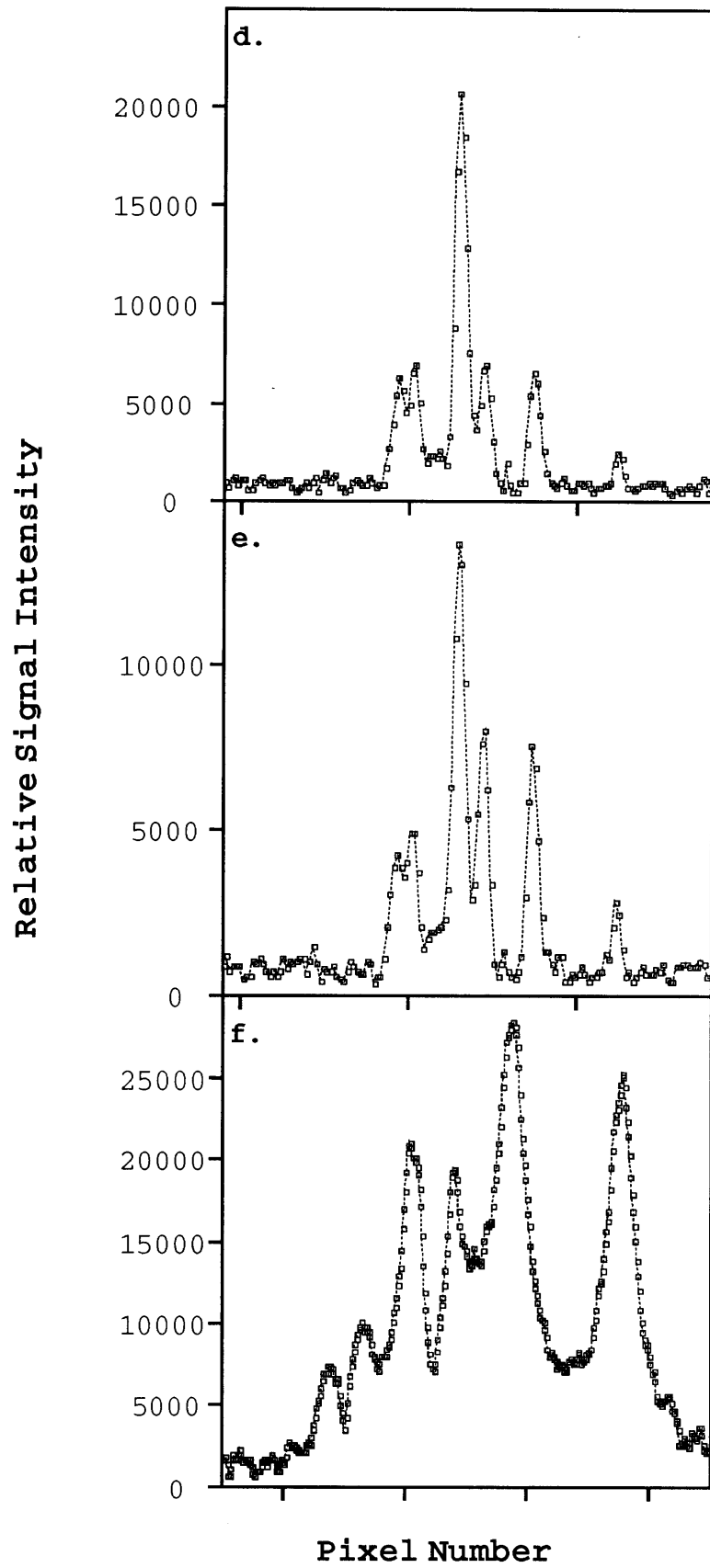
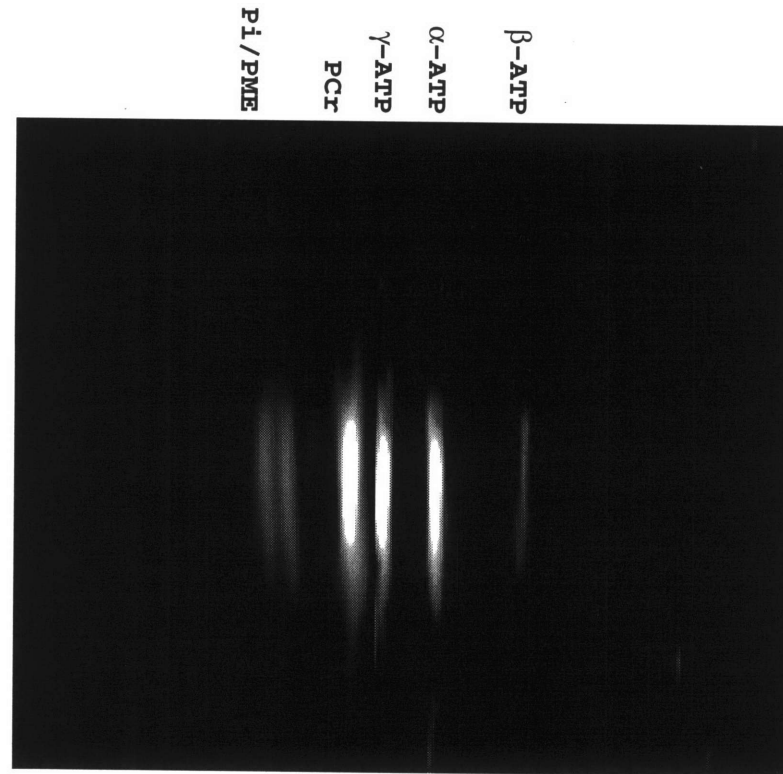
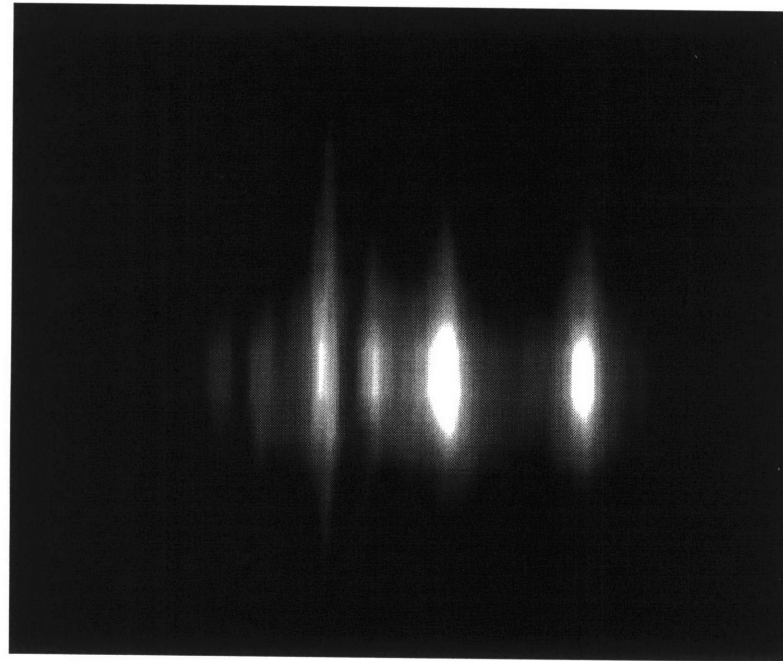


Figure 4.9 ( previous two pages). Three echo RARE mode SI's (a,b) and a conventional SI (c) of a live mouse along with representative spectra extracted from these data sets (d,e,f). The RARE mode acquisition was acquired in 5 minutes and 52 seconds while the conventional SI took 17 minutes and 36 seconds. The  $1/3J = 20$  ms echo spacing scheme shown in Figure 4.7 was used for the RARE mode acquisition and (a) is the direct reconstruction of k-space data in which the vertical axis is spatial from bottom to top (head) of the vertically oriented mouse and the horizontal axis is spectral. The observable bands are (from left-to-right) PME and Pi, PCr,  $\gamma$ ,  $\alpha$  and  $\beta$ -ATP. Ghosting due to J-coupling modulations along the spatial direction are seen for the  $\alpha$  and  $\gamma$  peaks and to a lesser degree the  $\beta$  peak. (b) Same RARE SI data set but reconstructed from k-space data processed according to Eq. 4 and the assumption of  $J_{\alpha\beta} = J_{\beta\gamma} = J = 16\text{Hz}$ . Note the reduction in spatial ghosting for the ATP peaks in (b) due to the post-processing which then introduces ghosting to the uncoupled resonances. The spectral bands from the conventional SI show only standard spatial ghosting associated with the use of only 16 phase encode steps and all the peaks are more intense due to FID acquisitions. The spectra in d-f were used to make signal-to-noise comparisons between the RARE and conventional SI's (Table 1). The dotted lines connect the actual sampled spectral points to improve visualization.



RARE SI  
a.



Conventional SI  
b.

Figure 4.10 a. By cutting and pasting of Fig. 4.9a and 4.9b, correct spatial mapping can be obtained for PCr, Pi and  $\alpha$  and  $\gamma$  resonances which agrees with the conventional SI shown in b. b. the SI acquired with conventional approach.

## Chapter 5

### Discussion

Spectroscopic imaging of the  $^{31}\text{P}$  resonances of ATP may ultimately benefit from multi-echo acquisitions to reduce scan times. The use of short echo readouts to capture usable echoes within the 100 ms or so  $T_2$  decay envelopes reported in vivo will require high fields which yield a greater spectral dispersion. With echo readouts as short as 17 ms, the primary resonances of in vivo  $^{31}\text{P}$  spectra are reasonably well-resolved at 4.7 T (Figure 4.9), arguing for the feasibility of multi-echo acquisitions.

The AMX J-coupling spin echo amplitude modulations of ATP resonances become important factors affecting the image quality of RARE mode acquisitions. We have shown in simple ATP phantoms that using an echo spacing of  $1/J = 52$  ms allows for simple k-space processing schemes which can correct for spatial misregistrations arising from the J-coupling effects. Namely, the spatial profiles of  $\alpha$  and  $\gamma$  resonances can be reconstructed without ghosting artifact by multiplying odd echo k-space lines by -1. Separate reconstructions for the different resonances may be performed and a final image with no misregistration artifacts may readily be generated by piecing together different frequency bands from the separate reconstructions.

The shorter  $T_2$  values of ATP in vivo (Straubinger et al, 1994, Jung et al, 1992, 1993, 1996) make use of  $1/J$  echo spacings problematic. We therefore employed an echo spacing of  $1/3J$  to generate 3 echo RARE mode SI data sets of a living mouse. The correction schemes for the k-space data based upon the general formulation given by Eq 4 served to reduce spatial misregistration of ATP peaks due to the J-

coupling (Figure 4.9). In this regard we note the importance of the perfect flip angle assumption we have made. Namely, in this work departures from  $90^\circ$  and  $180^\circ$  flip angles for the CPMG RF pulses were minimized by using "hard" pulses, allowing for use of the formalism embodied by Eq's 2 - 4 to account for J-coupling. If section selective RF pulses are used as part of the spatial localization process, the effects of a distribution of flip angles across the section must be considered. Straubinger et al have discussed this problem in some detail (1994 ) and have demonstrated the departure from the simple AMX behavior predicted by Eq 4 when non-ideal flip angles are employed. Though the effects can be evaluated theoretically, they are considerably more complex than those obtained under idealized CPMG conditions.

The acquisition of a standard SI data set of the mouse (Figure 4.9 c,f) allowed us to make a preliminary assessment of the impact on in vivo  $^{31}\text{P}$  spectral quality traded for the factor of 3 decrease in scan time associated with a 3-echo RARE mode acquisition (Table 1). Interestingly, the signal-to-noise ratio of the PCr and Pi signals were only minimally affected by the factor of three scan time decrease associated with the RARE acquisition, presumably due to their long T2 values in vivo. This finding implies that in vivo pH measurements using the frequency separation between these two uncoupled resonances may be facilitated using a fast RARE sequence approach, though probably with longer echo spacings to increase the spectral resolution and accuracy of the measurement. The ATP resonances, though clearly observed at quantifiable signal-to-noise levels in the RARE mode data sets, had signal-to-noise ratios smaller than those observed in the conventional SI data set. We attribute this decrease in signal to the relatively short ATP T2 values and to J-coupling effects. Though the effects of these factors on the spatial mapping can be accounted for and corrected, they do result in lower signal-to-noise ratios for ATP resonances in RARE mode acquisitions compared to conventional SI.

In summary, the experiments and theoretical analyses we have performed indicate that it is feasible to use multi-echo approaches for  $^{31}\text{P}$  in vivo NMR studies as a scan time reduction strategy at 4.7 T. Disadvantages compared to conventional SI methods include the usual T2-degradation of spatial mapping found with multi-echo phase encoding methods (Hennig et al, 1986, Mulkern et al., 1990, 1991), reduced spectral resolution, the need to account for J-coupling effects among the ATP nuclei on spatial mapping, and reduced ATP signal intensities. Further work is required to determine the extent to which these disadvantages offset the decreased scan times attainable with multi-echo techniques for specific applications in different organs.

## Appendix I: A numerical calculation of the AMX density operator formalism.

```
clear
% clg
hold off
AMXspin;

Q=pi/2;
R1=expm3(-i*Q*(Ax+Kx+Mx));
R11=expm3(i*Q*(Ax+Kx+Mx));
D0=R1*(Az+Kz+Mz)*R11;

Q=pi;
R2=expm3(-i*Q*(Ay+Ky+My));
R22=expm3(i*Q*(Ay+Ky+My));

Q=pi/2;
R3=expm3(-i*Q*(Ay+Ky+My));
R33=expm3(i*Q*(Ay+Ky+My));

%Hamiltonian of the system:
N=1024;

S=zeros(N,1);
%w is the chemical shift of the nuclei
w1=0;
w2=0;
w3=0;
J12=19;
J23=19;
J13=0;

%The Hamiltonian of the system
H=w1*Az+w2*Mz+w3*Kz+J12*Az*Mz+J23*Mz*Kz+J13*Az*Kz;

J=J12;
TE=1/(J);
tau=1/(4*J);

U0=expm3(-i*H*tau*pi^2);
U1=expm3(-i*H^4*tau*pi^2);
U00=expm3(i*H*tau*pi^2);
U11=expm3(i*H^4*tau*pi^2);
SW=3000;
T=N/SW; %the readout time; there is SW=N/T;
dT=1/SW;
for k=1:N
```

```

t=tau+(k-1)*dT;
U=expm3(-i*H*t*pi*2);
UU=expm3(i*H*t*pi*2);
D1=U*R2*U0*D0*U00*R22*UU;

D=U*R2*U1*R2*U1*R2*U1*R2*U0*D0*U00*R22*U11*R22*U11*R22*U11*R22*UU;

M1=(Ax+i*Ay)*D1;
M2=(Mx+i*My)*D1;
M3=(Kx+i*Ky)*D1;
% M=((Ax+Kx+Mx)+i*(Ay+Ky+My))*D;
S1(k)=trace(M1);%*exp(-t/0.5);;
S2(k)=trace(M2);%*exp(-t/0.5);
S3(k)=trace(M3);%*exp(-t/0.5);
k
end

subplot(3,2,1), plot(real(S1));
subplot(3,2,2), plot(imag(S1));          subplot(3,2,3), plot(real(S2));
subplot(3,2,4), plot(imag(S2));
subplot(3,2,5), plot(real(S3));
subplot(3,2,6), plot(imag(S3));

%*both expm1 and expm3 works, the expm3 seems the fastest
%*the expm2 works when t is very small, error occur when t is bigger
%*than certain value.
%*expm1 takes about 3 minutes
% |          ||          |
% | 90x<----tau----> | 180y<----tau----> readout for D1
% |          ||          |
% |          ||          ||          ||          |
% | 90x<--tau--> | 180y<--tau--> 90y<--tau--> 180y<--tau--> readout for D2
% |          ||          ||          ||          |

Functions:

1. AMXspin:

%AB system spin matrix for spin of 1/2:
%A=Ix*I0*I0;
%K=I0*Ix*I0;
%M=I0*I0*Ix;

clear
Paulispin;

```

A=Ix;  
B=I0;  
C=I0;  
directprod1;  
Ax=E;

A=Iy;  
B=I0;  
C=I0;  
directprod1;  
Ay=E;

A=Iz;  
B=I0;  
C=I0;  
directprod1;  
Az=E;

A=I0;  
B=Ix;  
C=I0;  
directprod1;  
Mx=E;

A=I0;  
B=Iy;  
C=I0;  
directprod1;  
My=E;

A=I0;  
B=Iz;  
C=I0;  
directprod1;  
Mz=E;

A=I0;  
B=I0;  
C=Ix;  
directprod1;  
Kx=E;

A=I0;  
B=I0;  
C=Iy;  
directprod1;

```

Ky=E;

A=I0;
B=I0;
C=Iz;
directprod1;

Kz=E;

```

## 2. Paulispin;

%Pauli spin matrix for spin of 1/2:

```

I0=zeros(2,2);
Ix=zeros(2,2);
Iy=zeros(2,2);
Iz=zeros(2,2);

```

```

I0(1,1)=1;
I0(2,2)=1;

```

```

Ix(1,2)=1;
Ix(2,1)=1;

```

```

Iy(1,2)=-i;
Iy(2,1)=i;

```

```

Iz(1,1)=1;
Iz(2,2)=-1;

```

```

Ix=Ix/2;
Iy=Iy/2;
Iz=Iz/2;

```

## 3. Direct Production Operation:

```

[m,n]=size(A);
[mI0,nI0]=size(B);
[mI1,nI1]=size(C);
for l=1:m
for k=1:n
D((l-1)*mI0+1:l*mI0,(k-1)*nI0+1:k*nI0)=A(l,k)*B;
end
end

[mI2,nI2]=size(D);

```

```
for l=1:mI2
for k=1:nI2
E((l-1)*mI1+1:l*mI1,(k-1)*nI1+1:k*nI1)=D(l,k)*C;
end
end
```

## Appendix II: Simulation of J-coupling effect on the spatial mapping in case of

$TE=n/J$ .

### a. simulation of the J modulation in the case four echo RARE SI

```
%initialization
```

```
clear
```

```
hold off
```

```
% the phantom
```

```
length=32;
```

```
psize=5;
```

```
p(1:length)=zeros(1,length);
```

```
shift=1;
```

```
p(length/2-psize/2+shift:length/2+psize/2-1+shift)=ones(1:psize);
```

```
L=1:1:length;
```

```
%subplot(3,2,1),plot(p);
```

```
%axis([1 length 0 1.2]);
```

```
%title('the phantom');
```

```
%input the general parameter
```

```
N=length;
```

```
T2pi=300/1000;
```

```
T2alpha=134/1000;
```

```
T2beta=180/1000;
```

```
T2gamma=98/1000;
```

```
FG=1/N;
```

```
%The J coupling effect
```

```
J12=19.3;
```

```
J23=19;
```

```
J13=0;
```

```
TE=58.8/1000;
```

```
NECHO=4;
```

```
f=-0.25; %the place where the phase encoding start
```

```
j0=(f+1)*N/2+1;
```

```
np=N/NECHO;
```

```
%A:The rare mode, T is the signal in time domain
```

```
for k=1:NECHO
```

```
theta1=pi*TE*k*(J12-J13);
```

```

theta2=pi*TE*k*(J12+J13);
FJalpha=(cos(theta1)+cos(theta2))/2;
theta1=pi*TE*k*(J23-J12);
theta2=pi*TE*k*(J23+J12);
FJbeta=(cos(theta1)+cos(theta2))/2;
theta1=pi*TE*k*(J13-J23);

theta2=pi*TE*k*(J13+J23);
FJgamma=(cos(theta1)+cos(theta2))/2;

for m=1:np
J=j0+m-1;

    while J > N
    J=J-N;
    end

L=1:1:length;
%x=FG*(J-N/2-1)*(x-length/2-1)*2*pi;
x=2*pi*FG*(J-N/2-1)*L; %it is very important to realize that the J should
d be changed to (J-N/2-1)

TDalpha(J)=exp(-k*TE/T2alpha)*FJalpha/2;
TDbeta(J)=exp(-k*TE/T2beta)*FJbeta/2;

Tpi(J)= sum(p.*exp(-i*x))*exp(-k*TE/T2pi);
Talpha(J)= sum(p.*exp(-i*x))*exp(-k*TE/T2alpha)*FJalpha;
Tbeta(J)= sum(p.*exp(-i*x))*exp(-k*TE/T2beta)*FJbeta;
Tgamma(J)= sum(p.*exp(-i*x))*exp(-k*TE/T2gamma)*FJgamma;
end

j0=j0+np;
end

SPpi=abs(iff(Tpi));
SPalpha=abs(iff(Talpha));
SPbeta=abs(iff(Tbeta));
SPgamma=abs(iff(Tgamma));

y=1:1:length;

subplot(3,2,1),plot(SPpi);
axis([1 length 0 1.0]);
title('The Pi, assuming T2=300ms');
subplot(3,2,2),plot(SPalpha);
axis([1 length 0 0.4]);

```

```

    title('The ATP alpha, assuming T2=130ms');
    subplot(3,2,3),plot(SPbeta);
    axis([1 length 0 0.5]);
    title('The ATP beta, assuming T2=120ms');
    subplot(3,2,4),plot(SPgamma);
    axis([1 length 0 0.3]);
    title('The ATP gamma, assuming T2=90ms');
    subplot(3,2,5),plot(L,TDalpha, '.');

axis([1 length -0.5 0.5]);
    title('Phase encoding of alpha and gamma');
    subplot(3,2,6),plot(L,TDbeta, '.');
    axis([1 length 0 0.5]);

    title('Phase encoding of beta');

```

### **b. simulation of the J modulation in the case eight echo RARE SI**

```
%initialization
```

```
clear
```

```
hold off
```

```
% the phantom
```

```

    length=32;
    psize=5.5;
    p(1:length)=zeros(1,length);
    shift=-.5;
    x=-psize/2:1:psize/2-1;
    px=sqrt(psize*psize/4-x.*x);
    p(length/2-psize/2+shift:length/2+psize/2-1+shift)=px(1:psize)/(psize/2)
;
    p(length/2-psize/2+shift:length/2+psize/2-1+shift)=ones(1:psize);
    L=1:1:length;
    %subplot(3,2,1),plot(p);
    %axis([1 length 0 1.2]);
    %title('the phantom');

```

```
%input the general parameter
```

```

    N=length;
    T2pi=300/1000;
    T2alpha=134/1000;
    T2beta=180/1000;
    T2gamma=98/1000;
    FG=1/N;
    %The J coupling effect

```

```

J12=19.3;
J23=19.3;
J13=0;

TE=1/19;

NECHO=8;

np=N/NECHO;

%A:The user defined mode, T is the signal in time domain
for k=1:NECHO
J1=N/2+np*(k-1)/2+1;
J2=N/2-np*(k-1)/2;
theta1=pi*TE*k*(J12-J13);

theta2=pi*TE*k*(J12+J13);
FJalpha=(cos(theta1)+cos(theta2))/2;
theta1=pi*TE*k*(J23-J12);
theta2=pi*TE*k*(J23+J12);
FJbeta=(cos(theta1)+cos(theta2))/2;
theta1=pi*TE*k*(J13-J23);
theta2=pi*TE*k*(J13+J23);
FJgamma=(cos(theta1)+cos(theta2))/2;
np2=np/2;
for m=1:np2

J=J1+(m-1);
L=1:length;
%x=FG*(J-N/2-1)*(L-length/2-1)*2*pi;
x=2*pi*FG*(J-N/2-1)*L;
%it is very important to realize the J should be J-N/2-1 as the phase encoding g
oes from -Kmax to +Kmax;
TDalpha(J)=exp(-k*TE/T2alpha)*FJalpha;
TDbeta(J)=exp(-k*TE/T2beta)*FJbeta;

Tpi(J)= sum(p.*exp(-i*x))*exp(-k*TE/T2pi);
Talpha(J)= sum(p.*exp(-i*x))*exp(-k*TE/T2alpha)*FJalpha;
Tbeta(J)= sum(p.*exp(-i*x))*exp(-k*TE/T2beta)*FJbeta;

Tgamma(J)= sum(p.*exp(-i*x))*exp(-k*TE/T2gamma)*FJgamma;
J=J2-(m-1);
%x=FG*(J-N/2-1)*(L-length/2-1)*2*pi;
x=2*pi*FG*(J-N/2-1)*L;
TDalpha(J)=exp(-k*TE/T2alpha)*FJalpha;

```

```

TDbeta(J)=exp(-k*TE/T2beta)*FJbeta;

Tpi(J)= sum(p.*exp(-i*x))*exp(-k*TE/T2pi);
Talpha(J)= sum(p.*exp(-i*x))*exp(-k*TE/T2alpha)*FJalpha;
Tbeta(J)= sum(p.*exp(-i*x))*exp(-k*TE/T2beta)*FJbeta;
Tgamma(J)= sum(p.*exp(-i*x))*exp(-k*TE/T2gamma)*FJgamma;

end
j0=j0+np;
end

SPpi=abs(iff(Tpi));
SPalpha=abs(iff(Talpha));
SPbeta=abs(iff(Tbeta));
SPgamma=abs(iff(Tgamma));

y=1:1:length;

subplot(7,5,1),plot(SPpi);
axis([1 length 0 0.9]);
set(gca,'XTick',[],'YTick',[])
% title('The Pi, assuming T2=300ms');
subplot(7,5,11),plot(SPalpha);
axis([1 length 0 0.8]);
set(gca,'XTick',[],'YTick',[])
% title('The ATP alpha, assuming T2=130ms');
subplot(7,5,16),plot(SPbeta);
axis([1 length 0 0.9]);
set(gca,'XTick',[],'YTick',[])
% title('The ATP beta, assuming T2=120ms');
subplot(7,5,6),plot(SPgamma);
axis([1 length 0 0.65]);
set(gca,'XTick',[],'YTick',[])
% title('The ATP gamma, assuming T2=90ms');
% subplot(3,2,5),plot(L,TDalpha,');
% axis([1 length -1 1]);
% title('Phase encoding of alpha and gamma');
% subplot(3,2,6),plot(L,TDbeta,');
% axis([1 length 0 1]);
% title('Phase encoding of beta');

```

## **Part II**

### **Fast PCr Imaging: Feasibility of Monitoring Muscle metabolism**

The goal of this part of my research is to evaluate the feasibility of fast phosphocreatine(PCr) magnetic resonance imaging technique and to apply PCr based imaging studies to the metabolic response to exercise in skeletal muscle.

## **Introduction:**

Nuclear magnetic resonance(NMR) spectroscopy and spectroscopic imaging allow the non-invasive study of energy regulation and metabolism in human skeletal muscle(Kent-Braun et al, 1990, Jenson et al 1993, 1996, Nelson et al, 1991, Ernst et al, 1993, Kushmerick et al, 1985, 1987, 1992, 1995). However, Magnetic Resonance Spectroscopy(MRS) provides limited spatial information and conventional spectroscopic imaging which provides both chemical and spatial information is often a lengthy procedure(Mora et al. 1991, Tsuji et al, 1996) and subsequently limits the clinical application. In our study, instead of looking at whole spectrum of  $^{31}\text{P}$  containing metabolites, we concentrate on one critical important molecule: phosphocreatine (PCr) whose level reflects the metabolic state so as to shorten the scan time providing suitable temporal resolution for the studies of energy metabolism.

In the transition from rest to work, adenosine triphosphate(ATP) turnover rate in skeletal muscle may increase as much as several orders of magnitude. Under most physiological conditions, muscle ATP concentrations do not change while phosphocreatine (PCr) declines during prolonged or repeated contractions (Kent-Braun et al, 1990, Kushmerick et al, 1987). The resting muscle restores ATP and PCr concentration depending on the rate of oxidative phosphorylation controlled by the ADP concentration (Kushmerick et al, 1992, Chance et al., 1986). The physiology of glycolysis and oxidative phosphorylation, regulation of blood flow, and the physiology of ATPase activities and muscle contraction differ in different muscle cell types which have different mixtures of predominantly aerobic (slow fibers) or predominantly glycolytic (fast fibers)(Kushmerick et al, 1992).

In skeletal muscle, the Creatine Kinase(CK) catalyzed reaction is thought to function primarily as an energy reserve for rapid resyntheses of ATP, where ATP is

regenerated from ADP and PCr. Repetitive contractions produce an initial decrease in PCr with a decrease in ATP seen only with very high rate of contraction (Kushmerick et al, 1992). Previous MR spectroscopic studies have shown during muscle contraction, inorganic phosphorus (Pi) peak area increases to approximately to the same extent as PCr decreases (Burt et al, 1976, Nelson et al. 1991, Kushmerick et al, 1992). The Creatine Kinase catalyzed reaction is much faster than the rate of oxidative phosphorylation (Stryer, 1988), therefore the PCr drop during muscle contraction provides a measure of energy consumption.

The long T2 of PCr ( ~ 400 ms) (Thomsen et al, 1989, Jung et al, 1992) allows application of multi-echo NMR techniques for fast PCr imaging (Hennig et al, 1986, Jones et al, 1992 ). The Rapid Acquisition with Relaxation Enhanced (RARE) technique collects multiple spin-echoes for each excitation . A distinct spatial phase encoding step is applied for each echo. Scan times are reduced compared to conventional imaging by a factor equal to the number of echoes collected per excitation using this multi-echo technique (Hennig et al, 1986, Jones et al, 1992, Mulkern et al, 1991). Thus, a multi-echo techniques could provide a better temporal resolution for the study of ATP metabolism.

A RARE technique has been developed to measure the distribution of PCr in the forearm with suitable temporal resolution. The changes of PCr level were observed through a time course of rest, exercise and recovery.

## Chapter 1

### Background

In this chapter previous studies of PCr are reviewed briefly with emphasis on those aspects most relevant to this research.

#### 1.1 Phosphocreatine(PCr) in biological system

The involvement of Phosphocreatine(PCr) in energy metabolism has been known for a long time. PCr is another metabolite containing high energy bonds along with ATP in a cell. The structure of PCr, ATP, ADP and AMP and their resonances in NMR spectra are shown in Figure 1.1. Creatine Kinase (CK) catalyzes the reversible transfer of a phosphoryl group from PCr to ADP to form ATP. The amount of PCr present in a cell depends on the cell type (Tsuji et al. , 1996, Hochachka, 1994, Stryer, 1988). In human beings, PCr is mainly present in skeletal muscles, myocardium and brain. The mechanisms controlling storage amounts are unknown, although the feedback repression of synthesis in the liver may limit total availability at these sites (Walk, 1979).

The total pool sizes of PCr + Cr are around 30 mM in muscles; higher in fast-twitch muscles and lower in slow muscles and myocardium (Kushmerick et al, 1992). On a short- and long-term basis, the amount of PCr available for high power output is related to the hypertrophy of the muscle and this adaptation mechanism seems limited to fast-twitch muscles (Holloszy et al., 1976). PCr reduction has been observed in dystrophic muscle (MuCully et al. 1991, Lane et al. 1989).

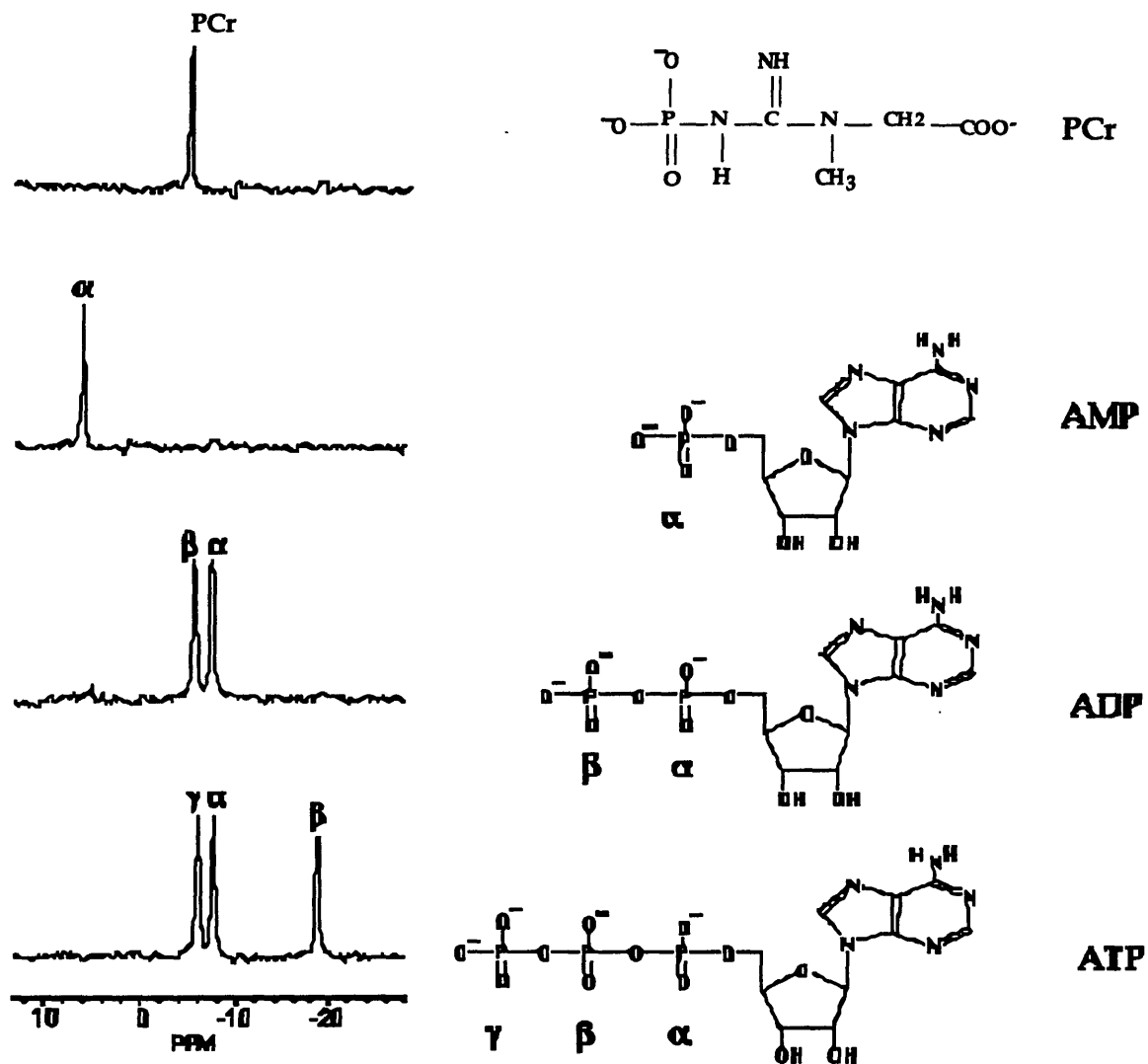
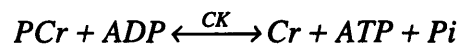


Figure 1.1 The structure of the high energy metabolites: PCr, ATP, ADP and AMP and their resonances in NMR spectroscopy. In resting muscle, typical concentrations of the metabolites are  $[PCr] = 25 \text{ mM}$ ,  $[ATP] = 4 \text{ mM}$ ,  $[ADP] = 0.013 \text{ mM}$  and insignificant amounts of AMP.

## 1.2 PCr level reflects the metabolic changes in patho-physiologic processes

When a cell demands energy rapidly and in a large amount, energy is first released from ATP directly to functional elements of the cell. Then the energy stored in the PCr is used immediately to reform new adenosine triphosphate through CK catalization:



This reaction occurs much more rapidly than the oxidative reactions (aerobic or anaerobic) and provides a source of extra energy that can be used to keep the cell functioning at a high rate of metabolism for a short period of time.

For muscle, during the transition from rest to work, ATP cycling or turnover can increase by several orders of magnitude. Despite such large differences in ATP flux, ATP concentrations do not change much (Kushmerick 1985, 1987, Kent-Braun et al. 1990). The mechanism of sustaining high ATPase with minimal alternation in ATP level is through ATP resynthesis by CK in which high energy ~P is transferred from PCr to ADP (Hochachka, 1987). During muscle recovery period, ATP and phosphocreatine are resynthesized by metabolic oxidative process of metabolism. Several muscle physiology studies have suggested that the total phosphorus integral did not significantly change during stimulation; the change in PCr with steady state is equal and opposite to the Pi change, and recovery rates for PCr and Pi were similar (Kushmerick et al., 1992, Nelson et al., 1991). Therefore, the change of the PCr level itself provides an insight into ATP -ase rate during muscle contraction and ATP resynthetic rate during recovery.

My research therefore is aimed at observing muscle PCr changes with improved temporal and spatial resolution.

### **1.3 Previous PCr imaging**

In the last two decades, extensive studies related to  $^{31}\text{P}$  metabolites were mainly performed with NMR spectroscopy (MRS) or chemical shift imaging(CSI). One limitation associated with MRS is the amount of spatial information, as the signal is either from the whole sample or from a specific spatial location. Phosphorous Chemical Shift Imaging has the great advantage of providing chemical information as well as spatial information(Maudsley et al. 1990, Nelson et al. 1991, Jeneson et al. 1992, Frederick et al. 1995, Etherington et al, 1995 ). However, the scan time is often too long and unsuitable for the study of metabolic processes. Several groups have demonstrated the feasibility and potential of PCr imaging in the study of the patho-physiology process. Mora et al. (1991) proposed and demonstrated PCr image of monkey brains using chemical-shift discrimination RF pulse by selective excitation of PCr. PCr distributions were obtained before and after visual stimulation. Nelson et al. (1992) mapped the PCr distribution of the forearm by extracting the PCr signal from a 2-D spectroscopic image. The drawbacks of these two approaches are long-scan time and/or low spatial resolution. Using selective excitation or an extensive chemical shift artifact, Ernst et al. (1993) imaged PCr and Pi of the human forearm and brain, in which same phase encoding was given to a Carr-Purcell-Meiboom-Gill(CPMG, described in the next chapter) echo train following each excitation. Echoes were added up to signal average. The disadvantage associated with this technique is relatively lower efficiency (compared to other fast scan approaches) and sensitivity to motion. In a recent abstract, Greenman et al. (1996) suggested a new approach of  $^{31}\text{P}$  imaging using the multi-

echo approach. PCr imaging of the leg was acquired without discrimination of Pi and PCr and without slice selection under resting conditions.

Given the above drawbacks, our research is aimed at the improvement of this technique in the study of metabolic processes regarding Pi contamination and signal to noise ratio.

#### **1.4 Shortening PCr imaging time**

In vivo NMR measurement of the spin-spin relaxation time T2 and spin-lattice relaxation T1 of human skeletal muscle has been performed (Thomsen et al., 1990, Jung et al. 1992). The reported T2 value of PCr is in the 350 to 450 ms range and T1 in the 5 to 5.5 seconds range. The reported T2 value of Pi is in the 180 to 200 ms range and T1 in the 3 to 5 seconds range. Compared to other 31P containing metabolites, PCr has uniquely high T2 and T1 relaxation time( described in detail in the next chapter). The chemical shift difference between Pi and PCr is around 5.0 ppm or 400 Hz on the 4.7 T system.

Given its long T1 value, PCr imaging with traditional approach would be a lengthy procedure. However, because of its long T2, it would be advantageous to use multi-echo approach for shortening PCr imaging time.

#### **1.5 Summary**

Previous studies of skeletal muscle have shown that PCr decreases, Pi increases and ATP shows little or no change during different metabolic processes. Thus, changes in PCr and Pi reflect changes in the energy state of normal skeletal muscle. The rate of PCr recovery reflects, in part, the rate of ATP synthesis. On a 4.7 T magnet system Pi and PCr resonances are well separated (~400 Hz), which allows us to concentrate on monitoring PCr level by suppressing the Pi signal. Long T2 decay time makes fast scanning techniques such as Rapid Acquisition Relaxation-

Enhanced (RARE) method extremely useful in shortening the scan time of PCr imaging. In this fast scanning approach, multiple spin-echoes are collected following each excitation and each echo is used for a distinct spatial phase encoding step (Hennig et al. 1986, Mulkern RV et al 1990). Given the same repetition time TR and the number of phase encoding steps, scan time is reduced by factors equal to the number of echoes collected per excitation using the multi-echo approach. Thus fast PCr imaging with RARE indirectly provides regional measures of ATP metabolism with a temporal resolution suitable for physiological and clinical studies.

The goal of this part of my research is to evaluate the feasibility of a fast phosphocreatine(PCr) magnetic resonance imaging technique and to facilitate PCr based imaging studies of muscle metabolic response to exercise.

## Chapter 2

### NMR Theory

This chapter reviews the basic principles of MRI and some NMR techniques used in our study with emphasis on aspects most relevant to my research.

#### 2.1 MRI theory:

The signals in NMR are produced by an ensemble of the same nuclei. Spatial information is obtained by superimposing magnetic field gradients ( $\vec{G}$ ) on the static magnetic field. The magnetic field gradient is applied so that each nucleus will precess at a frequency proportional to the local magnetic field which is a linear function of spatial location  $\vec{r}$ :

$$f = \gamma B = \gamma(B_0 + \vec{G} \cdot \vec{r}) \quad (2.9)$$

Consider a generalized situation of a spin-density distribution  $\rho(x,y)$  measured in an NMR system having quadrature detection, in the presence of three orthogonal gradients. Following a  $90^\circ$  pulse and ignoring the relaxation, the signal obtained ( $S$ ) is:

$$\begin{aligned} S &\propto \iiint_{x,y,z} \rho(x,y) \exp(i2\pi \int f(x,y,z,t') dt') dx dy dz \\ &\propto \iiint_{x,y,z} \rho(x,y) \exp(i\gamma \int_0^t [xG_x(t') + yG_y(t') + zG_z(t')] dt') dx dy dz \end{aligned} \quad (2.10)$$

The above equation can be rearranged as:

$$S \propto \iiint_{x,y,z} \rho(x,y,z) \exp \left( \overbrace{ix \left\{ \gamma \int_0^t G_x(t') dt' \right\}}^{k_x} + \overbrace{iy \left\{ \gamma \int_0^t G_y(t') dt' \right\}}^{k_y} + \overbrace{iz \left\{ \gamma \int_0^t G_z(t') dt' \right\}}^{k_z} \right) dx dy dz \quad (2.11)$$

or

$$S(k_x, k_y, k_z) = \iiint_{x,y,z} \rho(x,y,z) \exp(ik_x x + ik_y y + ik_z z) dx dy dz \quad (2.12)$$

Therefore, by giving different gradient strength or giving different gradient on-time or accumulation time, signals  $S(k_x, k_y, k_z)$  which are also called K space data with different  $K_x, K_y, K_z$  are collected. By filling a 3-D  $S(k_x, k_y, k_z)$  data set or K space matrix, an image, which represents the nuclear density, can be obtained by the Fourier transform of the K space data set. This type of image is also called nuclear density weighted image.

Consider spin-spin relaxation, i.e. including the relaxation time, Equation 2.9 can be written as:

$$S(TE) \propto \iiint_{x,y,z} \rho(x,y,z) \exp\left(-\frac{TE}{T2(x,y,z)}\right) \exp\left(i\gamma \int_0^t [xG_x(t') + yG_y(t') + zG_z(t')] dt'\right) dx dy dz \quad (2.13)$$

or

$$S(k_x, k_y, k_z) \propto \iiint_{x,y,z} \rho(x,y,z) \exp\left(-\frac{TE}{T2(x,y,z)}\right) \exp(ik_x x + ik_y y + ik_z z) dx dy dz \quad (2.14)$$

where TE is the time between the 90° excitation pulse and the center of the readout. The Fourier transform of time domain signal will give:

$$\rho(x,y)\exp\left(-\frac{TE}{T2(x,y,z)}\right) \quad (2.15)$$

That is, the image intensity is weighted by the spin-spin relaxation time T2. The effect of T2 decay is related to the TE; the longer the TE, the heavier the image is weighted by T2. In practice, another mechanism which also causes the dephase of the spins and consequently the decay of transverse magnetization is the magnetic field inhomogeneity. The time constant which describes the actual observed decay of  $M_{xy}$  is  $T2^*$ . In the spin-echo sequence described in the following chapter, the dephasing induced by the field inhomogeneity is refocused at the center of the echo using  $180^\circ$  RF pulses.

In the case of a slice selected 2-D image, a shaped RF pulse is applied with the slice selecting gradient on. The slice selecting gradient causes magnetization precessing at a frequency related to its spatial position. Shaped RF pulses have limited bandwidth; only magnetization whose precessing frequencies are within that bandwidth will be excited and flipped to the transverse direction. Under this condition, gradients along the remaining of two dimensions are applied to fill a 2-D K space, and a two dimensional image will be obtained.

## 2.2 Spin-echo and multi-echo technique

Spin-echo pulse sequence consists of a single  $90^\circ$  pulse followed by one  $180^\circ$  pulse. These two RF pulses are separated by time interval  $TE/2$ . Another time interval of  $TE/2$  is also given between the  $180^\circ$  pulse and echo readout. TE, therefore, stands for echo time which is the time interval between the  $90^\circ$  excitation pulse and the center of the readout. The  $90^\circ$  RF pulse flips the net magnetization vector into the transverse plane. During the ensuing interval of time,  $TE/2$ , possible phase coherence will get lost between spins due to local field

inhomogeneities as described above and inherent T2 relaxation processes. The 180° degrees pulse then inverts the spins about the x or y axis so that after the next TE/2 at the center of the echo-readout, dephase due to field inhomogeneity will be refocused. Any decay in the magnitude for the net magnetization vector at the time of this echo is due to inherent spin-spin relaxation processes. During the second TE/2 time interval phase encoding gradients are applied to encode magnetization frequency in one or two dimensions, and an readout gradient is applied during the echo readout to encode the magnetization in the second or third dimension.

In multi-echo sequences more 180° pulses are applied following the excitation 90° pulse and echoes are acquired following each 180° pulse (Figure 2.2). The time intervals are given so that the dephase can be refocused and echoes can form. The time interval between 90° and the first 180° pulse is  $\tau$ , which is also half of the first echo time. The same interval is given between 180° and echo as well as between the echo and the next 180° pulse and so on. In Carr-Pucell-Meiboom-Gill (CPMG) multi-echo sequences (Figure 2.2), 90° RF pulse is applied along the x axis ( or y axis) and all 180° pulses are applied along the y axis (or x axis) to ensure all echoes will have same phase. In multi-echo sequences, there are two modes of imaging acquisitions: CPMG mode and Rapid Acquisition with Relaxation Enhancement (RARE) mode. In CPMG mode, same phase encoding steps are applied to each echo in the echo train, each echo is used for a distinct image with echo time of  $n \cdot (\text{echo-spacing})$ , and number of images equal to the number of echoes following each excitation are obtained at the end of imaging. In RARE mode, distinct phase encoding steps are applied to each echo, that is, each echo represents one line in K space, and one image is obtained with scanning time shortened by a factor equal to the number of echoes collected following each excitation. Therefore, RARE is a fast scanning technique.

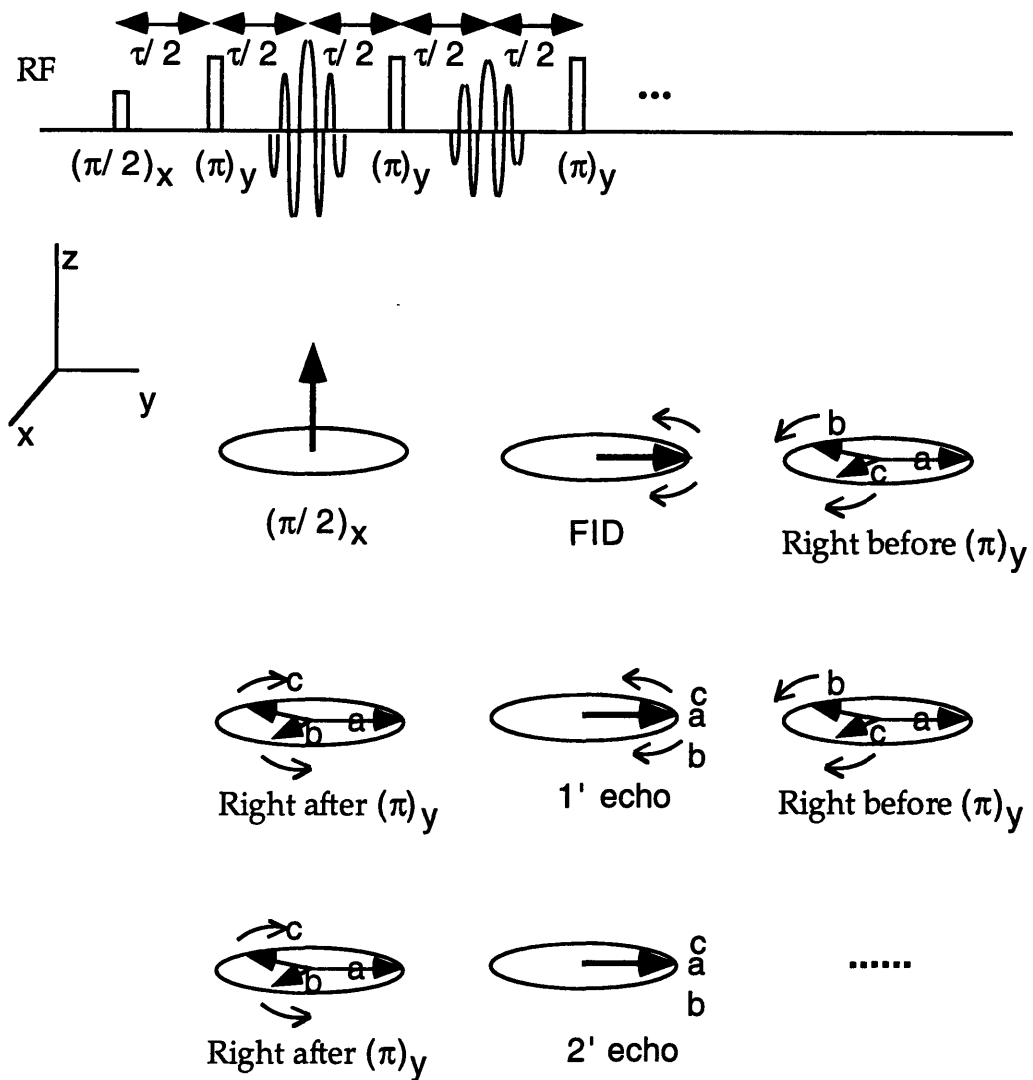


Figure 2.2 CPMG pulse sequence, a multi-echo sequences in which all  $180^\circ$  or  $(\pi/2)_x$  pulses in the train are phase shifted  $90^\circ$  with respect the initial  $90^\circ$  or  $(\pi/2)_y$  pulse. This sequence results in all echoes with same phase. CPMG sequence is particularly useful for determining the spin-spin interaction time  $T_2$ .

### **2.3 Spin-spin relaxation(T2) effect in RARE Image**

As echoes are generated following a spin excitation, there is a gradual loss of signal due to T2 decay processes. The T2 decay time is typically defined in terms of a decay of signal strength  $S$  with echo time TE, as described in Equation (2.8). In practice, T2 decay limits the amount of signal available from a given peak in successive echoes. The generation of spin-echoes beyond a given peak's T2 decay envelope leads to diminishing returns in signal-to-noise ratio. This feature determines an important practical consideration in performing RARE imaging studies: the number of usable echoes which can be acquired with the limitation imposed by the T2 decay time. This number depends upon the T2 decay time as well as the echo-spacing or how long a time period is used for acquiring each individual echo. The shorter the time required for each echo acquisition the more echoes can be acquired following excitation and the faster the RARE sequence. In our case, for PCr imaging, this feature is mainly limited by the hardware of our gradients, this will be discussed further in Chapter 5.1.

CPMG mode, in which a series of images with different echo time TE will be acquired, is suited for studying the tradeoffs between T2 decay and the total number of usable echoes acquired following each excitation and for determining the number of effective echoes which can be used in RARE mode to shorten imaging time. It tells the amount of signal which can be obtained at each echo-readout with T2 relaxation effect.

### **2.4 Suppression of unwanted resonance**

In many cases, signal from a specific molecule is desired, and signals from other molecules will cause degradation or contamination of the signal. To suppress unwanted signals, a commonly used technique is Chemical Selective Suppression

(CHESS). In CHESS, a chemical selective RF pulse, which has narrow bandwidth (in spectral domain) or long duration time ( in time domain), is followed by crusher gradients along three axes. The RF pulse selectively flips the unwanted magnetization into the transverse plane, crusher gradients dephase spins so that signals from spins are out of phase and cancel each other, thus total magnetization from that molecule in transverse plane is zero.

## 2.5 Determination of the spectral width of the RF pulse

Chemical selective RF pulse, which selectively flips one of the resonances without affecting the others in the spectrum, usually requires narrow spectral width or long pulse length. The length of the RF pulse is dependent on the chemical shift difference between the selected resonance to its neighboring resonances. PCr is next to Pi with a chemical shift difference of about 400 Hz on a 4.7 T magnet. To effectively remove Pi resonance which has full-width-of-half-maximum(FWHM) usually less than 250 Hz, requires that the RF pulse have about 125 HZ FWHM spectral width on Pi resonance. In the case of using a Gaussian shaped pulse, the duration time can be found as follows.

On our system, the Gaussian pulse duration time refers to the time interval between the two points at which pulse intensity drops to 0.01 of its peak intensity. Defining the Gaussian pulse as:

$$\exp(-t^2 \alpha^2); \quad (2.16)$$

and pulse length  $\tau$ , there is

$$\exp(-(\frac{\tau}{2})^2 \alpha^2); \quad (2.17)$$

thus :

$$\alpha\tau = 4.29 \quad (2.18)$$

The Fourier Transform of the Gaussian shaped pulse is:

$$\exp(-\omega^2 / 4\alpha^2) = \exp(-(2\pi f)^2 / 4\alpha^2) \quad (2.19)$$

since at FWHM, there is:

$$\exp(-2\pi(\frac{FWHM}{2})^2 / 4\alpha^2) = \frac{1}{2}; \quad (2.20)$$

and

$$FWHM = 0.53\alpha; \quad (2.21)$$

limiting the FWHM to 250 HZ, combining Eq. 2.18 and 2.21,  $\tau$  can be found as about 9 ms.

Similarly, the spectral width of all shaped pulses can be calculated. For example, 1 ms long Gaussian shaped pulse has a spectral width of about 2.3 KHz.

## Chapter 3

### Experimental material and method

In this chapter, the experiment instrumentation apparatus, setup, imaging pulse sequence and data processing are described.

#### 3.1 Instrumentation

All Experiments were performed on a 4.7 T, 30 cm horizontal bore Bruker BIOSPEC NMR system (Bruker Instruments, Billerica, MA). An Alderman-Grant coil (volume coil), 14 cm in diameter, 8 cm long, was made and used for both transmission and reception in human forearm muscle study.

The configuration of the Alderman-Grant Coil is described in Figure 3.1 (Alderman, Grant, 1979). It consists of two vertical bands with wings on both sides (top and bottom), two guard rings on the top and bottom, and capacitors between extremities of the wings on the two sides of the vertical band. There is a layer of 2 mm Teflon dielectric between the guard rings and the wing-band pieces. A total of four groups of capacitors were placed between the wings. Part of the resonating capacity is generated by the proximity of the “wings” of the vertical bands to the “guard rings.” The additional capacity necessary to resonate the structure at 81 MHz, the <sup>31</sup>P resonance frequency, was determined empirically and then added by soldering capacitors between the extremities of the wings. Capacitors are evenly placed in the four groups of capacitors between the extremities to optimize the RF field homogeneity inside the coil. The guard rings shield the sample from the electric fields generated by the RF voltage present between the wings. The advantage of this coil is simple structure, versatile resonance frequency and low heat dissipation. To optimize the static main magnetic field homogeneity

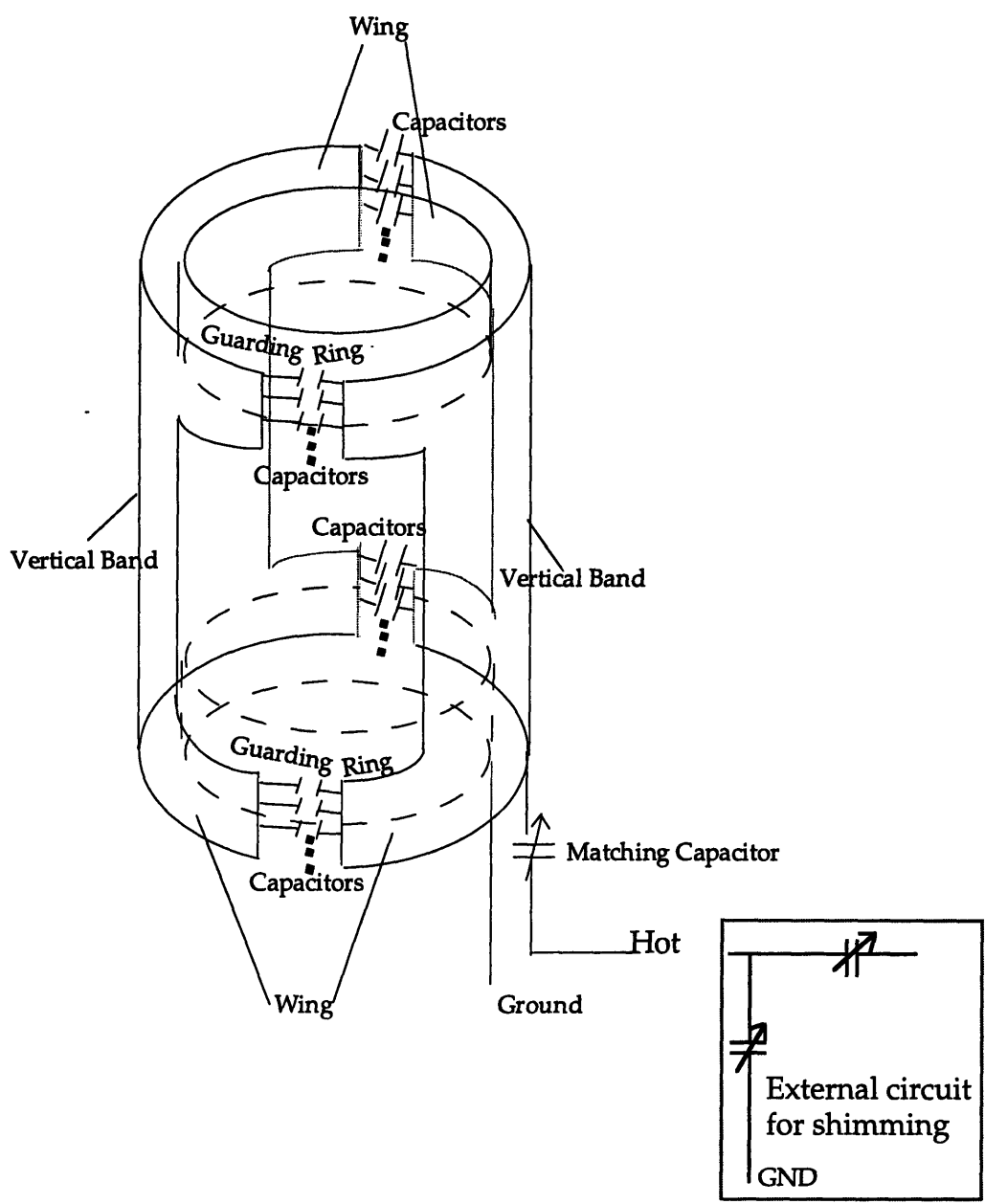


Figure 3.1 Alderman-Grant coil. It consists of two vertical band with wings on both sides, two guarding rings and capacitors between the wings. There is a layer of 2 mm Teflon dielectric between the guard rings and the wing-band pieces. An external was connected to the coil for tuning the coil to proton resonance frequency during shimming.

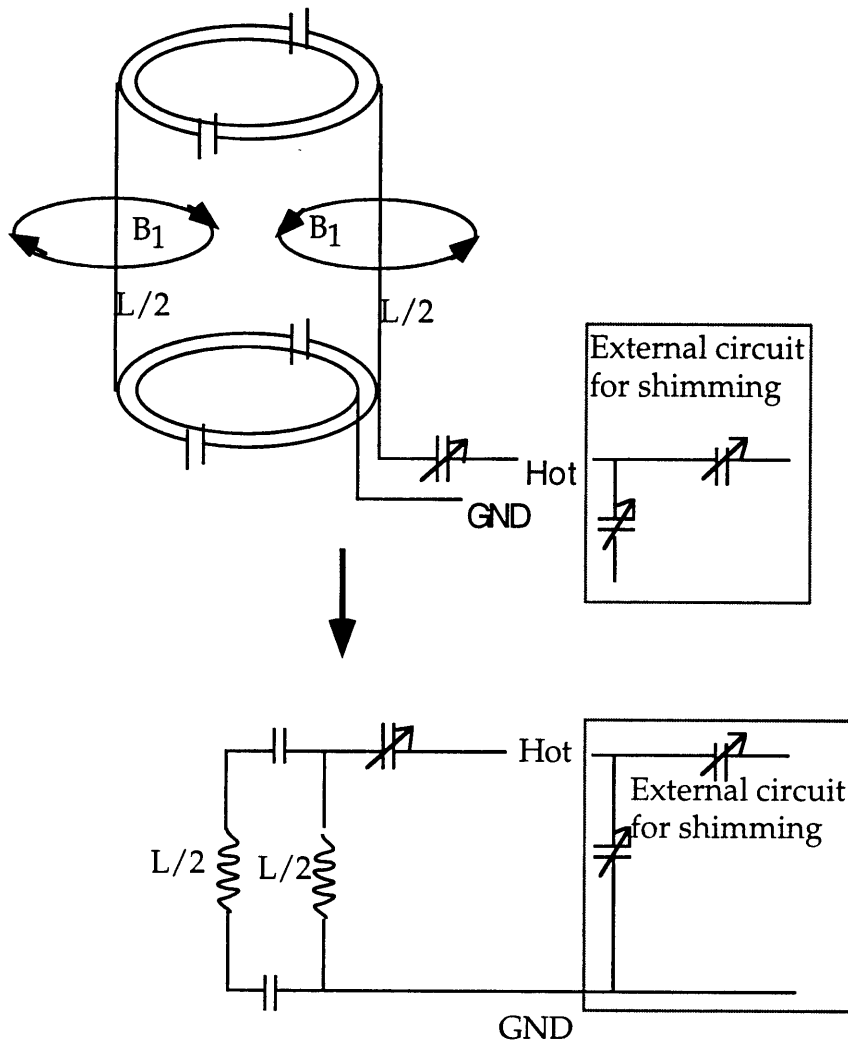


Figure 3.2. The mechanism of the Alderman-Grant Coil: A LC circuit analogous to the coil.

throughout the sample, an external circuit made of two variable capacitors is connected to the coil for tuning one of the resonant frequencies to proton during shimming. The mechanism of the coil and external circuit can be explained as in Figure 3.2.

### 3.2 Pulse sequence

Two types of spectral pulse sequences, one pulse (Figure 3.3a) and spin-echo(SE) (Figure 3.3b) are used for spectral acquisition; two modes of multi-echo mode sequences, CPMG and RARE are used for images acquisitions (Figure 3.4).

The one pulse sequence consists of a 1 ms Gaussian shaped pulse followed by a 5.12 ms readout with a sweep-width of 5 KHz. SE spectra with a sweep-width of 5 KHz, TE of 12 ms and an echo-readout starting at the center of the spin echo were recorded with Pi suppression. Pi suppressions were performed with CHES sequence repeated three times. The CHES sequence consisted of a 10 ms Gaussian pulse which has FWHM around 250 Hz (See previous chapter) at the Pi resonance followed by dephasing gradients along all three axes.

Multi-echo sequences are used for PCr imaging in which a 4 cm thick section-selective  $90^\circ$  PCr excitation RF pulse, 1 ms long, Gaussian shaped, was followed by non-selective refocusing  $180^\circ$  pulses. The amplitude  $90^\circ$  and  $180^\circ$  pulse were calibrated by minimizing FID components and maximizing echo signals during a CPMG echo train applied in the absence of gradients. A 2 ms phase encoding gradient lobe was applied prior to each readout and "unwound" afterwards. Thirty-two echo signals were collected following each excitation. In CPMG acquisition phase encoding gradient amplitudes were incremented from excitation-to-excitation. For each excitation one line in a series of thirty-two K space matrices were filled and a series of thirty-two images with TE equal to  $n \cdot (\text{echo-spacing})$ ,

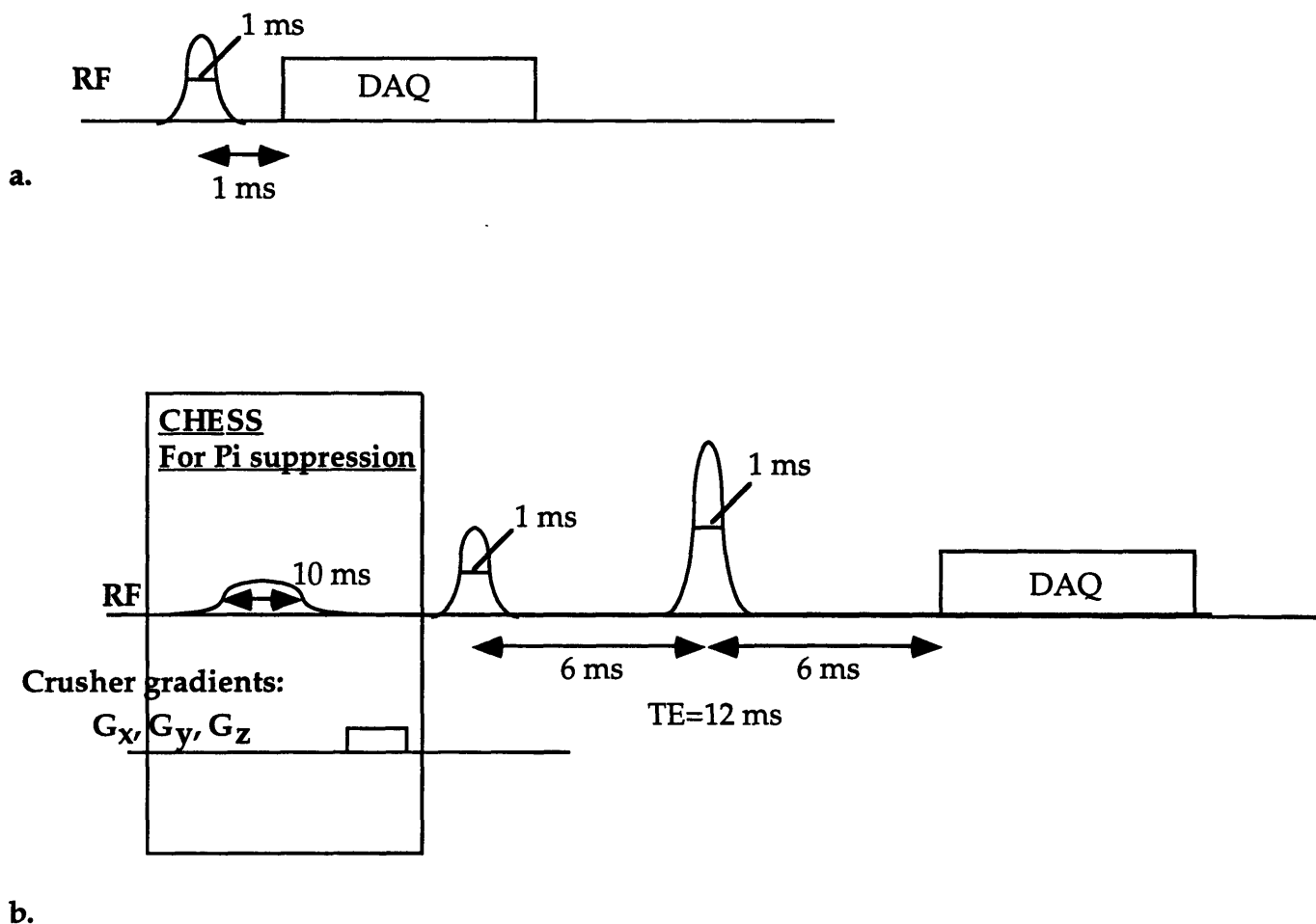


Figure 3.3 Pulse sequences used in acquiring spectra. a. In one pulse sequence, all  $^{31}\text{P}$  signals are recorded including Pi and PCr. b. In spin echo (SE) sequence, signals from Pi are selectively suppressed. SE spectral acquisition is important in determining the gain for the saturation RF pulse in order to precisely flip the Pi to the transverse plane. To avoid the imperfection of the  $90^\circ$  pulse, the CHES pulse was repeated three times.

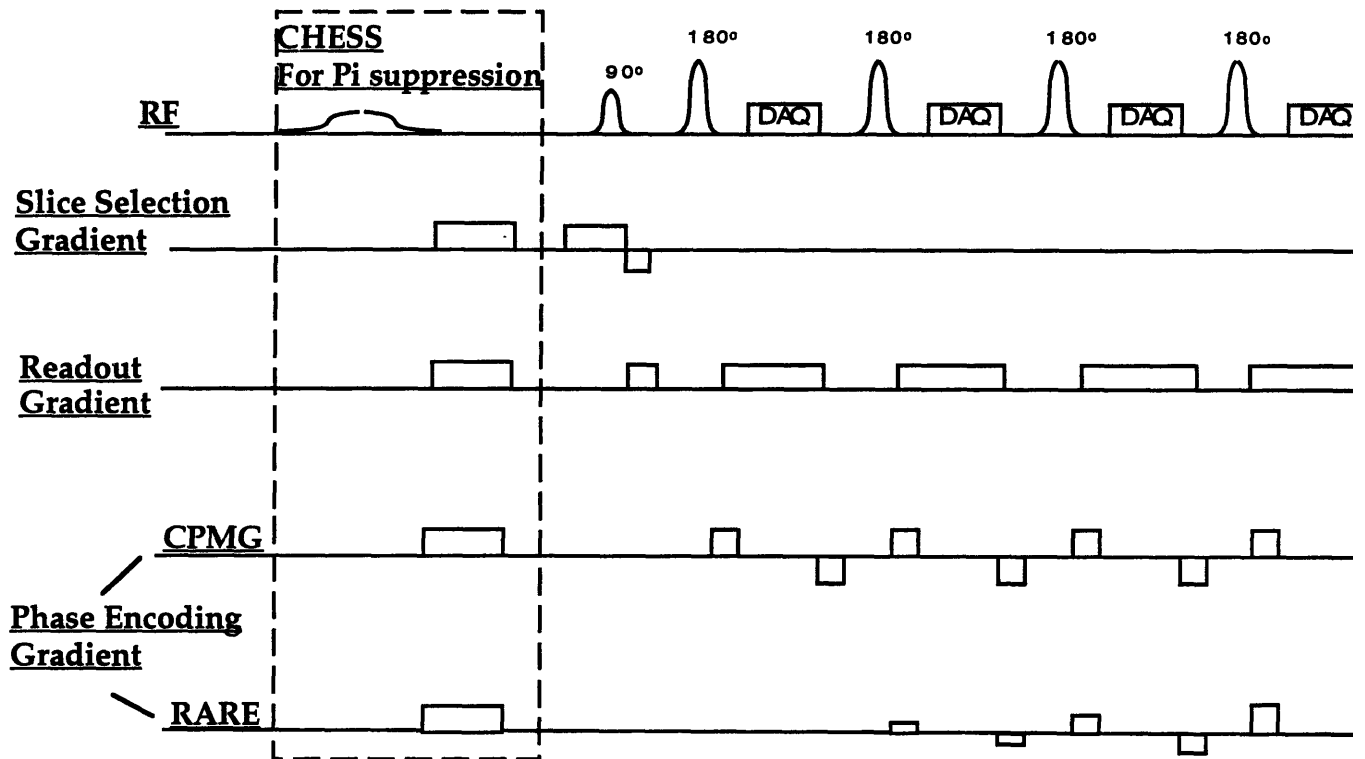


Figure 3.4 Multi-echo sequences used for PCr imaging. Section-selective gradient is applied to selectively excite a 4 cm section. Pi suppression is applied by using CHES pulse as in Fig. 3.3. A 2 ms phase encoding gradient is applied prior to each readout and "unwound" afterwards. a. In CPMG mode acquisition phase encoding gradients are incremented from excitation-to-excitation. This mode is important to determine the optimal number of echoes to be used in the RARE mode. b. In RARE mode acquisition, phase encoding gradients are incremented from echo-to-echo. Thus imaging time is shortened by a factor equal to the number of echoes collected following each excitation.

(where  $n=1, 2 \dots, 32$ ) were generated after the filling of all the K spaces. In the RARE acquisition, phase encoding gradient amplitudes incremented from echo-to-echo. For each excitation, thirty-two lines in one k-space are filled. Thus the scan times in the RARE mode were shortened by a factor of thirty-two, compared with the traditional imaging technique. A centric phase encoding reordering scheme was employed in which the lower phase encoding gradients were applied to early echoes and the larger phase encoding gradients to later echoes. The RARE images were also implemented with Pi suppression using the CHES sequence.

All images were acquired with 12 ms echo spacing, 3 ms echo readout, 5 s time-of-repetition (TR) and 32 X 32 matrix size.

### **3.3 Phantom experiment for technique testing**

A phantom study was used for testing the effectiveness of Pi suppression in the RARE imaging and for simulating the in vivo studies.

The PCr/Pi phantom consists of two rectangular shaped bottles containing approximately 30 ml of 150 mM PCr solution and 100 mM Pi solution respectively. The phantom was placed at the center of Alderman-Grant coil. Both one-pulse and SE spectra of the phantom were recorded with a 10 s TR, 5 KHz spectral width and two signal averages. NiSO<sub>4</sub> (shortening T<sub>2</sub>) were used to modify the T<sub>2</sub> value of the phantom so that it had T<sub>2</sub> values similar to those reported in vivo T<sub>2</sub> values for PCr. About 0.2 mg of NiSO<sub>4</sub> was added to 30 ml PCr solution to obtain a T<sub>2</sub> value of 420 ms and 0.5 mg of NiSO<sub>4</sub> was added to 30 ml Pi solution to obtain a T<sub>2</sub> value of 180 ms. A CPMG mode multi-echo imaging sequence was applied to acquire the T<sub>2</sub> values of the sample and to determine the number of echoes that can be used following the excitation in RARE mode imaging. A CPMG mode sequence was applied to record a series of thirty-two phantom images with TEs of  $n * 12$  ms.

Fitting of the signal intensities in the images vs. the echo time with a mono-exponential function of  $\exp(-n \cdot \text{echo-spacing}/T_2)$  yields the spin-spin relaxation time  $T_2$  of the sample. In centric phase encoding mode,  $T_2$  effect behaves as a low pass filter. The RARE images with and without  $\text{Pi}$  suppression were acquired with 16 cm X 16 cm Field-of -View (FOV) and four signal averages.

### **3.4 Experimental setup and protocol for human forearm study**

Human study includes four parts: the acquisition of spectra before and after exercise; acquisition of CPMG echoes; regional PCr change during the exercise; and the PCr recovery rate after exercise.

#### **3.4.1 The spectra acquisition before and after exercise**

The right forearm of healthy volunteers (N=6) were inserted into the Alderman-Grant coil with the 4 cm slice located approximately 3 cm distal to the elbow. Spectra were acquired using a one-pulse and a SE sequence with  $\text{Pi}$  suppression. All spectra were acquired with 5s TR and 16 signal averages. Spectra were recorded to observe the total  $\text{Pi}$  and PCr level change before and after exercise. Spectra were obtained at rest.

Exercise, which consisted of finger flexion, were performed for 5 minutes outside the magnet and continued during the second acquisition of spectra. Because signal came from the whole arm, motion induced problems should be minimal and were not considered during the spectral acquisition.

#### **3.4.2 CPMG Acquisition**

A series of thirty-two CPMG echoes were acquired at rest with zero phase encoding step using 5s TR and 64 signal average. Fourier Transform was performed to obtain the image profile along the frequency encoding direction. CPMG echoes

were acquired to determine the optimal number of echoes that should be used in the RARE imaging.

### **3.4.3 Regional PCr change during/after exercise and comparison with T2-weighted proton images**

Images were acquired using the RARE sequence with Pi suppression. All images were acquired using 5 s TR, 22 cm field-of-view, 32 X 32 matrix size and 64 signal averages, with a total scan time of 5 minutes and 30 seconds.

This study was aimed to observe the correlation of the involvement of muscle groups in exercise and the regional PCr drops and to exam the result with known physiology. The results were compared with T2 weighted proton images under the same physiological conditions. PCr images were obtained at rest. Vigorous exercise, consisting of the flexion of the fourth and fifth fingers, was performed outside the magnet for 10 minutes. Arms were then placed back in the magnet at the same position; another PCr image was immediately acquired. Exercise was continued during this time, but occurred only between scans during the TR waiting period. Gradient onset sound was used for timing. A similar experiment was performed with exercise consisting of the flexion of three fingers: the third, the fourth and the fifth fingers. PCr images were also recorded at rest and during/after exercises.

Proton images are acquired with effective echo time of 80 ms under exactly the same physiological conditions used in the PCr imaging.

In the above study no attempts were made to standardize the work load of the exercises.

### **3.4.4 PCr recovery rate after exercise**

This study is aimed to observe regional PCr changes in the time course of rest, exercise and recovery. These change partially indicate the metabolic status. Images were first acquired at rest. Exercise was performed inside the magnet. Exercise, consisting of flexion of fingers without restriction in the use of the fingers, was measured at 3 pounds per square inch for every 1 to 2 seconds, initiated after the start of the second imaging acquisition, and timed between TR periods during waiting time. A final three PCr images were acquired immediately following exercise cessation to observe PCr recovery.

To compare the PCr level during these three periods of time, average signal intensities from a region with size of four pixels are chosen in the plots, and error bar indicates the standard deviation among the four pixels.

## Chapter 4

### Results:

Both spectra and PCr images from the phantom experiment, the human forearm muscle are shown here.

#### 4.1 Phantom experiment

One pulse and SE spectrum of the phantom are shown in Figure 4.1. Both PCr and Pi peaks are clearly seen in one-pulse spectrum (Figure 4.1a). In the SE spectrum (Figure 4.1b), the Pi resonance is eliminated using Pi suppression and the PCr peak is intact.

A series of images of the phantom, acquired at TE of  $n \cdot 12$  ms using CPMG mode of multi-echo sequence, are shown in Figure 4.2. A gradual signal drop due to T2 decay can be seen in these images. A T2 value of 400 ms for PCr and 150 ms for Pi were found after fitting the signal intensities of the images versus echo time with a monoexponential decay function. The RARE image of Pi/PCr phantom are shown in Figure 4.3a without Pi suppression and in Figure 4.3b with Pi suppression. Both PCr and Pi are shown in Figure 4.3a, and Pi was effectively removed in Figure 4.3b.

#### 4.2 Human forearm muscle studies

The results from human forearm studies: the acquisition of spectra before and after exercises, acquisition of CPMG echoes, regional PCr change during the exercise, and the PCr recovery rate after exercise are presented.

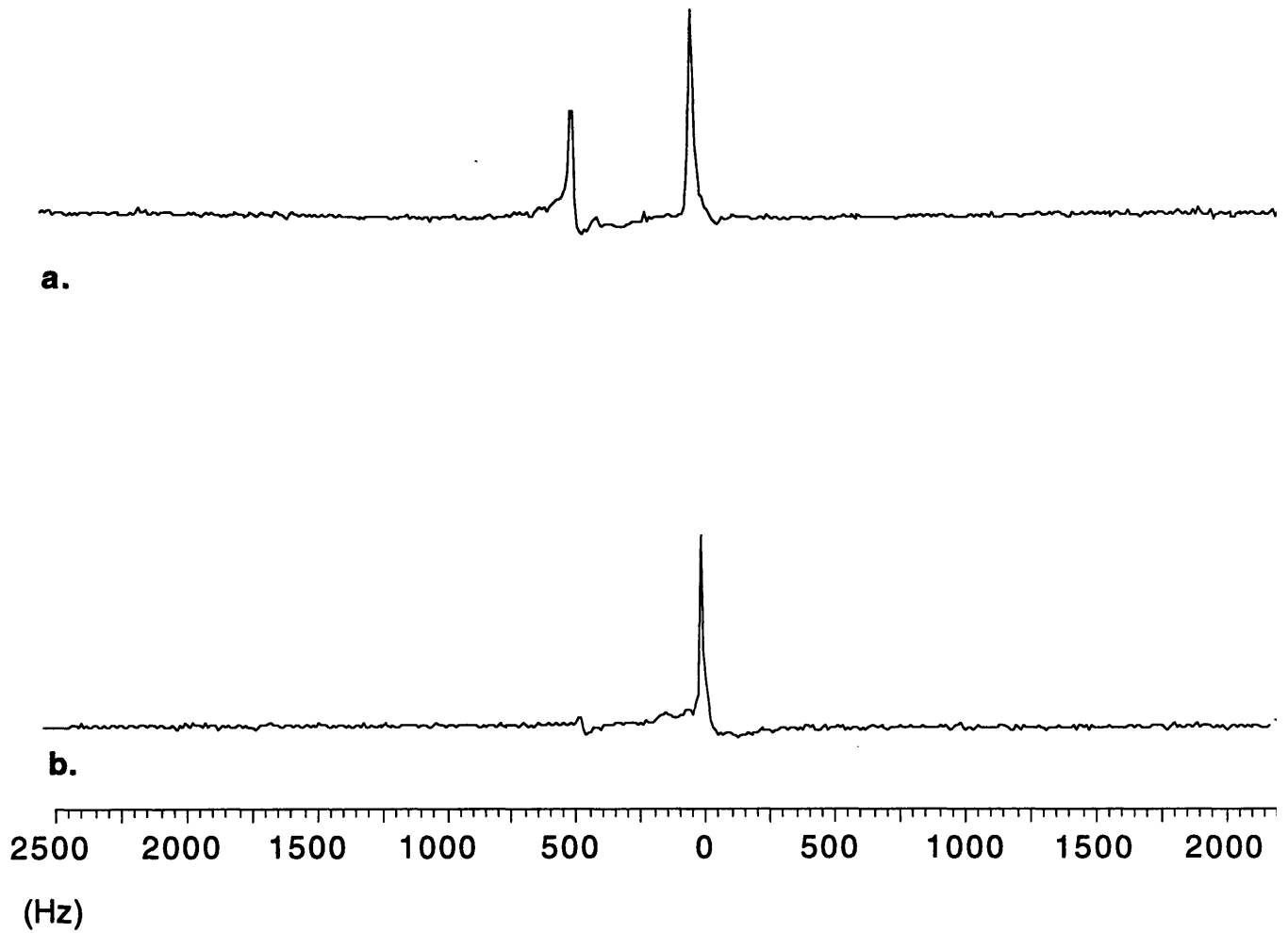


Figure 4.1. One-pulse and spin-echo spectra of the Pi/PCr phantom. Both were acquired with 5Hz spectral width and 10 s TR. a. one-pulse spectrum: both Pi and PCr resonances are well depicted. b. in spin-echo spectrum: using CHES, Pi resonance is effectively removed. Spectrum acquired with TE of 12 ms.

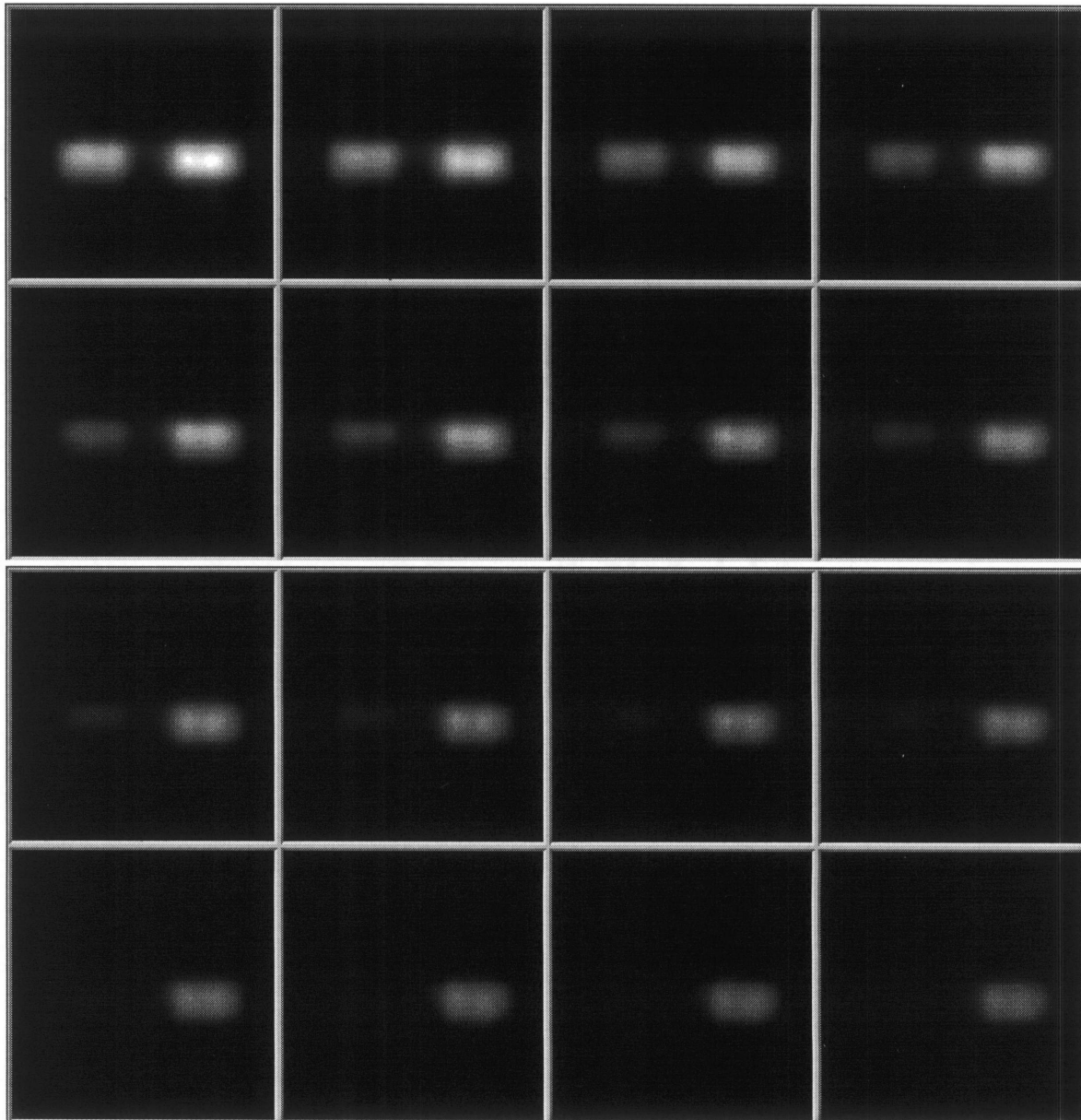


Figure 4.2 A series of 32 CPMG images. Shown here are every other images in the series. A gradual signal intensity decay can be observed due to the T2 relaxation. A monoexponential function was used to determine T2, NiSO<sub>4</sub> was used to modify the T2 of PCr to about 400 ms.

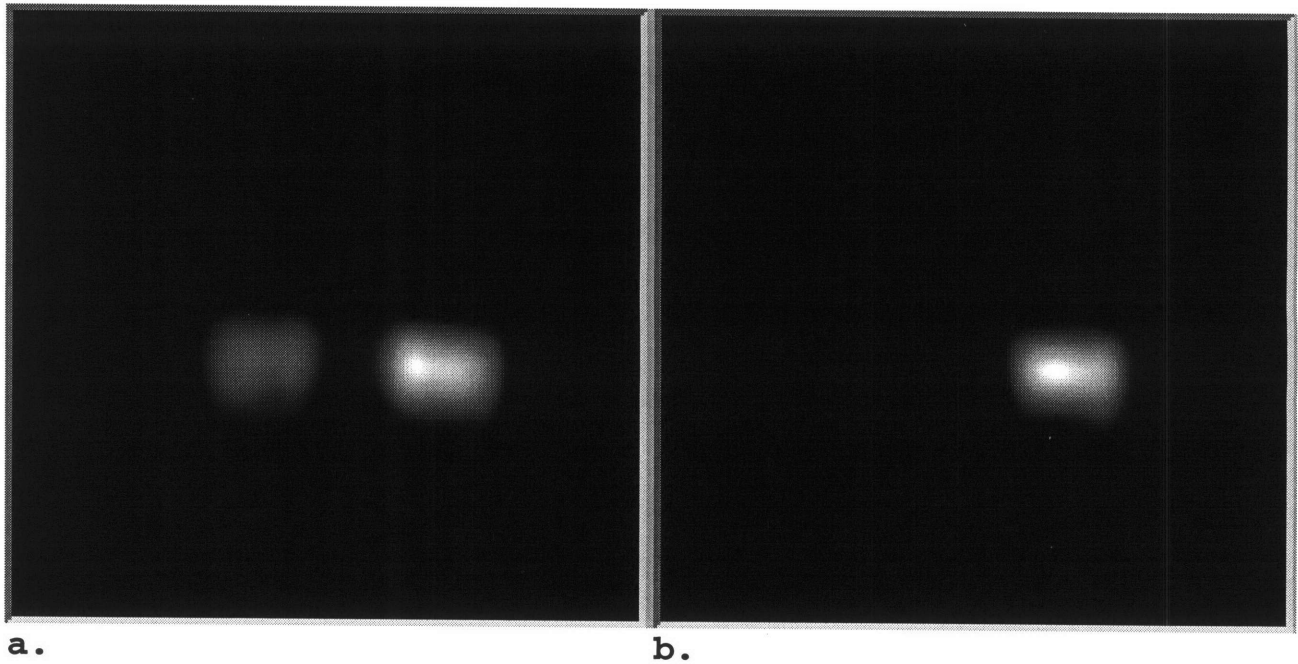


Figure 4.3 The RARE image of the Pi/PCr phantom. Thirty-two echoes were collected following each excitation, thus imaging time is shortened by a factor of 32. a. A RARE image recorded without Pi suppression. Both Pi and PCr phantom are well shown in the image. b. A RARE image recorded with Pi suppression. Pi phantom is effectively removed. All images are acquired with 12 ms TE, 10 s TR and 2 signal average.

#### 4.2.1 The spectra acquired before and after exercise

The spectra of the human forearm at rest are shown in Figure 4.4a, using one-pulse sequence, and in Figure 4.4b, using spin-echo sequence with Pi suppression. In general, at rest large PCr resonance can be observed with minimal Pi. ATP resonances are weak, which could be due to a much lower ATP concentration compared to PCr concentration and the limited RF-pulse spectral width used in the pulse sequence. The spectra obtained during/after exercise are shown in Figure 4.4c using one-pulse and in Figure 4.4d using spin-echo sequences. Notice the increased Pi resonance and decreased PCr resonance in Fig. 4.4c. In Fig 4.5d, Pi resonance is removed using spin-echo sequence with Pi suppression; PCr drop can be observed.

#### 4.2.2 CPMG acquisition

A series of Fourier-transformed CPMG echoes are shown in Figure 4.5 which represent the image profiles along the frequency encoding direction obtained at TE of  $n \cdot 12$  ms ( $n=1, 2, \dots, 32$ ). A monoexponential decay of the signal intensity is seen. A global T2 value of 360 ms of the forearm muscle is yielded after fitting the peak-height signal intensity versus TE with a monoexponential function (Figure 4.6).

#### 4.2.3 Regional PCr change during/after exercise and the comparison with T2-weighted proton images

Shown in Figure 4.7 a-f are PCr RARE images and T2 weighted proton images obtained at rest and 10 minutes after the flexion of the fourth and the fifth fingers. Shown in Figure 4.7a is a RARE PCr image and in Figure 4.7b is a T2 weighted proton image of the forearm at rest. Two bony structures (radius and ulna) can be seen as low intensity areas in PCr images due to low PCr concentration

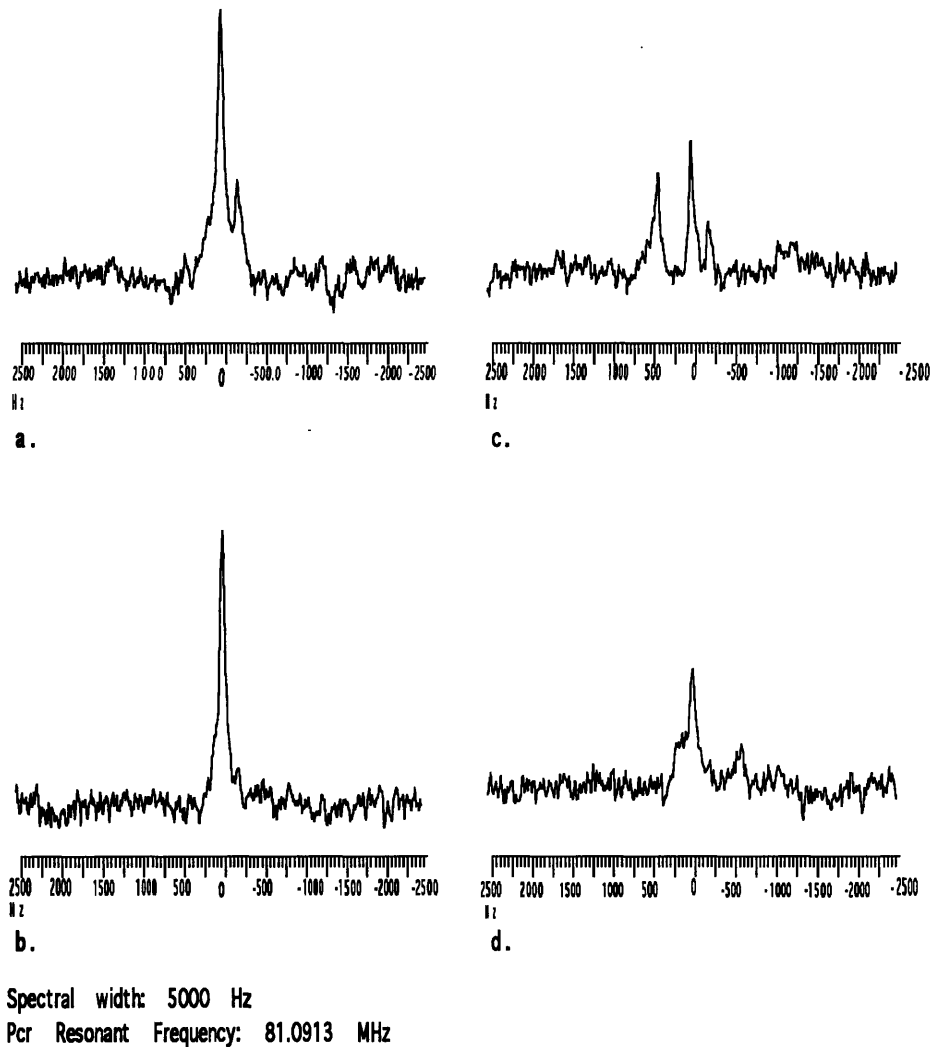


Figure 4.4 One-pulse and spin echo spectra of human forearm acquired before and after exercise. On the top, a. and b., are one-pulse spectra; on the bottom, c. and d., are spin-echo spectra. a. At rest, on one-pulse spectrum, large amount of PCr can be observed with minimal amount of Pi. b. after exercise, on spin-echo spectrum, PCr decreases, Pi increases, probably to the same amount. c. at rest, spin-echo spectrum, large amount of PCr can be observed. d. after exercise, PCr decreases, Pi resonance is effectively removed with CHESS. In those spectra, ATP resonances, especially  $\alpha$ -ATP and  $\beta$ -ATP, are not well observed, which could be due to the relatively small amount of ATP in muscle compared to PCr and limited bandwidth of the 1 ms Gaussian pulse.

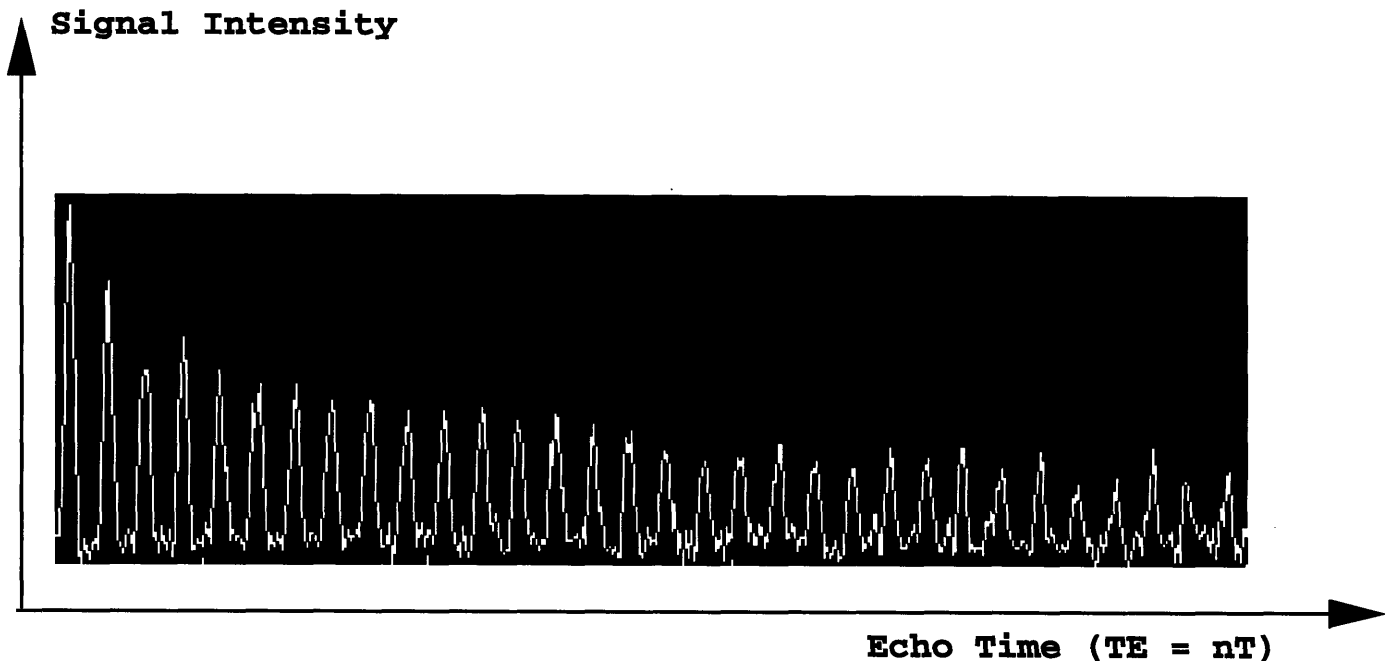


Figure 4.5 The FT of a series of 32 CPMG echo train acquired at zero phase encoding gradients, thus they represent the image profiles along the frequency encoding direction. This CPMG echo train was used to see how much signal can be acquired at each echo time and to determine the optimal number of echoes to be used for the RARE mode. Here we can see that even at the third-second echo, reasonable amount of signal can be collected. This led us to use 32 echoes in the later RARE mode forearm imaging. Because of centric phase encoding used in RARE mode, this decay envelope also provides a view of low pass filtering effect in the RARE mode imaging due to T2 relaxation.

## T2 relaxation effects on signal amplitude observed in CPMG echo train

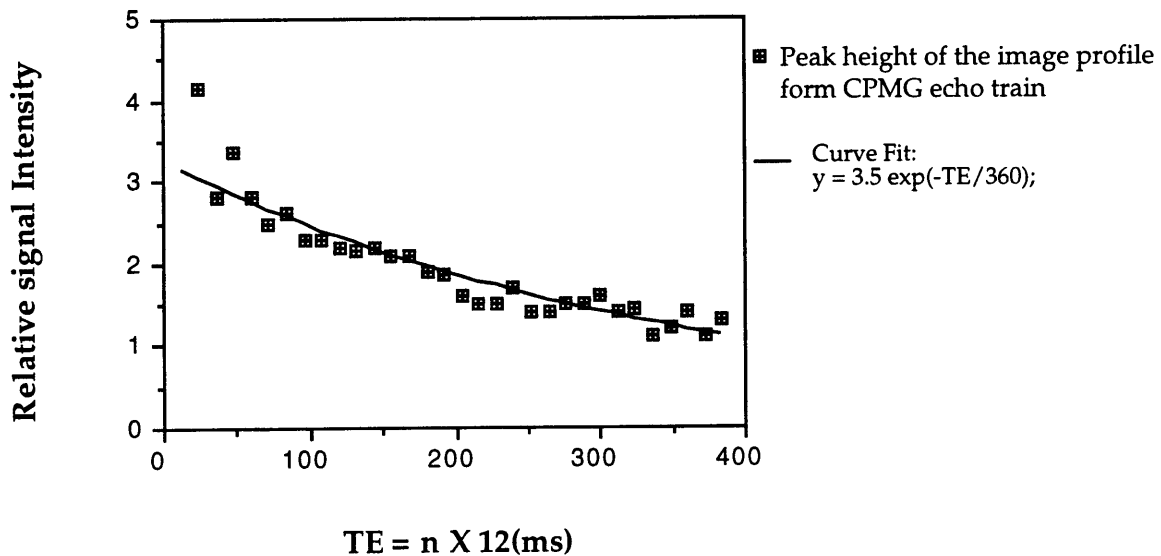


Figure 4.6 A global T2 value of 360 ms is found for the forearm muscle after fitting the CPMG echoes peak-height vs. echo time with a monoexponential function. Errors are found for the early echoes which could be due to T1 relaxation effect as 5 s TR used in the experiment is close to T1, a short T2 component in PCr or/and imperfect RF pulse flip angles .

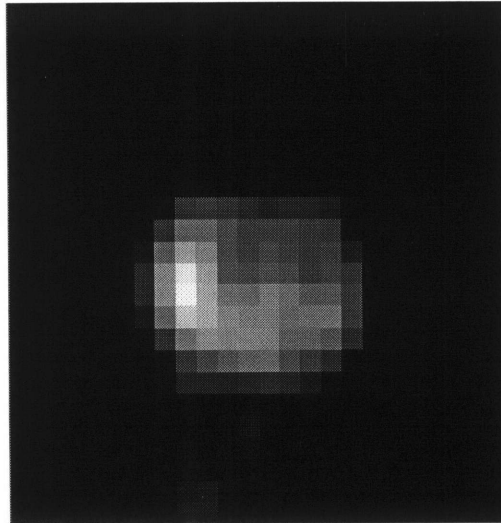
in bone, and can be seen as two low signal intensity areas with high signal intensities inside as bone marrow in proton images. The bony structure can be used as landmarks to orient PCr images and proton images to identify different muscle groups. After ten minutes of contraction, another RARE PCr image and proton image are acquired as shown in Figure 4.7c and Figure 4.7b, respectively. Notice pre-exercise gives higher signal intensity in PCr images and generally lower muscle signal intensity in the proton image. In the post-exercise images, a regional signal intensity drop in PCr image and a regional signal intensity increase in T2-weighted proton image can be seen at similar locations. The images that gives the signal intensity difference before and after exercises are indicated in Figure 4.7e for PCr images, and Figure 4.7f for proton weighted images, respectively. Compare with standard anatomy atlas flexor digitorum profundus (FDS) can be identified as the muscle mainly involved in the exercises.

Shown in Figure 4.8 are another set of images acquired before and after the 10 minute flexion of the third, the fourth and the fifth fingers. Similarly, high signal intensity in PCr images (Figure 4.8 a) and low signal intensity in proton images as shown (Figure 4.8 b) at rest. Bony structures were used to orient images. After ten minutes of flexion, PCr images and proton images are acquired as shown in Figure 4.8 c and Figure 4.8 d. Signal intensity changes: drops in PCr image (Figure 4.8c) and increases in proton signal (Figure 4.8 d), in a larger region can be observed, which suggests that more groups of muscle were involved in this exercise than the previous one. The difference of the images before and after exercises are given in Figure 4.8 e for PCr images, and Figure 4.8 f for proton weighted images. The images that give the signal intensity difference before and after exercises are given in Figure 4.8e for PCr images, and Figure 4.8f for proton weighted images, respectively. By comparing

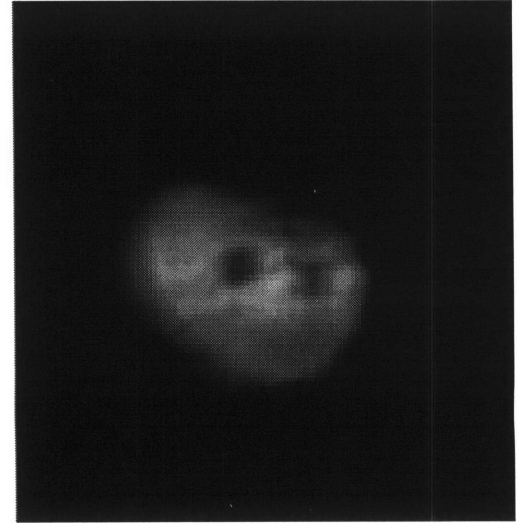
**RARE PCr Images:**

**T2 Weighted Porotn Images:**

**Rest:**

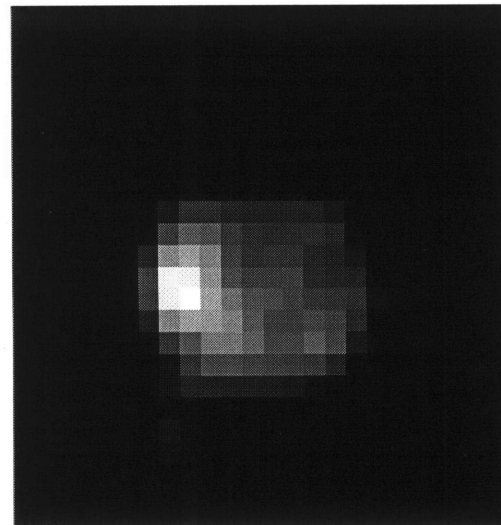


**a.**

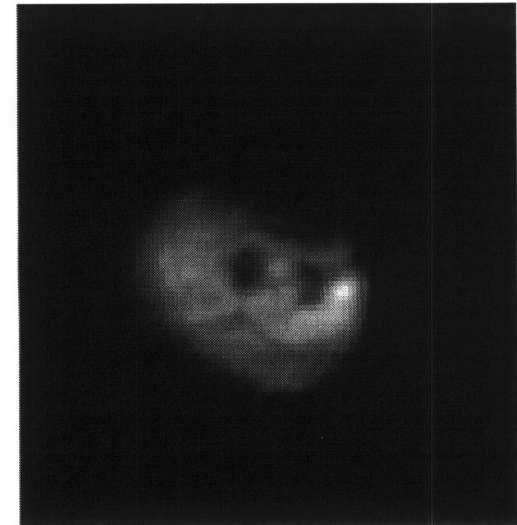


**b.**

**Exercise:**

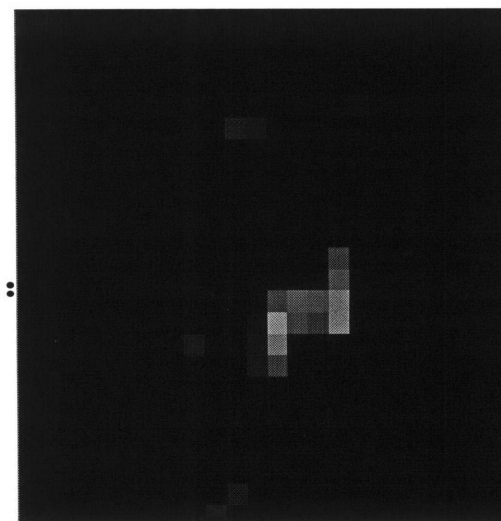


**c.**

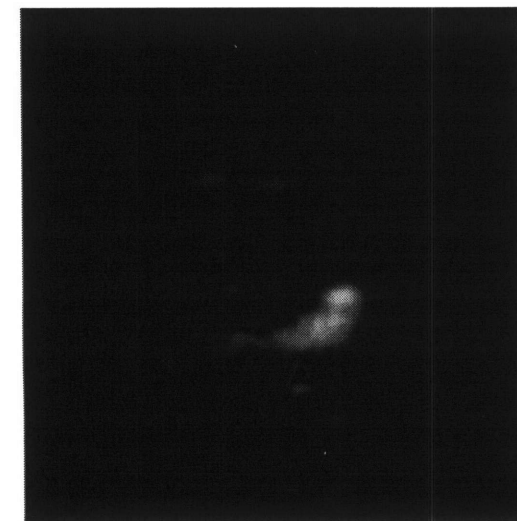


**d.**

**Difference:**



**e.**



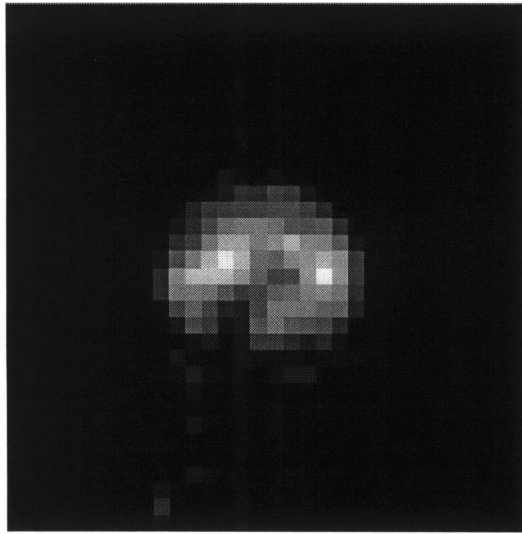
**f.**

Figure 4.7 (previous page) PCr distributions of the forearm (left column) before and after the flexion of the fourth and the fifth fingers using the RARE imaging approach, PCr images are compared with T2 weighted proton images before after the same exercise. Bony structures i.e. Radius and Ulna seen as two low signal areas in both types of images are used to align the images. Effective TE of 80 ms are used for the proton image acquisition. a. PCr image b. T2-weighted proton image acquired at rest. High signal PCr levels and low T2 values are seen in the resting muscle. c. PCr image d. T2 weighted proton image acquired after 10 minutes of finger flexion. In the similar area below the radius, decreased signal intensity in PCr image and increased signal intensity in proton images are observed. e. the subtraction PCr image f. the subtraction T2 weighted image before and after exercise. Good agreements are found in the two types of images. The signal change occurred in the flexor digitorum profundus (FDP) which is consistent with the physiological study. PCr images were acquired with 12 ms echo spacing, 5 s TR and 64 signal averages.

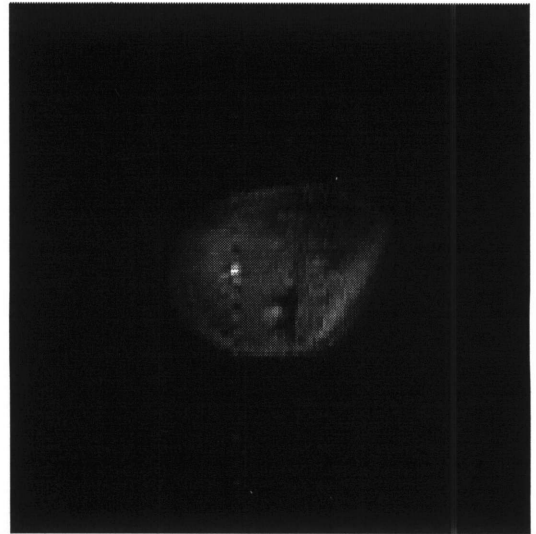
**RARE PCr Images:**

**T2 weighted Proton Images:**

**Rest:**

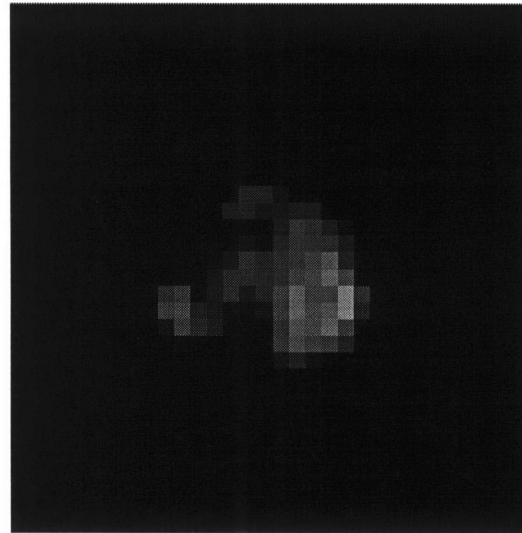


**a.**



**b.**

**Exercise:**

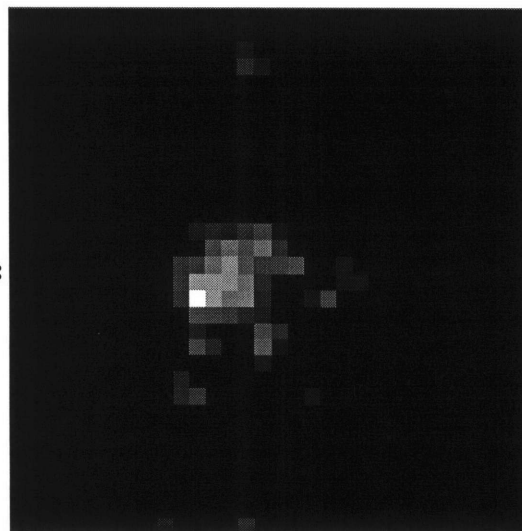


**c.**

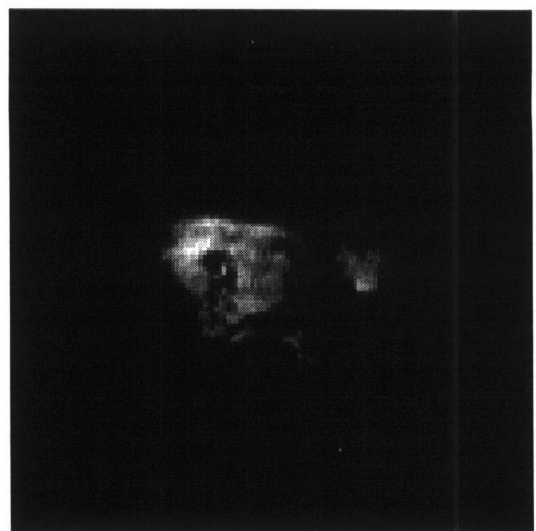


**d.**

**Difference:**



**e.**



**f.**

Figure 4.8 (previous page) Similar as Figure 4.7 however this time three fingers are used in the exercise. PCr distributions of the forearm (left column) before and after the flexion of the third, the fourth and the fifth fingers are compared with T2 weighted proton images before and after the same exercise. Bony structures are used to align these two types of images. Effective TE of 80 ms was used for the proton image acquisition. a. PCr image b. T2-weighted proton image acquired at rest. High signal PCr levels and low T2 value are seen in the resting muscle. c. PCr image d. T2 weighted proton image acquired after 10 minutes of finger flexion. In a similar area, larger than seen in Fig. 4.7, decreased signal intensity in PCr image and increased signal intensity in proton images are observed. e. the subtraction PCr image f. the subtraction T2 weighted image before and after exercise. Good agreements are found in the two types of image. The signal change areas are identified as two muscle group flexor digitorum profundus (FDP) and flexor digitorum superficialis(FDS) which is directly related to the third finger. The results are consistent with the physiological study. PCr images were acquired with 12 ms echo spacing, 5 s TR and 64 signal averages.

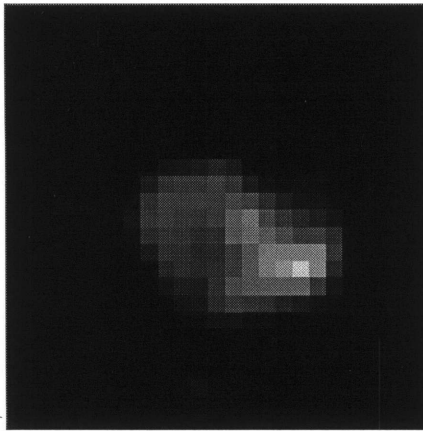
Figure 4.8e with Fig 4.8a, flexor digitorum profundus (FDP) and flexor digitorum superficialis (FDS) can be identified as the muscles involved in the exercises.

#### **4.2.4 PCr recovery rate after exercise**

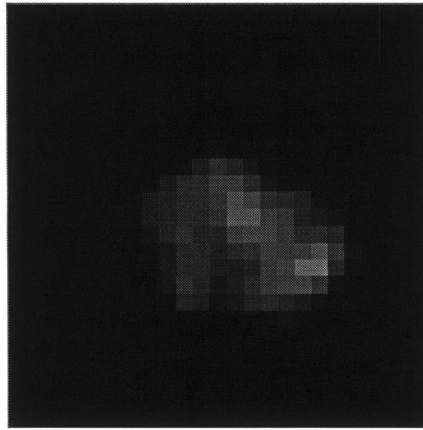
Shown in Figure 4.9 are images obtained at rest, during exercise and the recovery period. A PCr image of a forearm under resting condition is shown in Figure 4.9b. By comparing with Figure 4.9a, the radial and ulnar bones and the different muscle groups can be identified. The image acquired during exercise is shown in Figure 4.9c. Large decreases in PCr were observed in the Flexor digitorum profundus (FDP), superficialis (FDS) and flexor pollicis (FPL) longus area. Shown in Figure 4.9 d, 4.9f are the images obtained during recovery period immediately following exercise. Nearly complete PCr recovery was observed.

The FDP and FDS are the two muscles involved most in the finger flexion, PCr intensities versus time from these two regions are plotted in Figure 4.10 for the eight volunteers. PCr drop and recovery were observed in all the volunteers but varied markedly in the two regions.

**Rest**



**Exercise**



**Recovery**

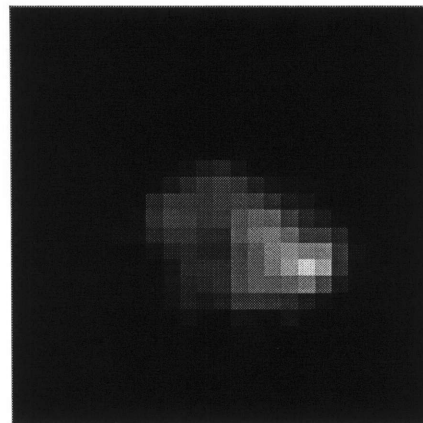
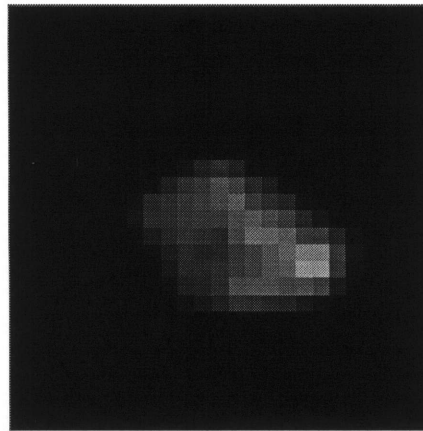


Figure 4.9 (in the previous page) The PCr recovery after muscle contraction.

Imaging are acquired as following:

Rest-----> exercise----> Recovery .....  
1' image-> 2' image---->3' images.....

no time interval was applied between image acquisitions. Exercise started immediately after the first image acquisition with contractions only between scans during TR waiting period of the second image acquisition. The third image initiated after the second image acquisition after the exercise stopped. For this volunteer, most PCr was recovered in the first image after exercise ( or the 3' image).

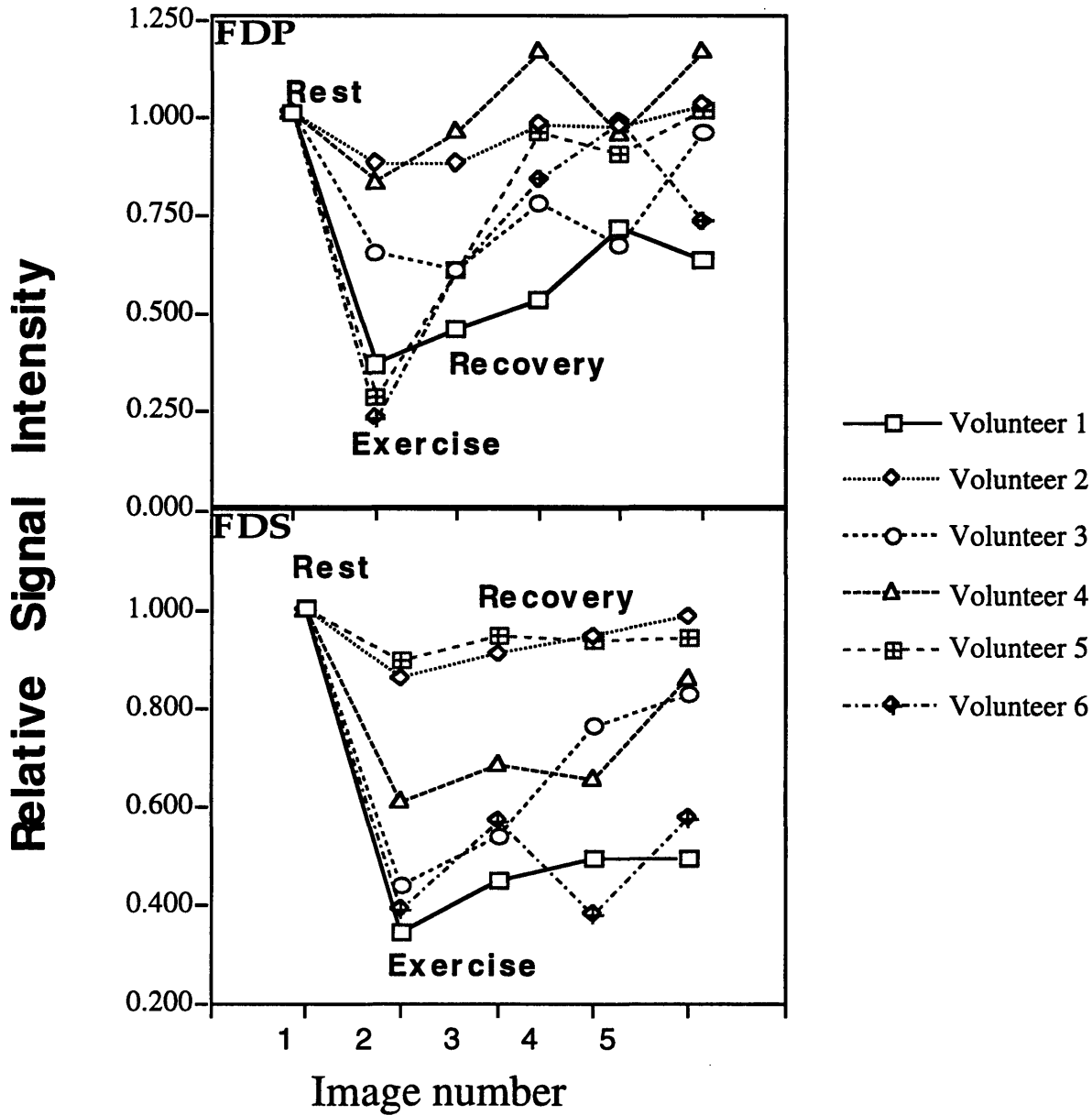


Figure 4.10. Signal intensity vs. time in the FDP and FDS. As FDP and FDS are the two muscle groups involved most in the finger flexion, signal intensities in these two area are plotted during rest, exercise and recovery. a. PCr recovery in FDP and b. PCr recover in FDS. Signal intensities are the average signal intensities of a 2 X 2 pixel<sup>2</sup> area chosen from FDP and FDS. PCr recovery rates markedly differ among volunteers which suggests multiple factors could affect the PCr recovery rates.

## Chapter 5.

### Discussion

Our studies have demonstrated the feasibility of using the RARE PCr imaging to shorten MRI scan time, thus facilitating the study of the physiological processes. With multi-echo approaches the scan time is shortened by a factor of thirty-two, providing a better temporal or spatial resolution compared with conventional techniques. PCr imaging could also be a very useful technique in the study of cardiac energetics such as myocardial ischemia, infarction, hypertrophy and brain metabolism.

#### 5.1 Pi suppression

PCr was recorded with Pi suppression. The CHESS used for Pi suppression was repeated three times to avoid incomplete suppression due to imperfect  $90^\circ$  pulse used in CHESS. The magnetization left in longitudinal  $M_z$  direction following a RF pulse is  $\cos(\theta)M_0$ , where  $\theta$  is the flip angle. Since the time intervals between each CHESS pulse are short ( $= 10$  ms) compared to the  $T_2$  value of Pi ( $\sim 200$  ms) and  $T_1$  relaxation effect is minimal, after three CHESS pulses the longitudinal magnetization  $M_z$  of Pi is  $(\cos(\theta))^3M_0$ . Even in case the flip angle is only  $70^\circ$ ,  $M_z$  of Pi left in longitudinal direction after the suppression pulse is only 4%. Pi suppression using CHESS is efficient and effective in multi-echo sequence with centric phase encoding gradient step ordering, as the  $90^\circ$  excitation pulse follows immediately after the CHESS pulse when the  $M_z$  from Pi is minimal. After the  $90^\circ$  excitation pulse, the transverse magnetization for Pi will be minimal as multiple  $180^\circ$  refocusing pulse are followed. Therefore signals from Pi are invisible in the spin-echoes following the  $90^\circ$  excitation pulse.

Another approach could be used to suppress Pi alone or used in combination with CHESS to further improve the Pi suppression in the RARE approach is the Dixon's method(Higuchi et al, 1992, Dixon 1984, Yamamoto et al, 1986), in which a proper delay  $\tau_c=1/4\omega_c$  (where  $\omega_c$  is the chemical shift difference between Pi and PCr in Hz) is introduced between the excitation pulse and refocusing pulse of conventional spin-echo imaging so as to generate a phase shift between the selected line(PCr) and chemically shifted species(Pi) at the center of the first echo in CPMG echo train. Because of this phase shift, for the chemically shifted species(Pi) the applied CPMG sequence becomes actually a CP sequence for Pi resonance with no self-correction properties for imperfect  $180^\circ$  pulse leading to enhanced signal decay and raw k-space data matrix become segmented into blocks alternately multiplied by  $\pm i$ , leading to signal dispersion following Fourier transformation(Higuchi et al, 1992).

TE used in SE spectrum acquisition is the same as the echo-spacing(= 12 ms) used in the RARE imaging sequence. Therefore, the SE signals in the spectra provided an estimation for the amount of PCr and Pi signals in the first echo RARE acquisitions and gave a general view of image SNR. The first spin echo in the RARE mode was acquired with the zero phase encoding gradients in centric phase encoding order and its intensity has dominant effect on overall signal intensity in the final RARE image.

## **5.2 CPMG mode determines the optimal number of echoes to be used in the RARE mode**

CPMG images give T2 values at each spatial location. However, for in vivo studies, especially for humans, acquiring a series of CPMG images could be long and impractical. CPMG acquired at zero phase encoding offers an estimation of a globe

T2 value assuming insignificant differences in T2 value among different muscle fiber type. In the fitting of CPMG image profiles with monoexponential decay function, errors are present in the early echo. Several factors which could contribute to those errors including possible short T2 components in PCr, T1 relaxation effect and imperfect flip angles.

### **5.3 Reducing motion artifacts**

In this study, PCr images are acquired with thirty-two echo RARE sequence and matrix size of 32 X 32. It therefore resembles an one-shot sequence with less sensitivity to motion compared to the sequence in which echoes with different phase encoding steps are acquired from two or more excitations. It is advantageous in our experiment where exercise is involved and it could be very important in applying this technique to study the myocardium when both cardiac and respiratory motions are present.

### **5.4 Implementation on the clinical system**

Although our experiments were performed on 4.7 T system, the Pi and PCr separation on 1.5 T clinical system (>100 Hz) could allow the implementation of these studies on a clinical system with relatively lower field strength with relatively lower SNR.

### **5.5 Instrumentation: Coil and active shielded gradients**

Alderman-grant coil is a linear transmitting/receiving coil. Compared to the quadrature coil such as Birdcage coil in which magnetic field exists along two orthogonal axes, the efficiency is lower by 40%. Thus, the imaging time could be further shortened or SNR could be further improved with quadrature transmitting/receiving coil.

Further improvements of these experiments is using proton decoupling (NOE effect) and shortening the TE. Because of the lack of active shielded gradient, and the long gradient rise time ( $\geq 400 \mu\text{s}$ ), only thirty two echoes were able to be acquired following each excitation on our system within a 400 ms T2 envelope when using TE of 12 ms. If TE can be shortened by a factor of two, resolution or SNR can be further improved by 40%.

### **5.6 PCr imaging and T2-weighted proton imaging**

On one hand muscle contraction consumes ATP which leads to the consumption of PCr, this direct effect resulting from metabolic processes can be observed with PCr imaging.

On the other hand, exercise leads to increased T2 in the muscle involved in the exercise. People suggested these changes are due to increased blood flow in the muscles groups involved in the exercises which leads to increased extra cellular free fluid or water which has higher T2 value than the restricted intracellular fluid (Fleckenstein et al., 1988, Hinshaw et al., 1979), although the exact mechanism is still not completely understood. This change of free fluid before and after exercise as a secondary change resulted from exercise can be observed with T2-weighted proton imaging.

### **5.7 PCr recovery rate**

There are three pathways in which ATP is regenerated:

#### **1. Creatine Kinase:**



#### **2. Aerobic Respiration (oxygen-requiring) Processes.**



#### **3. Anaerobic Respiration and Lactic Acid Formation.**

The early phase of glucose respiration, also called glycolysis, requires no oxygen.

The responding time of the first pathway is fast, less than a second, the later two pathways were slower (on the orders of several minutes or longer) and could differ between individuals. The first pathway reflected in our PCr image are PCr depletion during exercises. Due to the nature of the exercise performed in our experiment, the second path should be the major source of the ATP regeneration and further PCr regenerated during the recovery period. Aerobic respiration rates are affected by many factors which include: muscle fiber composition, blood oxygenation and blood flow volume. Blood oxygenation and blood flow are further affected by the heart function. These could explain the markedly various PCr-recovery rate among our volunteer.

In our study, a couple of volunteers had almost complete recovery at the first image acquired after exercise (Figure 4.10) and a recent NMR spectroscopic study by Ryschon et al., (1997) also found a recovery rate of about 2 min for foot dorsiflexion and tibialis anterior and extensor digitorum longus muscles. This findings suggest 5 min and 30 sec temporal resolution could be too long for the study of metabolism in some cases. Other factors which might affect the image signal intensity and are not considered is possible T2 change of PCr, possible decreased blood flow because of long stretching time of the arm during the data acquisition for later images and ATP drop in the case of excessive exercises. Because of centric phase encoding order, the effective TE for our image is 12 ms which can minimize the effect of PCr T2 alternation. Decreased blood flow for later image can cause decreased recovery rate of even decreased PCr level in later images during recovery. Excessive exercises which causes the ATP drop and long scan time bring error in the estimation of ATP-ase and ATP resynthesis rate by estimating the PCr drop and PCr recovery rate.

In summary, our study has demonstrated the feasibility of the RARE approach in shortening PCr imaging time, and for monitoring muscle metabolism. Further improvements such as shortening TE, using NOE effect and quadrature coils to increase imaging efficiency are necessary to increase temporal resolution for effectively estimating the ATP resynthesis rate during muscle recovery.

## References:

Abraham A. Principles of Nuclear Magnetism (Clarendon press, Oxford, England, 1978)

Albrand JP, Foray MF, Decorp M, Remy C; 31P NMR measurement of T2 relaxation times of ATP with surface coil: suppression of J modulation. Magn Reson Med. 1986, 3: 941-945.

Bachelard HS, Badar-Goffer RS, Ben-oseph O, and Morris PG, 1994, use of Combined 13C, 19F and 31P-NMR spectroscopy in research on brain metabolism. Magnetic Resonance Scanning and Epilepsy NATO ASI series A: Life Sciences Vol. 264: 241-248.

Becker ED, High resolution NMR, theory and chemical applications, 2nd Edition, Academic press., 1980.

Bottomley PA, Chales HC, Roemer PB, Flamig D, Engeseth H, Edelstein WA, Mueller OM. Human in vivo phosphate metabolites imaging with 31P NMR Magn. Reson. Med. 7: 319-336.

Bruhn H, Frahm J, Gyngell ML, Merboldt KD, Hanicke W, Sauter R, Cerebral metabolism in man after acute stroke: New observations using localized proton NMR spectroscopy. magn. Reson. Med. 1989, 9:126-131

Brown TR, Kincaid BM, Ugurbil K. NMR chemical shift imaging in three dimensions. Proc. Natl. Acad. Sci., 1982, 79:3523-3526.

Buchli R, Duc O, Martin E, Boesiger P. Assessment of absolute metabolite concentrations in human tissue by 31P MRS in vivo. Part 1: Cerebrum, cerebellum, cerebral gray and white matter. Magn. Reson. Med., 1993, 31:447-452.

Burt TC, Glonek T, Barany M. Analysis of phosphate metabolites, the intracellular PH, and the state of adenosine triphosphat in intact muscle by phosphorus nuclear magnetic resonance. The Journal of Biological Chemistry. 1976, Vol 251, No. 9: 2584-2591.

Cadoux-Hunson TA, Blackledge MJ, Radda GK; Imaging of human brain creatine kinase activity in vivo. *FASEBJ*, 1989 Dec; 3(14): 2660-6.

Carr HY, Purcell EM; Effects of diffusion on free precession in nuclear magnetic resonance experiments. *Phys. Rev.* 1954, 94: 630-638.

Chance B, Leigh JS, Kent J, McNully; Metabolic control principles and <sup>31</sup>P NMR. *Federation Proc.* 45: 2915-2920; 1986.

Dixon WT, *Radiology*, 1984, 153:189

Duyn JH, Moonen CTW; Fast Proton spectroscopic imaging of human brain using multiple spin echoes. *Magn. Reson. Med.* 1993; 30:409-414.

Duyn JH, Frank JA, Moonen CTW; Incorporation of lactate measurement in multi-spin-echo proton spectroscopic imaging. *Magn. Reson. med.* 1995; 33 101-107.

Ernst T, Lee JH, Ross BD; Direct <sup>31</sup>P imaging in human limb and brain. *J Comput Assist Tomogr*; 1993. Sep-Oct; 17(5):673-80.

Farrar TC; Density matrices in NMR spectroscopy: Part I; Concepts *Magn. Reson.*, 1990; 2:1-12.

Farrar TC; Density matrices in NMR spectroscopy: Part II; Concepts *Magn. Reson.*, 1990; 2:55-61.

Farrar TC, *An introduction to pulse NMR spectroscopy*, The Farragut Press, 1987.

Fleckenstein JL, Ganby RC, Parkey RW, Peshock RM. *Amer. J. Radiol.* 1988; 151:231

Frahm J, Bruhn H, Gyngell ML, Merboldt KD, Hanicke W, Sauter R, Localized proton NMR spectroscopy in different regions of the human brain in vivo. Relaxation times and concentrations of cerebral metabolites. *Magn. Reson. med* 1989, 11:47-63.

Friedrich J, apstein CS, Ingwall JS; 31P nuclear magnetic resoance spectroscopic imaging of regions of remodeled myocardium in infarcted rat heart. *Circulation*, 1995. dec 15; 92(12):3527-38.

Fukushima E, Roeder SB, *Experimental pulse NMR, a nuts and bolts approach*. Addison-Wesley Publishing Company, 1981.

Greenman RL, Schnall MD, Bolinger L, Cecil KM, Lenkinski RE; 31P imaging using a fast spin echo pulse sequence at 4.0T; *Proc. of 4th international society for magn reson med* 1996.

Hennig J, Naureth A, Friedburg H; RARE imaging: a fast imaging method for clinical MR. *magn Reson med* 1986; 3:823-833.

Hetherington HP, luney DJ, Vaughan JT, Pan JW, Ponder SL, Tschendel O, Twieg DB, Pohost GM; 3D 31P spectroscopic imaging of the human heart at 4.1 T. *Magn Reson Med*, 1995 Mar; 33(3):427-32.

Higuchi N, Hiramatsu K, Mulkern RV; A novel mechod for fat suppression in RARE sequences. *Magn. Reson. Med*, 1992, 27:107-117

Hinshaw WS, Andrew ER, Bottomley PA, Holland GN, Moore WS Worthington BS; *Br. J. Radiol.* 1979; 52:36.

Hochachka PW, *Muscles as Molecular and Metabolic Machines*. CRC Press, 1994.

Hochachka PW, *Fuels and pathways as designed systems for support of muscle work*. *J Exp Biol*, 1987, 115, 149-164.

Holloszy JO and Booth FW, *Biochemical adaptations to endurance exercise in muscle*. *Annu Rev. Physiol.* 1976, 38, 273-291.

Jeneson JAL, van Dobbenburgh JO, van Echteld CJA, Lekkerkerk C, Janssen WJM, Dorlan L, Berger R, Brown TR. *Experimental Design of 31P MRS Assessment of*

Human forearm Muscle Function: Restrictions Imposed by Functional Anatomy. *Magn Reson Med*; 1993. 30:634-640.

Jeneson JA, Nelson SJ, Bigner DB, Taylor JS, Murphy-Boesch J, Brown TR; Two-dimensional <sup>31</sup>P-chemical shift imaging of intramuscular heterogeneity in exercising human forearm muscle. *Am J Physiol*, 1992 Aug; 163 (2 Pt 1):c357-64

Jung W-I, Straubinger K, Bunse M, Schick F, Kuper K, Dietze G, and Lutz O, <sup>31</sup>P transverse relaxation times of the ATP signal NMR signals of human skeletal muscle in vivo; 1992, *Magn Reson Med* 28: 305-310.

Jung W-I, Straubinger K, Bunse M, Widmaier S, Schick F, Kuper K, Dietze G, and Lutz O; A pitfall associated with determination of transverse relaxation times of <sup>31</sup>P NMR signals of ATP using the Hahn spin-echo. *Magn. Reson. Med.*, 1993;30: 138-141.

Jung W-I, Widmaier S, Bunse M, Seeger U, Straubinger K, Kuper K, Dietze G, Lutz O. <sup>31</sup>P transverse relaxation times of ATP in human brain in vivo; *Magn Reson med*, 1993 Dec; 30(6):741-3.

Jung W-I, Widmaier S, Seeger U, Bunse M, Strauber A, Sieverding L, Straubinger K, van Erckelens f, Schick F, Dietze G, Lutz O. Phosphorus J coupling constants of ATP in human myocardium and calf muscle. *J Magn Reson B*, 1996, Jan; 110(1): 39-46.

Kent-Braun JA, McCully KK, Chance B, 1990, Metabolic effects of training in humans: a <sup>31</sup>P-MRS study, *J. appl. Physiol.* 69:1165

Kushmerick MJ; Patterns in mammalian muscle energetics; *J Exp Biol*, 1985 Mar; 115: 165-77.

Kushmerick MJ; Energetics studies of muscle of different types. *Basic Res Cardiol.* 1987; 82 suppl 2 17-30.

Kushmerick MJ, Moerland TS, Wisman RW; Mammalian skeletal muscle fibers distinguished by contents of phosphocreatine, ATP and Pi; Proc Natl Acad Sci USA, 1992 Aug 15; 89(16):7521-5.

Kushmerick MJ, Meyer RA, Truman RB; Regulation of oxygen consumption in fast- and slow-twitch muscle. Am. J. Physiol.; 1992, 263 (Cell Physiol. 32):C598-C606.

Lane RJ; Watough NJ, Jaros E; Effects of tenotomy on muscle histology and energy metabolism in normal and dystrophic mice; J Neurol Sci, 1989 Sep; 92(2-3): 307-16.

Maudsley AA, Twieg DB, Sappey-marini D, Hubsch B, Hugg JW, Matson GB, Weiner MW; Spin echo <sup>31</sup>P spectroscopic imaging in the human brain; Magn Reson Med; 1990; 14:415-422.

McCully K, Giger U, Argov Z, Valentine B, Cooper B, Chance B, Bank W; Canine X-linked muscular dystrophy studied with in vivo phosphorus magnetic resonance spectroscopy; Muscle Nerve, 1991 Nov; 14(11): 1091-8.

Meiboom S, Gill; Modified spin-echo method for measuring nuclear relaxation times; Rev. Sci. Instrum. 1958, 29:668-691.

Merboldt KD, Chien D, Hanicke W, Gyngell MG, Bruhn H, Frahm J; J Magn Reson, 1990, 89 343.

Mora B, Narasimhan PT, Ross BD, Allman J, Barker PB. <sup>31</sup>P saturation transfer and phosphocreatine imaging in the monkey brain. Proc Natl Acad Sci USA; 1991. Oct, 88: 8372-8376.

Mulkern R, Bowers J; Density Matrix calculations of AB spectra from multipulse sequences: Quantum mechanics meets in vivo spectroscopy; Concepts in Magnetic Resonance, 1994; 6:1-23

Mulkern RV, Melki PS, Lilly HS, Hoffer FA; 1-D spectroscopic imaging with RF echo planar(SIRFEN) methods. Magn. Reson. Imag.; 1991, 9:909-916.

Mulkern RV, Wong STS, Winalski C, Jolesz FA. Contrast manipulation and artifact assessment of 2D and 3D RARE sequences. *magn Reson Imaging* 1990; 8: 557-566.

Neubauer S, Krahe R, Schindler R, Horn M, Hillenbrand H, Entzeroth C, Mader H, Kromer EP, riegger GZ, Lackner K, et al., <sup>31</sup>P magnetic resonance spectroscopy in dilated cardiomyopathy and coronary artery disease. altered cardiac high-energy phosphate metabolism in heart failure. *Circulation*, 1992 Dec; 86(6): 181-8.

Neubauer S, Horn M, Pabst T, Godde M, Lubke D, Jiling B, Hahn D, Ertl G; Contributions of <sup>31</sup>P-magnetic resonance spectroscopy to the understanding of dilated heart muscle disease. *Eur Heart J*, 1995 Dec; 16 suppl ) 115-8.

Nelson SJ, Taylor JS; Vigneron DB, Murphy-Boesch J, Brown TR; Metabolites images of the human arm: changes in spatial and temporal distribution of high energy phosphates during exercise. *NMR Biomed*, 1991. Dec 4(6):268-73.

Oshio K, Mulkern RV, Rapid fat/water assessment in knee cavity bone marrow by inner volume spectroscopic imaging with RARE, *J. of Magn. Reson. Imag.*, 1992, 2:601-604.

Prichard JW., Alger JR, Behar KL, Petroff OAC and Shulman RG , 1983, cerebral metabolic studies in vivo by <sup>31</sup>P NMR, *Proc Natl Acad Sci*. 80: 2748-2751.

Ryschon TW, Fowler RE, Wysong AR, Anthony AR and Balaban RS; Efficiency of human skeletal muscle in vivo: Comparison of isometric, concentric and eccentric muscle action. Submitted to *Am. J. Physiol.*, 1997.

Rosen BR, Fleming DM, Kushner DC, Zaner KS, Buxton RB, Bennet WP, Wismer GL, Brady TL, Hematologic bone marrow disorders: Quantitative Chemical shift MR imaging. *Radiology*, 1988, 169: 799-804.

Ryvlin P, Philippon B, Cinotti L, Froment JC, Le Bars D, and Mauguiere F. Functional neuroimaging strategy in temporal lobe epilepsy: a comparative study of <sup>18</sup>F-FDG-PET and <sup>99m</sup>Tc-HMPAO-SPECT. *Ann Neurol*. 1992; 31:650-656.

Slichter CP, Principles of Magnetic Resonance. 3rd Edition. Springer-Verlag, 1989.

Straubinger K, Jung WI, Bunse M, Lutz O, Kuper K, Dietze G, Spin-echo methods for determination of <sup>31</sup>P transverse relaxation times of ATP signals of human skeletal muscle in vivo. *magn. Reson. Imag.* 1994, 12:121-129.

Stryer L, *Biochemistry*. 1988. Third edition Freeman Press

Tsuji MK, Mulkern RV, Cook CU, Meyers RL, Holtzman D, Relative phosphocreatine and nucleoside triphosphate concentrations in cerebral gray and white matter measured in vivo by <sup>31</sup>P nuclear magnetic resonance, 1996, *Brain Research* 707: 146-154.

Thomsen C, Jensen KE, and Henriksen O, 1989, *Magn reson Med* 3: 941

Takeo S, Taguchi R, Tanonaka K, Miyake K, Horiguchi R, Takagi N, fujimori K; Sustained damage to energy metabolism of brain regions after microsphere embolism in rats, *Stroke*, 1992 Jan; 23 (1): 62-8.

Thomsen C, Jensen KE, Henriksen O, <sup>31</sup>P NMR measurements of T2 relaxation times of metabolites in human skeletal muscle in vivo. *Magn. Reson. Imag.* 1989;7:557-559.

Turner JC, Garlick PB, One- and two- dimensional <sup>31</sup>P spin-echo studies of myocardial ATP and phosphocreatine. 1984, *J. Magn. Reson.* 57:221-227

Walker JB, Creatine: biosynthesis, regulation and function 1979, *adv. Enzymol.* 50, 177-242.

Yamamoto E Kohno H, *Phys. Med. Biol.*; 1986, 3:713.

8050-90